ABSTRACT

Duan, Emily Tzu-Chieh. Design, Optimization, and Testing Soft Fluidic Actuators and Sensors (Under the direction of Dr. Matthew Bryant).

Deformable sensors and energy sources have been recognized as a key technology to enabling applications from wearable electronics and health monitoring implants to soft robotics and sensors. Although significant progress has been made, improving the versatility and operating efficiency of these systems remains a challenge. This dissertation addresses gaps in current hierarchical actuation and architectural design of spatially constrained soft fluidic actuators as well as improving performance of soft supercapacitors.

The first study presented in this dissertation explores the implications of pennation angle on spatially constrained bi-pennate fluidic artificial muscle (FAM) bundle designs. While studies on natural muscles show the pennate topology can achieve higher output force per geometric cross-sectional area, it is not necessarily true for FAM bundles due to the contraction and rotation behavior of individual actuator units (fibers). A method for muscle bundle parameterization based on the desired bundle spatial bounds is presented in this study. The study showed individual FAM contraction and rotation are both key factors contributing to situations where bipennate muscle topologies are advantageous as compared to parallel muscle topologies. The results illustrate bipennate artificial muscle bundles can be designed to amplify the muscle contraction, output force, stiffness, or work output capacity as compared to a parallel bundle with the same envelope dimensions. Furthermore, analysis on a fiber contact boundary condition for the FAM bundle illustrate opportunities for packing more actuator units than a pinned boundary condition. The fiber boundary condition can also enable certain bi-pennate FAM bundle designs to behave as a negative stiffness structure.

The second study describes a design optimization framework for spatially constrained FAM bundle to address challenges in identifying tradeoffs between different different architectural designs. While some tradeoffs are identified between different muscle architectures, this optimization tool is a method to map architectural tradeoffs to soft actuator designs. Desirable topological properties are realized using a multi-objective genetic algorithm-based optimization framework based on the objectives and spatial constraints provided. The generated Pareto frontier results outline optimal architectural designs across the operating space and inform design decisions based on the force and stroke demand from the desired operating task. Topological properties such as number of FAMs in the bundle, individual FAM sizing, and FAM pennation angle can be extracted from the optimal architectural designs on the Pareto frontier. The study also illustrates how the desirable topological properties of the optimzied FAM bundle changes with respect to different spatial bounds.

The third study is an approach to improve the performance of a soft variable-area electrochemical supercapacitor with the use of a helically braided fiber reinforced sleeve. The soft variable area electrochemical supercapacitor is able to convert mechanical motions into electricity by actively modulating the electrical double layer (EDL) area of the liquid metal electrode. Analysis on the kinematics of the braided sleeve show a greater change in EDL area per unit axial stretch of the electrode from amplified radial compression. This change in EDL area induces capacitance change and movement of charges in the circuit. When a mechanical input of cyclic axial stretch is applied on the working electrode, it produces alternating current. Simulation and experimental results show a significant increase in peak current per unit axial stretch with the presence of the braided sleeve as compared to without the braided sleeve.

Design, Optimization, and Testing Soft Fluidic Actuators and Sensors

by
Emily Tzu-Chieh Duan

A dissertation submitted to the Graduate Faculty of
North Carolina State University
in partial fulfillment of the
requirements for the degree of
Doctor of Philosophy

Mechanical Engineering

Raleigh, North Carolina
2024

APPROVED BY:

_____	_____
Dr. Matthew Bryant Committee Chair	Dr. Katherine Saul
_____	_____
Dr. Andre Mazzoleni	Dr. Nitin Sharma

DEDICATION

To my parents, Daniel and Yushuang, and sister, Amy.

To every teacher, professor, mentor, and friend.

BIOGRAPHY

Emily Tzu-Chieh Duan received her B.S. degree in Mechanical Engineering with a minor in Entrepreneurship and Innovation from the University of Maryland, Baltimore County (Catonsville, MD) in May 2019. At UMBC, Emily was a Center for Women in Technology (CWIT) scholar, NAE Grand Challenges scholar, Mechanical Engineering S-STEM scholar, and Meyerhoff Affiliate. She was an active member and held leadership positions in several groups on campus, including Secretary of the UMBC Chapter of the American Society of Mechanical Engineers (ASME) organization, Co-founder and Secretary of the UMBC Grand Challenges Student Club, and Historian for the CWIT Student Council.

In August 2019, she subsequently began her graduate studies in the direct-to-PhD program at North Carolina State University (Raleigh, NC) and joined the Intelligent Structures and Systems Research lab (iSSRL) in the Mechanical and Aerospace Engineering Department. During her time at NCSU, Emily was a Provost Doctoral Fellow, Dean's Doctoral Fellow, and NC Space Graduate Research Fellow. In 2023, she received her en-route Master's of Science degree in Mechanical Engineering. Emily has published one journal paper in the MDPI Actuators, one paper has been submitted for publication in the Bioinspiration and Biomimetics Journal, and a third paper is under preparation for submission for publication in the Advanced Materials Technologies Journal. Her research interests are focused on improving mechanical systems via novel configurations and actuation techniques.

ACKNOWLEDGMENTS

To my parents, Daniel and Yushuang, and sister, Amy, thank you for your unconditional love and support as well as faith in me to pursue my goals and education to the fullest. Thank you to my advisor, Dr. Matthew Bryant, for his patience, guidance, and support throughout my graduate career. I am grateful to have joined his research team, and his mentorship has been essential in fostering me to become a better researcher and engineer. To my dissertation committee, Dr. Katherine Saul, Dr. Andre Mazzoleni, and Dr. Nitin Sharma, thank you for serving as educators and resources for me during my time at NC State. I greatly appreciate your expertise and guidance in my education and research. To my iSSRL lab mates and the FAM group, it had been a joy to work and learn from all of you.

I gratefully acknowledge funding sources for my research. Material in the second and third chapter was supported by the Faculty Early Career Development Program (CAREER) of the National Science Foundation under NSF Award Number 1845203. Material in chapter 4 is supported by the North Carolina Renewable Ocean Energy Program administered by the Coastal Studies Institute. During my time at NCSU, I was also supported by the NCSU Provost's Doctoral Fellowship, NC Space Grant Graduate Research Fellowship, and NCSU College of Engineering Dean's Doctoral Fellowship.

TABLE OF CONTENTS

LIST OF TABLES

LIST OF FIGURES

CHAPTER 1: Introduction

1.1 Motivation

While actuators and sensors are vital for mechanical systems to interface with the physical world, compliance is essential to address challenges where adaptivity and multifunctional properties are desired but not possible with conventionally rigid designs. [1,2] These soft devices include but are not limited to stretchable electronics [3–5], wearables [6–10], energy harvesters, and soft robotics [11–16]. Toward this effort, researchers have explored alternative materials to substitute structurally stiff components [17–25] and drawn inspiration from biological systems to improve versatility and efficiency [12,26].

Considering the complexity and range of motion in human skeletal muscles, many have sought methods to mimic or imitate the behaviors observed [27]. One approach is to use the hierarchical structure found in mammalian muscles, where an organized set of actuation elements can be called upon as desired [28,29]. The evolution of muscle tissues enables the body to pack a large number of actuators into a compact package for a variety of kinematic behaviors. This is made possible by the diversity of the muscle topology, where actuation elements can be sized, arranged, and oriented in various configurations [30,31]. This muscle architecture and control strategy can be leveraged in robotics to improve energy efficiency, bandwidth, and variable stiffness control. Applying this approach to soft, muscle-inspired actuators allows for topological freedom not possible in traditional robotic actuation systems like motors and pistons. The inherent compliance, ease of fabrication, and high force-to-weight ratio of McKibben muscles or fluidic artificial muscles (FAMs) are attractive properties for soft actuators in the robotics research community, especially for prosthetics, wearable devices, as well as robots that interact with humans. The McKibben muscle consists of an elastomeric tube with a helically braided fiber reinforced mesh sleeve that uses fluid pressure (pneumatic or hydraulic) to radially

expand the inner tube while the inextensible fiber braid design allows for axial contraction. This helically braided fiber reinforced sleeve is a tubular structure composed of multiple fibers crossing over and under each other, similar to a basket weave, but the pattern created visually appears as a twill weave, where a set of fibers in the same direction appear to be oriented at a specified angle while another set of fibers appear to be positioned at the same specified angle but in the opposite direction. This tubular pattern structure allows for even distributed load and commonly found in a variety of applications from hydraulic brake hose lines in cars to everyday garden hoses. In most common applications, the fibers are aligned in the direction of the resultant tangential and axial forces experienced by the hose to prevent deformation or rupture such that it can operate under high force, high pressure, and/or temperature-varying conditions. However, for soft actuator designs such as the McKibben muscle or fluidic artificial muscle (FAM), the fibers are aligned based on the desired axial and radial behavior. Much like natural human muscle tissues, FAMs can be sized, oriented, and organized into a bundle to produce various topologies, different force-displacement behaviors, and differing dynamic responses. This hierarchical actuation allows the use of geometric complexity to tailor configuration, speed, force, efficiency, and stroke.

Current literature focuses on the kinematic behavior of FAMs arranged in parallel [32–36]. Although this parallel actuator is one embodiment of a hierarchical actuator, present literature exploring other configurations is sparse. In 2013, Azizi et al. was the first to study FAMs in a unipennate array and found variable gearing exists much like in natural muscles, which is possible purely due to this architectural feature [37,38]. In more recent studies, Jenkins et al. developed a constitutive model to describe the coupled relationship between force, speed, and stiffness of individual FAMs to that of the bundle and validated the model via a proof-of-

concept bipennate FAM array [39]. A myriad of muscle fiber arrangements and topologies remain and have yet to be explored with FAMs. To this end, there are several gaps within current research that need to be addressed. The first gap in our understanding is the effect of pennation angle (shown in Figure 1) on spatially constrained bipennate FAM bundle design and actuation performance. While it is generally known that a pennate muscle generates more output force and less contraction than that of a parallel muscle of similar size and anatomical cross-sectional area, the effects of pennation angle on force, contraction, stiffness, and work output with FAM actuators still need to be quantified for complete understanding of this architectural feature. The second gap is to map the FAM bundle topology to desired objective(s) subject to various spatial envelopes. While inspiration can be drawn from nature to mimic various muscle tissue designs, they may not be ideal or optimal for applications on a legged robot with different joint angles and limb parameters or a wearable assistive device to be work around the human limb. Although models for pennate FAM bundle behavior have been developed and validated [39], a computational design tool is needed to consider kinematic and geometric constraints and inform desirable topological properties in FAM bundle design.

A complementary objective of this research addresses an approach to improve the performance of a soft variable area supercapacitor with a helically braided fiber reinforced sleeve. Variable area supercapacitors rely on the ability to alter the electrical double layer (EDL) area or interfacial area between the electrode and electrolyte in the solution [40]. A recent development of this soft variable area electrochemical supercapacitor is composed liquid metal electrodes encapsulated inside a hydrogel casing. The study showed the behavior of this type of soft supercapacitor is influenced by the electrode area, electrolyte concentration, mechanical deformation amplitude, and input frequency. [41] With the presence of the helically braided fiber

reinforced sleeve, the kinematics of the braided sleeve amplifies the radial compression of the soft supercapacitor when axially stretched to produce a greater change in EDL area and induced capacitance.

1.2 Research aims

1.2.1 Objective 1: Investigate implications of spatial bounds on FAM bundle actuation with bipennate topology

Gap in the status quo: Current studies lack the ability to quantify effects of pennation angle on fluidic artificial muscle bundle actuation behavior. Researchers have observed notable differences in actuation behavior with varying muscle architecture types, of which parallel and pennate muscle fiber arrangements are found most commonly in human skeletal muscle tissues [42,43]. Long fibers in parallel generate significant muscle contraction while short fibers arranged obliquely to the line of motion enable additional fibers to be added and contribute to a greater amount of force. While this tradeoff is conceptually understood, a direct and fair comparison to quantify this behavior in FAMs requires parameterizing individual FAMs in the bundle based on a uniform spatial envelope that the actuators remain within during actuation.

Objective 1: Understand implications of spatially constrained bipennate topology of fluidic artificial muscle bundle actuation.

1.2.2 Objective 2: Develop a design optimization tool for spatially constrained FAM bundle

Gap in the status quo: Optimal FAM bundle topology for desired actuation objective(s) subject to spatial envelope constraint is unknown. Although models of parallel and pennate FAM bundles have been developed and demonstrated, it is unclear under what conditions which topology should be selected. A purely biomimetic approach to FAM bundle design may not be optimal given the requirements and constraints on a human can be drastically different from those on a legged robot or wearable assistive device. Thus, a strategic method of optimizing FAM bundle topology for a given application is needed. The optimal FAM bundle topology will

likely differ based on the optimization cost function, such as minimizing input energy, minimizing actuator mass, and maximizing limb payload. Previous work in FAM bundle topology design assumes a uniform arrangement of homogeneous FAMs, which may not present to be most efficient or desirable. Enabling heterogeneity within the FAM bundle brings about potential improvements in bundle performance but there have yet to be studies on the parameterization and behavior of heterogeneous FAM bundles with pennate topologies.

Objective 2: Develop a framework for optimizing fluidic artificial muscle bundle topologies given desired actuation kinematics and geometric constraints for a specified objective function.

1.2.3 Objective 3: Examine strain amplified soft supercapacitor with helically braided fiber reinforced sleeve

Gap in the status quo: The performance of variable area supercapacitors is limited by the electrode area, electrolyte concentration, and mechanical input parameters. A recent development of a soft variable area electrochemical supercapacitor has been demonstrated to convert mechanical motion into electricity with the use of liquid metal electrodes encapsulated inside a hydrogel casing [41]. While the study showed increased mechanical input amplitude and frequency result in greater induced current response, there has yet to be studies exploring methods to amplify the generated current response per unit of mechanical deformation.

Objective 3: Investigation of a soft variable area electrochemical supercapacitor with a helically braided fiber reinforced sleeve to improve performance.

1.3 Dissertation structure

Chapter 2 focuses on the pennation angle sensitivity for spatially constrained FAM bundle actuation and explores different boundary conditions. Chapter 3 presents an optimization tool for spatially constrained FAM bundle designs to inform design decisions and evaluate tradeoffs of various topologies based on the objective. Chapter 4 details the approach for

improving the performance of a soft variable area electrochemical supercapacitor with a helically braided fiber reinforced sleeve. Finally, Chapter 5 summarizes the findings of this research and highlights the research contributions.

CHAPTER 2: Implications of spatially constrained bipennate topology on fluidic artificial muscle bundle actuation

2.1. Introduction

Actuators are vital to enabling mechatronic systems to interface with the physical world. Thus, roboticists and engineers have placed a great deal of attention on the design of actuators and many have drawn inspiration from distinctive attributes of biological muscles to equip actuators with safe human-robot interaction capabilities. Neuromuscular physiology and anatomy studies have shown that a single biological muscle tissue is comprosed of multiple motor units [30]. Each motor unit consists of hundred to thousands of muscle fibers that can be arranged in a variety of topologies. Analagously, hierarchical actuators use multi-unit architectures to augment the total actuator performance and increase actuator functionality [29]. The practicality of this hierarchical actuation strategy has been demonstrated on cellular piezoelectric actuators [30], whiffletree actuators [29], series-parallel elastic actuators [44], and bioinspired orderly recruitment actuator bundles [45]. This muscle-inspired hierarchy has led to the development of linear bundle actuators capable of mimicking orderly recruitment and thus improving efficiency by activating only the smallest required actuator unit for a given task [45–47]. Recent studies have explored parallel and pennate topologies of bundle actuators [44,48,49]. The parallel topology configures the longitudinal axis of individual actuator 'fibers' parallel to the bundle actuator line of motion while the pennate topology orients individual actuator fibers at an angle to the bundle line of motion. These topologies are bio-inspired: human skeletal muscle tissues exhibit parallel (e.g. bicep's brachii muscle), asymmetric unipennate (e.g. extensor digitorum or posterior forearm muscle) and symmetric bipennate (e.g. rectus femoris in the quadriceps muscle group) architectures [28]. Advantages of the pennate topology in biological muscles and the effects of fiber pennation angle on contraction speed, damping from impact disturbances, and aging have been emphasized in numerous studies [38,39,48,49]. The coupling between the

muscle force and displacement to the fiber force and displacement results in the ability to passively alter the effective gear ratio (i.e. the effective relationship between muscle fiber input and macro muscle outputs) [39,48,49]. This passive control of effective gear ratio has led to the categorization of pennate actuator bundles as variable stiffness actuators, which are especially attractive for their potential in energy storage. Furthermore, appropriately controlled variable stiffness may allow for safer human-robot interaction [50].

McKibben fluidic artificial muscles are particularly suitable for pennate bundle actuators due to their muscle-like actuation behavior, inexpensive construction, inherent flexibility, and high force-to-weight ratio. The dense, helical braid sleeve around the soft elastomer allows it to generate forces of hundreds to thousands of Newtons. While previous studies have established models for the force generation, contraction, and stiffness mechanics of pennate McKibben artificial muscle bundle actuators [39,48,51], the relationships between pennation topology and actuator output characteristics for a given actuator envelope have not been studied to date.

This paper explores the parameterization, design, and analysis of a bio-inspired pennate topology fluidic artificial muscle (FAM) bundle actuator under spatial envelope constraints. The primary contributions of this paper are to establash the sensitivity of FAM bundle actuation performance characteristics including force, contraction, work output, and stiffness to pennation angle and fiber boundary condition when bundle envelope dimensions are held constant. The results reveal that bipennate topologies, when appropriately designed, can achieve force, contraction, work, or stiffness performances exceeding that of a parallel topology muscle bundle with equivalent envelope dimensions, but that tradeoffs exist between fiber boundary conditions. If the mucle bundle is configured with contacting fibers, competing effects of fiber radius and length give rise to extensile motions and negative stiffnesses for some designs. The remainder of

this paper is organized as follows: Section 2 presents the system formulation with method for muscle bundle parameterization for a prescribed bundle spatial envelope for fiber bounding conditions, Section 3 discusses and examines effects of boundary conditions and pennation angle on muscle bundle performance, and Section 4 enumerates the conclusions of the paper.

2.2. System Formulation

2.2.1. Muscle Topologies

A bundle actuator consists of multiple McKibben fluidic artificial muscles (FAMs), where individual FAMs are referred to as "fibers" and the complete bundle actuator is referred to as a "muscle". Fibers in a pennate topology are arranged at a angle to the direction of muscle bundle motion. The fibers in a pennate muscle are subject to axial contraction, radial expansion, and rotation upon actuation. A special case of fibers with zero pennation angle is also recognized as the parallel topology. The critical difference in this zero pennation angle configuration is the fibers will only contract axially and expand radially, but not rotate. Each muscle topology in this analysis is considered as a single-layer, two-dimensional array of fibers. All fibers have the same initial braid angle α_i. The fibers in the pennate topology are assumed to be symmetrically oriented in a bipennate arrangement. Figure 2.1 is a visual representation of the two muscle topologies under consideration. Figure 2.1(a) illustrates the special case zero pennation configuration or parallel fiber topology and Figure 2.1(b) shows the bipennate fiber topology. The fibers are represented as red cylinders.

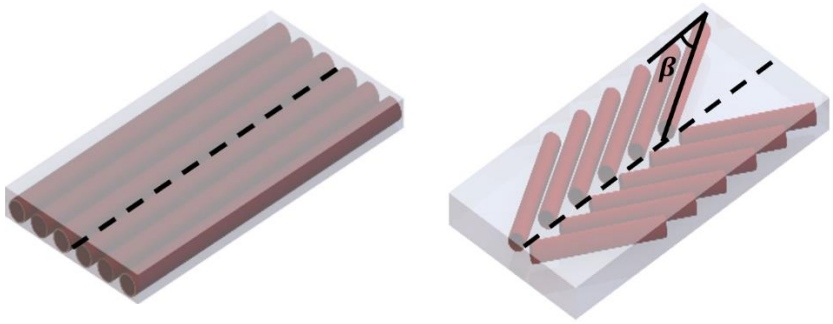

(**a**) Parallel topology (**b**) Bipennate topology

Figure 2.1 Three-dimensional visual representation of muscle topologies considered. The shaded region indicates the bounding envelope. The black dashed centerline is the muscle axis of motion. The β shown in (b) indicates the pennation angle or angle at which the fiber is oriented with respect to the muscle line of motion.

2.2.2. Design Case and Fiber Boundary conditions

The goal of this study is to understand the effects of configuring the bundle with different initial fiber pennation angles while maintaining uniform envelope dimensions of the bundle. We take the bundle envelope, shown as the shaded region in Figure 2.1, as the smallest fixed prismatic rectangular volume that all portions of the bundle remain within throughout actuation. Therefore, for each initial pennation angle, the parameters including fiber number, initial length, and initial radius must be determined such that the configuration remains within the prescribed envelope during actuation. From among the set of configurations that would satisfy this criterion for each initial pennation angle, we consider a design that sets the initial fiber radius, length, and number such that the initial total internal volume of the fibers within the envelope is as large as possible.

We also consider two sets of fiber boundary conditions:

- The *'fiber contact boundary condition'* defines that contact between fibers is maintained during actuation. Fibers are assumed to remain cylindrical and are constrained to remain in frictionless, tangential contact such that they can freely slide relative to one another but cannot be separated. Physically, this could be implemented by pinning one end of the outer or top-most pair of fibers to a rigid external frame while the remaining fiber ends on the rigid frame are able to slide freely. The opposite ends of the fibers are connected to their respective symmetric counterparts to complete the bipennate arrangement. Figure 2.2(b) illustrates a visual representation of fibers under this boundary condition. This fiber contact boundary condition represents an idealization of the function of the connective tissue in biological muscles that surrounds individual muscle fibers and enables fibers to slide relative to one another while holding the fibers together transversally. This connective tissue, or endomysium, is deformable to adapt to volumetric changes during muscle fiber contraction and has been shown to have a limited role in transmitting muscular force [52]. This fiber contact boundary condition thus serves as a direct analogy to biological muscle physiology.
- The *'pinned boundary condition'*, illustrated in Figure 2.2(a), defines that one end of each fiber is pinned to the rigid frame while the other end is pinned to a central spine. Because the pin joints are fixed to rigid bodies, an initial clearance must be provided between the fibers such that the fibers do not interfere with one another during contraction and the resulting radial expansion. We consider the case where this clearance is set such that the fibers contact one another at exactly one contraction condition and never interfere over the full stroke of the muscle.

While the fiber contact boundary condition is more closely bioinspired, the pinned boundary condition is mechanically simpler because it eliminates the need for sliding degrees of freedom within the muscle.

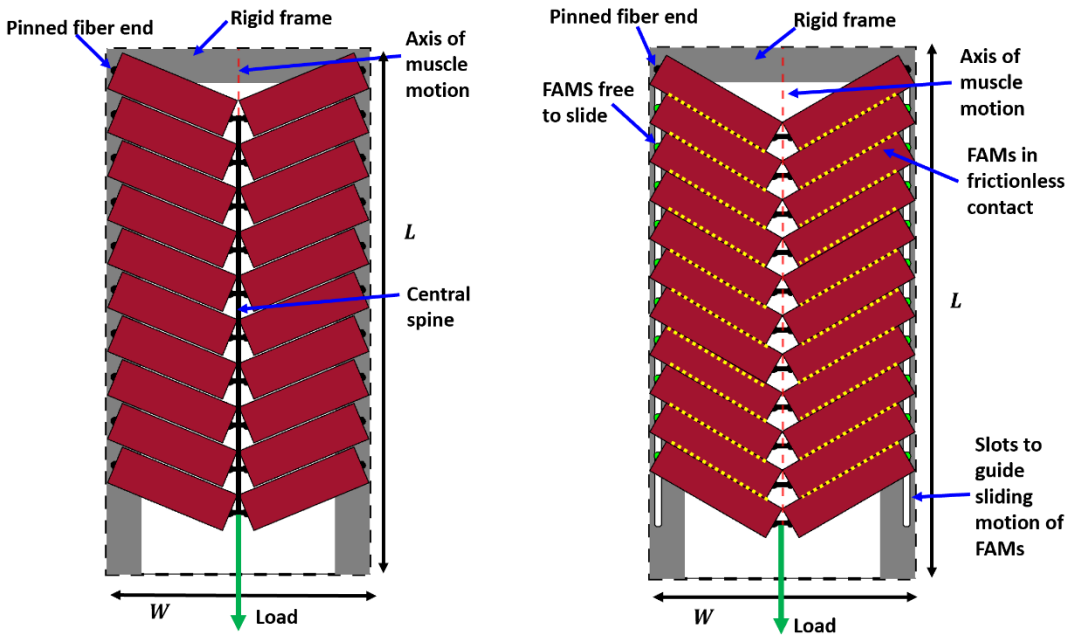

(**a**) (**b**)

Figure 2.2 Two-dimensional visual representation of (a) pinned boundary condition and (b) fiber contact boundary condition of a bipennate muscle. The length and width of the bounding envelope are illustrated. The muscle is shown in planar view so the depth dimension D is not indicated. The bounding envelope is indicated by the black dashed lines around the rigid frame. The red dashed vertical line represents the axis of muscle motion, and the green arrow indicates the applied load. The black semicircles indicate the pinned fiber end locations on the rigid frame and central carriage. The green semicircles indicate the fiber ends to translate vertically along the rigid frame and central carriage. Symmetric slots on the frame and central carriage in (b) are shown to direct vertical translation of the FAMs. Yellow dotted lines in (a) indicate FAM surfaces in frictionless contact.

2.2.3. Muscle Bundle Parameterization

This section details a method to determine the set of fiber parameters based on a prescribed initial pennation angle in this muscle bundle design. The initial pennation angle in combination with the fiber contraction behavior will dictate the fiber behavior during muscle contraction. The fibers in the topology can be contraction-limited, rotation-limited, or both at free contraction of the muscle. If the configuration is rotation-limited, it indicates the fibers are not capable of reaching their full contraction potential but will reach full rotation. Therefore the pennation angle at free muscle contaction $\beta_{free} = 90°$ as shown in Figure 2.3.

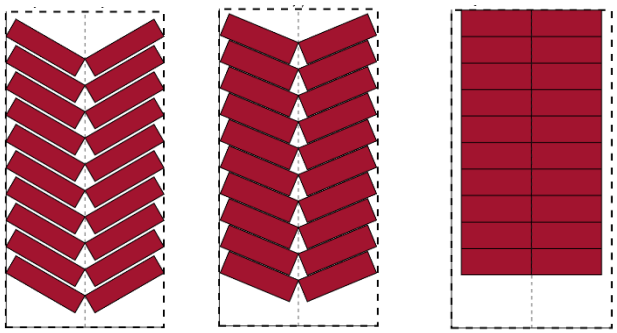

(**a**) $\varepsilon_m = 0$ (**b**) $\varepsilon_m = \frac{\varepsilon_{free}}{2}$ (**c**) $\varepsilon_m = \varepsilon_{free}$

Figure 2.3 Two-dimensional visual representation rotation-limited bipennate fibers during muscle contraction from zero muscle strain (a) to free contraction muscle strain (c). The planar view of the bounding envelope is indicated by the black dashed lines. Each image is a snapshot of the fiber dimension and orientation at different stages of muscle strain ε_m.

If the configuration is contraction-limited, it indicates the fibers are not capable of reaching full rotation but will reach their full contraction as illustrated in Figure 2.4. Therefore, a contraction-limited configuration will have $\beta_{free} < 90°$ and the fiber braid angle at free contraction $\alpha_{free} = \alpha_{max}$ where α_{max} is the fiber braid angle corresponding to the maximum attainable fiber contraction at a given pressure. If the configuration is both contraction and

rotation-limited, it indicates that the fiber will reach full contraction and full rotation simultaneously and thus $\alpha_{free} = \alpha_{max}$ and $\beta_{free} = 90°$.

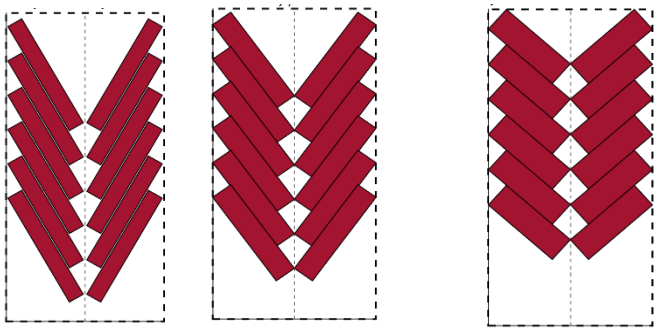

(**a**) $\varepsilon_m = 0$ (**b**) $\varepsilon_m = \frac{\varepsilon_{free}}{2}$ (**c**) $\varepsilon_m = \varepsilon_{free}$

Figure 2.4 Two-dimensional visual representation contraction-limited bipennate fibers during muscle contraction from zero muscle strain (a) to free contraction muscle strain (c). The planar view of the bounding envelope is indicated by the black dashed lines. Each image is a snapshot of the fiber dimension and orientation at different stages of muscle strain ε_m.

To analyze this muscle contraction behavior, we consider the fibers as idealized McKibben actuators such that the model assumes a cylindrical fiber geometry, and negligible bladder thickness and stiffness [53]. Muscle bundle thickness is held constant to enable a explicit relationship between fiber axial contraction and rotation for finding β_{free} and α_{free}.

$$\therefore \beta_{free} = \sin^{-1}\left(\frac{\sin(\beta_i)\cos(\alpha_i)}{\cos(\alpha_{max})}\right) \tag{1}$$

$$\alpha_{max} = \tan^{-1}(\sqrt{2}) \cong 54.7°$$

$$\therefore \alpha_{free} = \cos^{-1}\left(\frac{\sin(\beta_i)\cos(\alpha_i)}{\sin(\beta_{free})}\right) \tag{2}$$

where β_i is the initial fiber pennation angle and α_i is the initial braid angle.

Relationships between fiber parameters and dimensions of the bounding envelope can be formulated as follows to ensure the fibers remain inside the bounding envelope during muscle contraction [50]:

$$(\frac{n_w}{2} - 1)\frac{2r_f}{\cos(\beta)} + 2r_f\cos(\beta) + l_f\sin(\beta) \leq \frac{W}{2} \quad (3)$$

$$\left(\frac{n_l}{2} - 1\right)\frac{2r_f}{\sin(\beta)} + 2r_f\sin(\beta) + l_f\cos(\beta) \leq L \quad (4)$$

where n_w is the number of fibers that can fit along the prescribed width dimension of the bounding envelope W, n_l is the number of fibers that can fit along the prescribed length dimension of the bounding envelope L, r_f=$\frac{\sin(\alpha)}{\sin(\alpha_i)}r_{f,i}$ is the instaneous fiber radius, $l_f = \frac{\cos(\alpha)}{\cos(\alpha_i)}l_{f,i}$ is the instaneous fiber length, and α is the instaneous braid angle. Inequalities (3) and (4) are used to assess the muscle bundle length and thickness remain within the prescribed bounding envelope. These constraints are necessary to design a bipennate topology muscle bundle under spatial bounds. However, these are not sufficient conditions to determine the set of fiber parameters for this muscle bundle design. Furthermore, these conditions are not adequate for designing bipennate topology muscle bundles with pinned boundary conditions.

This study analyzes a design that sets the fully expanded fiber diameter such that the initial volume of the muscle bundle is maximized within the spatial bounds. Therefore, the fiber radius at free muscle contraction is bounded as $0 < r_{f,free} \leq \frac{\mathrm{D}}{2}$. For this range of possible fiber radii at free muscle contraction, corresponding fiber parameters can be determined for each initial

pennation angle to obtain the set of fiber parameters that gives the largest initial muscle bundle volume

$$V_m = n\pi r_{f,i}^2 l_{f,i} \tag{5}$$

for each initial pennation angle, where $n = \max(n_w, n_l)$.

For a possible $r_{f,free}$ within the bounds, the initial fiber radius $r_{f,i}$ can be derived as

$$r_{f,i} = \frac{\sin(\alpha_i)}{\sin\left(\tan^{-1}(\sqrt{2})\right)} r_{f,free} \tag{6}$$

For a parallel topology, the fibers only contract axially during muscle contraction. Therefore, the fibers in a parallel topology are always contraction-limited. The initial fiber length and the number of fibers are bounded by the length and width of the bounding envelope, respectively. Based on the orientation of the fibers in the bounded space, the fibers can only be arranged along the width dimension of the bounding envelope ($n_l = 1$). Inequality (3) can be used to realize the n_w, which is equivalent to the number of fibers that can fit within the bounding envelope n. n must be a positive non-zero integer. For bipennate topology, the fiber length and the maximum number of fibers that can fit in the bounding box depend on the fiber behavior. Although the constraints can provide insight on the fiber parameters, $l_{f,i}$ and n are coupled and will depend on the minimum fiber clearance required to enable the fibers to fully contract, rotate, or both. An initial fiber length can be estimated from the following relationship.

$$l_{f,i} = \max\left(\frac{L - max\left(r_f\, sin(\beta)\right) - r_f\, sin(\beta)}{\frac{cos(\alpha)}{cos(\alpha_i)}\cos(\beta)}\right) \tag{7}$$

This relationship depends on the minimum fiber clearance along the length dimension of the bounding envelope from the top-most pair of fibers, $\max\,(r_f \sin\,(\beta))$. Assuming that at least one

pair of fibers can fit along the width dimension of the bounding box (i.e. $n_w \geq 2$), this estimated initial fiber length must satisfy inequality (3). If this estimated initial fiber length satisfies constraint (3), then this estimated initial fiber length is valid. However, this does not automatically indicate that a single pair of fibers is the maximum number of fibers that can fit along the width dimension of the bounding box. The appropriate n_w and n_l will need to be determined with this set of valid fiber dimensions based on the fiber boundary conditions. For the fiber contact boundary condition, the exact n_w and n_l only need to satisfy inequalities (3) and (4) respectively. For the pinned boundary condition, a minimum clearance is needed to determine the fiber pin locations such that the fibers do not interfere with one another during contraction and the resulting radial expansion. In addition, the n_w and n_l need to satisfy the following inequalities as well as inequalities (3) and (4) respectively to ensure the fibers remain inside the prescribed bounding envelope during muscle contraction:

$$\left(\frac{n_w}{2} - 1\right) \max\left(\frac{2r_f}{\cos(\beta)}\right) + 2r_f \cos(\beta) + l_f \sin(\beta) \leq \frac{W}{2} \tag{8}$$

$$\left(\frac{n_l}{2} - 1\right) \max\left(\frac{2r_f}{\sin(\beta)}\right) + 2r_f \sin(\beta) + l_f \cos(\beta) \leq L \tag{9}$$

The minimum clearance required between fibers along the width dimension of the bounding envelope is expressed as $\max\left(\frac{2r_f}{\cos(\beta)}\right)$ and the minimum clearance needed between fibers along the length dimension of the bounding envelope is computed as $\max\left(\frac{2r_f}{\sin(\beta)}\right)$. If this estimated initial fiber length violates inequality (3), the estimated initial fiber length must be recomputed

with $n_w = 2$. Note that both n_w and n_l must be even and positive non-zero integers. The fibers are laterally arranged if $n_w \geq n_l$ and centrally arranged if If $n_w < n_l$. These fiber arrangements are illustrated in Figure 2.5.

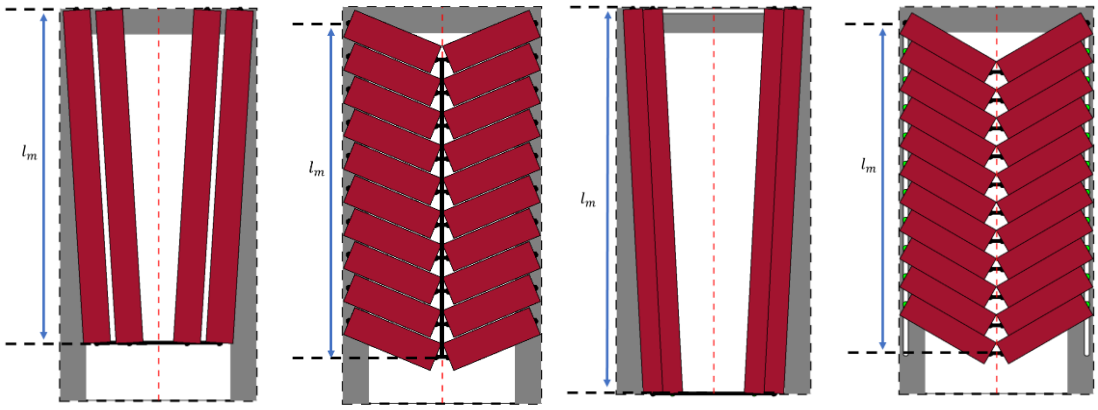

(**a**) (**b**) (**c**) (**d**)

Figure 2.5 Muscle length for bipennate muscle bundles with (a) laterally arranged fibers and pinned boundary condition, (b) centrally arranged fibers and pinned boundary condition, (c) laterally arranged fibers and fiber contact boundary condition, and (d) centrally arranged fibers with fiber contact boundary condition.

2.3 Effects of pennation angle on bundle actuator performance

2.3.1. Muscle force-strain behavior

In order to understand the implications of varying fiber pennation angle on actuation performance, the muscle and fiber behavior during actuation are evaluated for a range of initial fiber pennation angles with the two fiber boundary conditions. Table 2.1 shows the initial braid angle of the mesh sleeve for each fiber as well as the prescribed bounding box parameter dimensions used throughout the study.

Table 2.1 System parameters.

Parameter	**Variable**	**Value**
Initial braid angle	α_i	$30°$
Bounding length	L	$30.48\ cm\ (12\ in)$
Bounding width	W	$15.24\ cm\ (6\ in)$
Bounding depth	D	$2.54\ cm\ (1\ in)$

Muscle force F_m is computed with the nonlinear force-strain relationship represented by the ideal virtual work model

$$F_m = n\pi r_{f,i}^2 P\left(a\left(1-\varepsilon_f\right)^2 - b\right)\cos(\beta) \tag{10}$$

$$\beta = sin^{-1}\left(\frac{sin(\beta_i)}{\varepsilon_f}\right)$$

$$a = \frac{3}{tan(\alpha_i)^2} \qquad b = \frac{1}{sin(\alpha_i)^2}$$

where P is the pressure supplied to each fiber, and a and b are constants related to the initial braid angle. Figure 2.6 illustrates muscle force with respect to muscle strain at a constant applied pressure of $345\ kPa\ (50\ psi)$ for different bipennate muscle topologies and fiber constraints. We note that for some initial pennation angles with the fiber contact boundary condition, the muscle strain becomes negative, indicating extension of the muscle, or experiences a direction reversal where it initally extends then contracts during actuation. For the pinned boundary condition, the muscle strain is always contractile but the maximum strain depends strongly on

the initial pennation angle.

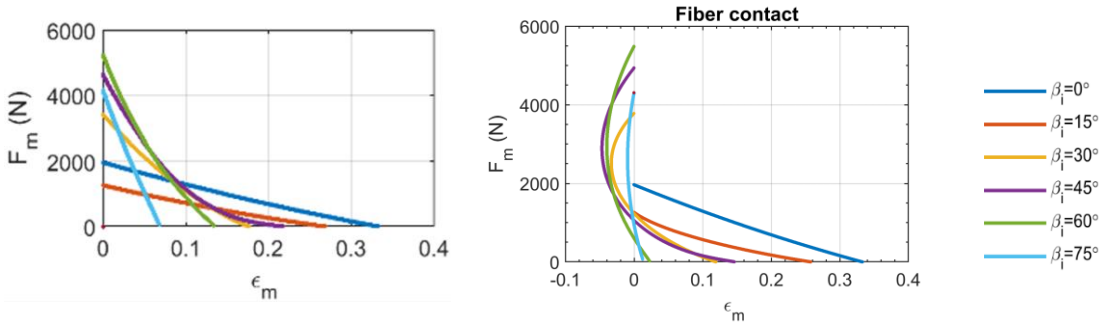

(**a**) (**b**)

Figure 2.6 Muscle force- muscle strain behavior of parallel ($\beta_i = 0°$) and bipennate muscle bundles with pinned boundary condition (a)) and fiber contact boundary condition (b). The legend shown on far right indicates the fiber pennation angle of the muscle topology.

To understand this behavior we consider the relationship between muscle strain ε_m and fiber strain ε_f where

$$\varepsilon_m = \frac{\Delta l_m}{l_{m,i}} \tag{11}$$

$$\varepsilon_f = \frac{\Delta l_f}{l_{f,i}}$$

The muscle length l_m is defined as the distance, in the direction of muscle displacement, between the outer attachment point for the first pair of fibers and the inner attachment point of the last pair for fibers. Note that the center-to-center spacing between fibers in the fiber contact boundary condition changes with respect to fiber radial expansion and axial contraction, whereas

it remain fixed in the pinned boundary condition. This is depicted in Figure 2.5 for pinned fibers and fibers in contact. These variations in muscle length are expressed as

$$l_m = \begin{cases} l_f \text{ for parallel fibers} \\ l_f \cos(\beta) \text{ for bipennate lateral fibers} \\ \left(\frac{n}{2} - 1\right)\frac{2r_f}{\sin(\beta)} + l_f \cos(\beta) \text{ for bipennate central fibers} \end{cases} \quad (12)$$

Muscle displacement Δl_m is measured as $\Delta l_m = l_{m,i} - l_m$ where $l_{m,i}$ is the initial muscle length. The muscle strain increases at the same rate as fiber strain increases for the parallel muscle topology due to the fibers running parallel to the axis of muscle motion. It should be noted that a bipennate muscle with an initial pennation angle of 90° is incapable of muscle contraction along the direction of muscle motion.

Figure 2.7 plots muscle strain as a function of fiber strain. It shows that, in rotation-limited topologies ($\beta_i \geq 41.86°$), as initial pennation angle increases, the fiber strain decreases due to decreasing range of fiber rotation. Hence, as initial pennation angle increases for bipennate muscle topologies with the fiber contact boundary condition, the fiber strain increases at a faster rate than muscle strain. Furthermore, the negative (extensile) muscle strains exhibited by the fiber contact boundary condition with sufficiently large β_i indicate the contribution of the fiber radial expansion along the length dimension of the bounding envelope dominates the contribution of the fiber axial contraction.

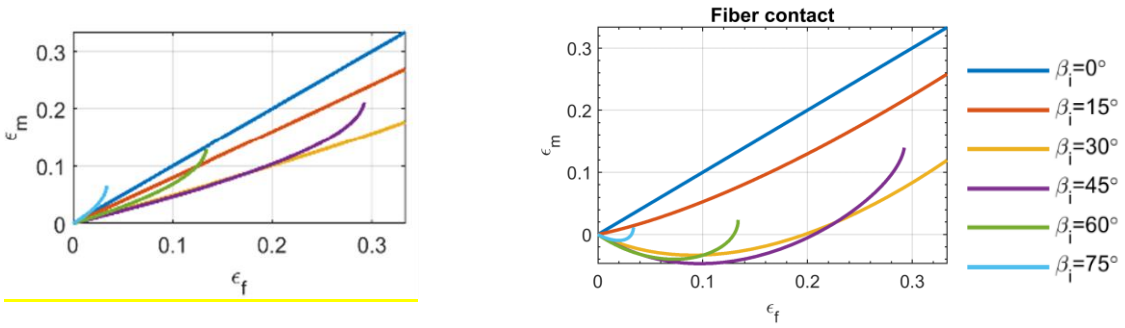

(**a**) (**b**)

Figure 2.7 Muscle strain- fiber strain behavior of parallel ($\beta_i = 0°$) and bipennate muscle bundles with pinned boundary condition (a)) and fiber contact boundary condition (b). The legend shown on far right indicates the fiber pennation angle of the muscle topology.

Figure 8 dissects the muscle contraction behavior during actuation to show the contributions to overall muscle contraction from the radial expansion and axial contraction for a $\beta_i = 30°$ bundle with fiber contact boundary conditions. In the initial stage of actuation, the radial expansion dominates the axial contraction such that the muscle experiences extensile motion. This elongation behavior will occur until the fiber axial contraction overcomes fiber radial contraction and drives the muscle to contract. However, depending on the muscle topology, the fiber axial contraction may never surpass the fiber radial expansion enough to enable muscle contraction. Similar effects have been reported natural muscles; fiber pennation angles above approximately $55°$ have been shown to be incapable of producing muscle shortening in myomeres of fishes [54]. Biological muscles vary muscle thickness to impose the isovolumetric constraint on the muscle while the artificial muscle bundle considered here keeps muscle thickness constant via the rigid frame that supports the outer muscle connections. The drawback of maintaining a constant muscle thickness is that it reduces the extent of fiber rotation, ultimately impacting muscle contraction. However, the pinned fiber boundary condition counters

this drawback by eliminating the muscle elongation behavior through precisely locating the fibers such that fiber contact is avoided and does not interfere with muscle motion.

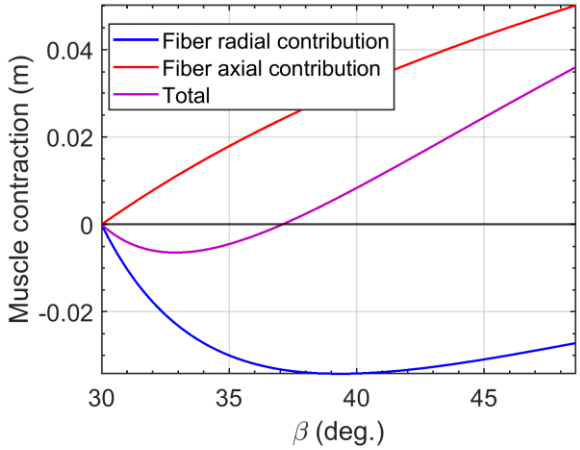

Figure 2.8 Variation in fiber radial and axial contributions to total muscle contraction with fiber pennation angle for a $\beta_i = 30°$ bundle with fiber contact boundary conditions.

The muscle force-strain behavior for a bipennate muscle topology that experiences both extensile and contractile motion is broken down to illustrate the muscle displacement direction reversal in Figure 2.9. Figure 2.9(a) illustrates the muscle force during actuation for a bipennate muscle of an initial pennation angle of $45°$ under the fiber contact constraint. A constant pressure of $345\ kPa$ $(50\ psi)$ is supplied to all the fibers. The series of images in Figure 2.10(b) provide visual snapshots of the muscle state at different stages of muscle actuation. The distance between the upper and lower blue lines is the muscle length at the specified actuation. The figure illustrates that as the muscle contracts from the initial (blocked force) condition, the fiber radial expansion dominates the muscle motion and the muscle begins to extend while the muscle force decreases. Once the fiber axial contraction overcomes the fiber radial expansion, the muscle transitions to contractile motion. Thus, the muscle can experience the same muscle strain at different stages of fiber contraction as can be seen at point (3) where the muscle topology

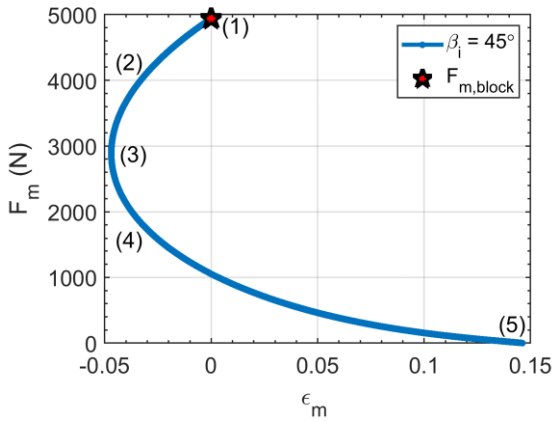

(**a**)

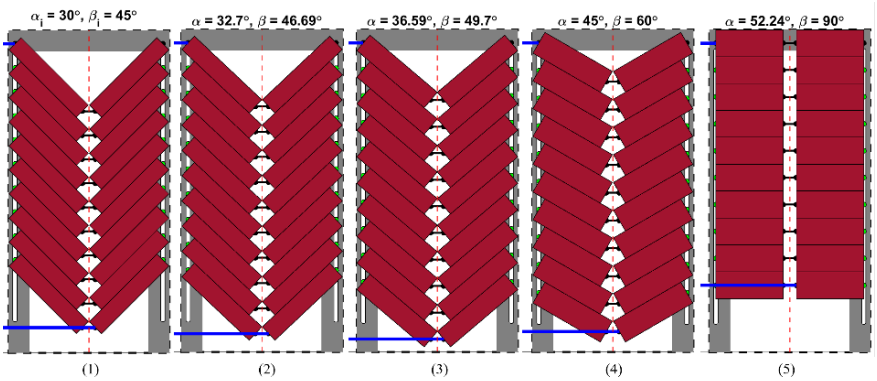

(**b**)

Figure 2.9 (a): Muscle force- muscle strain behavior of bipennate muscle bundle with $\beta_i = 45°$ and fiber contact boundary condition. The numbered label on the plot indicates sequential change in muscle force and muscle strain during fiber actuation. **(b):** Visual representation of bipennate muscle bundle motion with fiber contact boundary condition. Each numbered image corresponds to different stages in fiber actuation and aligns with the numbered labels in (A). (1) is the initial or blocked force condition, (2) is $\varepsilon_m = -0.025$ during extensile motion, (3) is $\varepsilon_m = -0.025$ during contractile motion, (4) is when the muscle returns to its initial muscle length, and (5) is the free muscle contraction condition.

appears noticeably dissimilar to point (2) even though $\varepsilon_m = -0.025$ in both cases. Depending on the muscle topology, the contractile motion may be capable of bringing the muscle back to the original muscle length as seen at point (4) and transition to muscle contraction as seen in point (5). However, for some other bipennate muscle topologies with the fiber contact constraint applied, the fiber axial contraction is incapable of overcoming the fiber radial expansion. This results in the muscle only experiencing extensile motion.

Analogous to architectural gear ratio (AGR) in biomechanics studies, transmission ratio can be used to relate the fiber behavior to the muscle behavior. The transmission ratio TR analyzed in this study is defined as the ratio of change in muscle length to the change in fiber length as shown in Eq. (13).

$$TR = \frac{\Delta l_m}{\Delta l_f} \tag{13}$$

Figure 2.10 shows how the transmission ratio varies with respect to fiber pennation angle for different fiber boundary conditions. In the parallel topology, the muscle contraction rate and fiber contraction rate are equivalent (i.e. $TR = 1$) because no fiber rotation occurs. The transmission ratio for the parallel muscle topology is shown as a red star marker. A transmission ratio greater than one indicates the muscle topology amplifies fiber contraction; a ratio less than one indicates the topology reduces contraction. Figure 9 shows that for all bipennate muscles, the transmission ratio increases as pennation angle increases. The rates of change of transmission ratio with pennation angle observed here differ from that previously reported for bipennate bundle actuators with fixed fiber geometries due to the spatial constraint on muscle envelope and corresponding fiber sizing considered here [39]. The pinned fiber boundary condition analysis shows that all bipennate muscle topologies considered produce transmission ratios greater than 1.

For bipennate muscles with fibers in contact, both positive and negative transmission ratios are observed and ratios are generally less than 1. The negative transmission ratio values align with the elongation behavior observed in bipennate muscles with the fiber contact boundary condition that was seen in Figure 2.6(b) and 2.7(b). Knowledge of bipennate variable gearing and muscle force-strain space gives insight to match muscle output demands of speed or force for a broad range of movements.

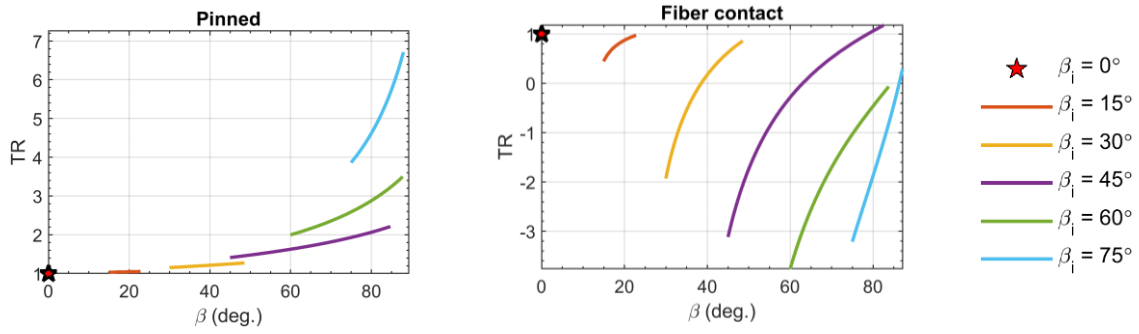

(**a**) (**b**)

Figure 2.10 Variation in muscle transmission ratio of parallel ($\beta_i = 0°$) and bipennate muscle bundles with pinned boundary condition (a) and fiber contact boundary condition (b). The legend shown on far right indicates the fiber pennation angle of the muscle topology.

2.3.2. Peak muscle displacement

The peak muscle displacement reaches a maximum and then decreases significantly as the initial fiber pennation angle increases as shown in Figure 2.11. However, this relationship is nonlinear due to the extent of fiber contraction and rotation behavior in the muscle bundle. At small initial pennation angles, the fibers are arranged laterally where the fiber length makes a larger contribution to the muscle length. The fiber lengths at small initial pennation angles for bipennate muscles are almost equivalent to fiber lengths of the parallel muscle as shown in Figure 2.12.

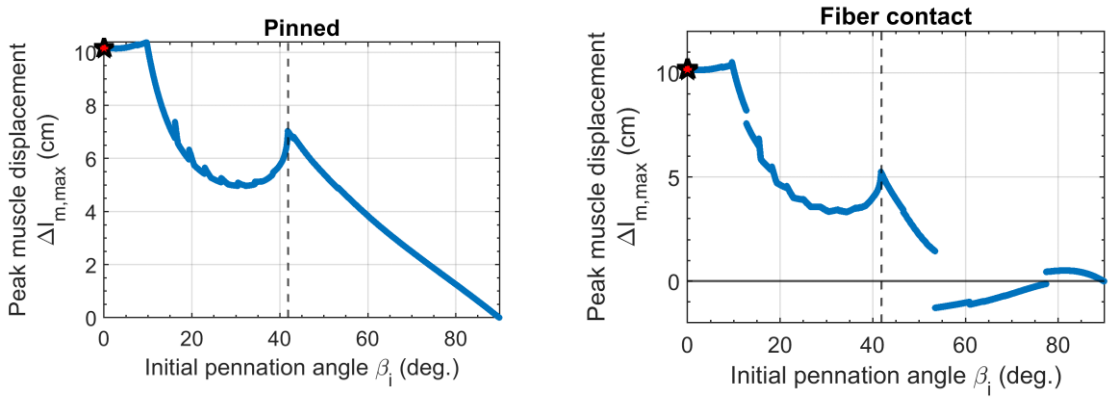

(**a**) (**b**)

Figure 2.11 Variation in peak muscle displacement for muscle bundle design with (a) pinned boundary condition and (b) fiber contact boundary condition. Red star indicates a parallel ($\beta_i = 0°$) muscle bundle topology and dashed vertical line indicates the boundary between fiber contraction-limited (left of line) and fiber rotation-limited (right of line) topologies.

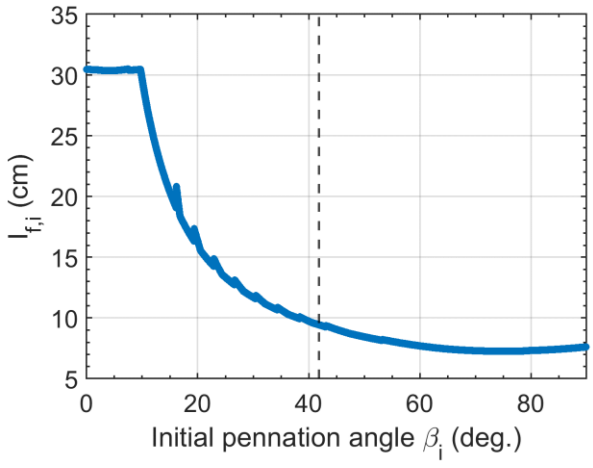

Figure 2.12 Variation in initial fiber length with initial pennation angle with the pinned boundary condition. The dashed vertical line indicates the boundary between fiber contraction-limited (left of line) and fiber rotation-limited (right of line) topologies.

This is due to the fibers being contraction-limited and the length dimension of the bounding envelope determine the initial fiber length. Fibers at these small initial pennation angles rotate with fiber contraction and assists in muscle contraction such that the peak muscle displacement exceeds that of the parallel topology. As the initial pennation angle increases, the initial fiber length is increasingly driven by the width dimension of the bounding envelope and thus decreases. This is even more so for rotation-limited fibers since the fibers need to fully rotate.

One may intuitively assume that a bipennate configuration in which the fibers simulaneaously fully contract and fully rotate should result in a greater muscle displacement as compared to a parallel topology. In fact, this was observed in a previous study that considered fibers of *prescribed length* with varying initial pennation angle [39]. Our analysis of the prescribed bounding envelope case condidered here partially supports this intuition as the peak muscle displacement of bipennate muscle topologies approaches a local maximum at the fiber contraction-rotation limited boundary. However, this local maximum is noticeably less than the peak muscle displacement of the parallel topology since the combination of fiber sizing, rotation, and boundary conditions dictate the extent of muscle contraction. This is a direct implication of the prescribed bounding volume and design objective of effectively utilizing the available space. The small jumps in the peak muscle displacement are associated with the changes in the number of fibers in the muscle bundle. We also note that for a range of bipennate muscle topologies with the fiber contact boundary condition, the peak muscle displacement falls below zero, indicating those configurations have a larger magnitude of extension than compression resulting in a peak muscle displacement in the extensile direction.

2.3.3. Muscle blocked force

The muscle blocked force (i.e. the force at zero strain) varies nonlinearly with initial pennation angle. This condition represents the maximum force generation of the muscle and can be expressed as a function of applied pressure and initial pennation angle as

$$F_{m,block} = F_m|_{\varepsilon_f=0} = n\pi r_{f,i}^2 P(a-b)\cos(\beta_i) \tag{14}$$

The muscle blocked force is generally expected to increase with increasing initial fiber pennation angle since a larger number of fibers can be packed in the muscle bundle. However, this is not always the case for spatially bounded muscle bundles as seen in Figure 2.13 due to the fiber arrangement.

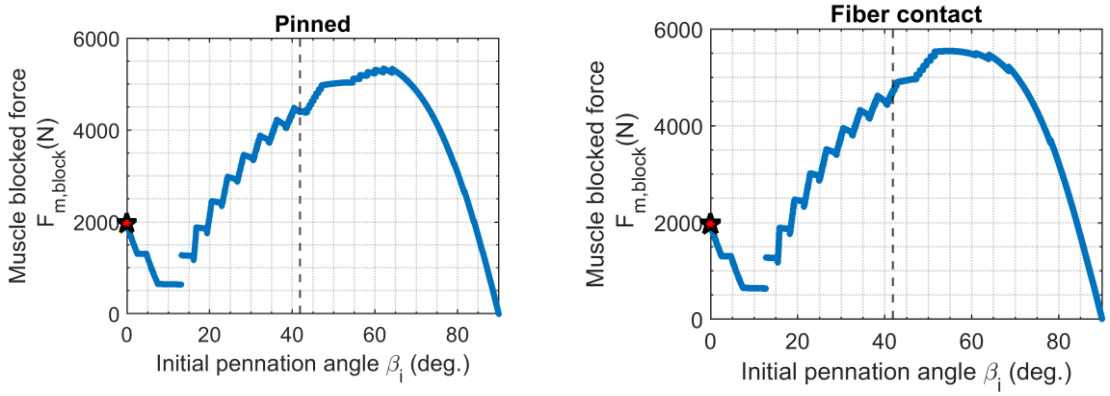

(**a**) (**b**)

Figure 2.13 Variation in muscle blocked force at a constant applied pressure of $345kPa$ $(50\ psi)$ with initial pennation angle for (a) pinned boundary condition and (b) fiber contact boundary condition. Red star indicates a parallel ($\beta_i = 0°$) topology and dashed vertical line indicates the boundary between fiber contraction-limited (left of line) and fiber rotation-limited (right of line) topologies.

The lateral or central arrangement of the fibers depend on the number of fibers that can fit along the width of the bounding envelope n_w and number of fibers that can fit along the length of the bounding envelope n_l. Figure 2.14 illustrates the range of initial pennation angles where fibers are laterally and centrally arranged. The fiber contact boundary condition shows a similar trend in number of fibers, but the lack of clearance space between the fibers permits additional fibers to fit in the bounding envelope at certain initial pennation angle values.

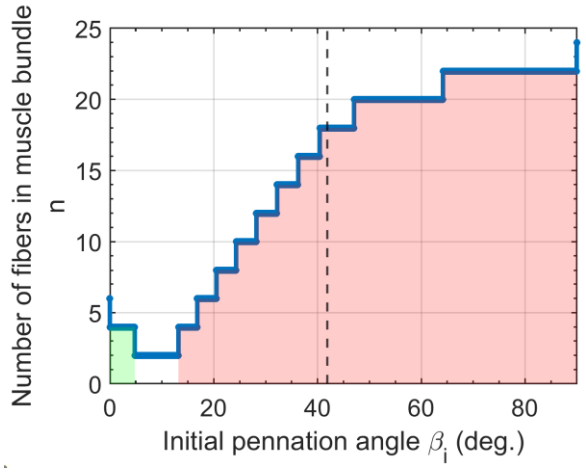

Figure 2.14 Variation in number of fibers in muscle bundle with initial pennation angle with the pinned boundary condition. Green shaded region is associated with laterally arranged fibers and pink shaded region indicates centrally arranged fibers. White region indicates where only one pair of fibers can fit in the prescribed bounding envelope.

The fiber diameter also plays a part in fiber arrangement and force capacity. The initial fiber radius depends on the contraction-rotation behavior such that contraction-limited fibers have an appropriate initial fiber radius to enable full radial expansion while rotation-limited fibers can have larger radii depending on the extent of radial expansion as shown in Figure 2.15.

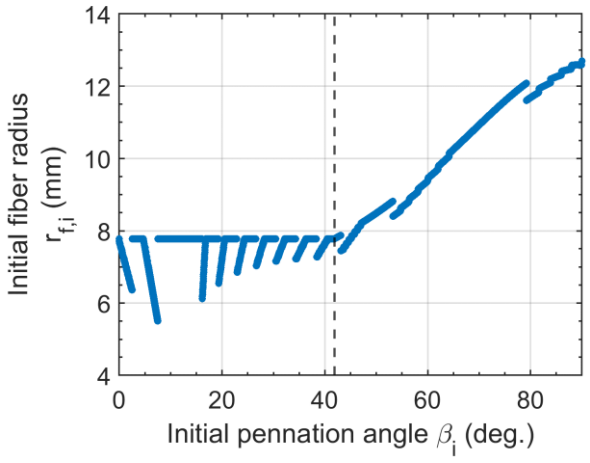

Figure 2.15 Variation in initial fiber radius with initial pennation angle with the pinned boundary condition. The dashed vertical line indicates the boundary between fiber contraction-limited (left of line) and fiber rotation-limited (right of line) topologies.

The fiber radius and length do not vary with respect to fiber boundary conditions. Thus, for a given initial pennation angle, the muscle bundle blocked force profile with the fiber contact condition is equal to (in cases where the same number of fibers are present) or slightly larger than (in cases where additional fibers are present) that with the pinned condition as showed in Figure 13. The jumps in the blocked force profiles correspond to variation in the number of fibers in the muscle bundle. This analysis also shows a large range of bipennate muscle topologies can achieve a muscle blocked force significantly greater than that of the parallel muscle topology, with the largest blocked force configuration exhibiting more than 2.5 times that of the parallel topology. Although the fiber clearance required by the pinned condition decreases the number of fibers in the muscle bundle compared to the fiber contact condition, the pinned condition is generally comparable to that of the fiber contact condition.

2.3.4. Muscle stiffness

In understanding the muscle force-strain relationship, the muscle displacement direction reversal suggests bipennate muscle topologies can be designed as both a positive and/or negative stiffness structure. In this analysis, the following formulation is used to compute the muscle stiffness k_m behavior during actuation.

$$k_m = \frac{dF_m}{d\Delta l_m} = \frac{\frac{\partial F_m}{\partial \alpha}}{\frac{\partial \Delta l_m}{\partial \alpha}} \tag{15}$$

The applied pressure is held constant at $345\ kPa$ $(50\ psi)$ to observe the stiffness during isobaric contraction. Figure 16 shows that operating stiffness decreases with increasing pennation angle for muscle topologies with pinned fiber boundary condition, but stiffness always remains positive. Negative stiffness behavior is observed in muscle topologies with fibers in contact as the muscle length increases with decreasing force. Figure 2.17 illustrates a bipennate muscle with fiber contact that transitions from extensile to contractile motion. The stiffness approaches an asymptote or an instance of infinite stiffness when the muscle transitions from extensile to contractile motion. This infinite stiffness occurs at a mechanical singularity where the fiber radial expansion and axial contraction can no longer allow the muscle to extend without violating the fiber contact boundary condition constraint. This mechanical singularity prevents a conclusive statement to be made on the operating stiffness range for muscle topologies with the fiber contact boundary condition. On the other hand, the operating stiffness range for muscle topologies with pinned fibers increases with muscle topologies approaching the fiber contraction and rotation-limited boundary, where the fibers in the muscle can fully contract and fully rotate.

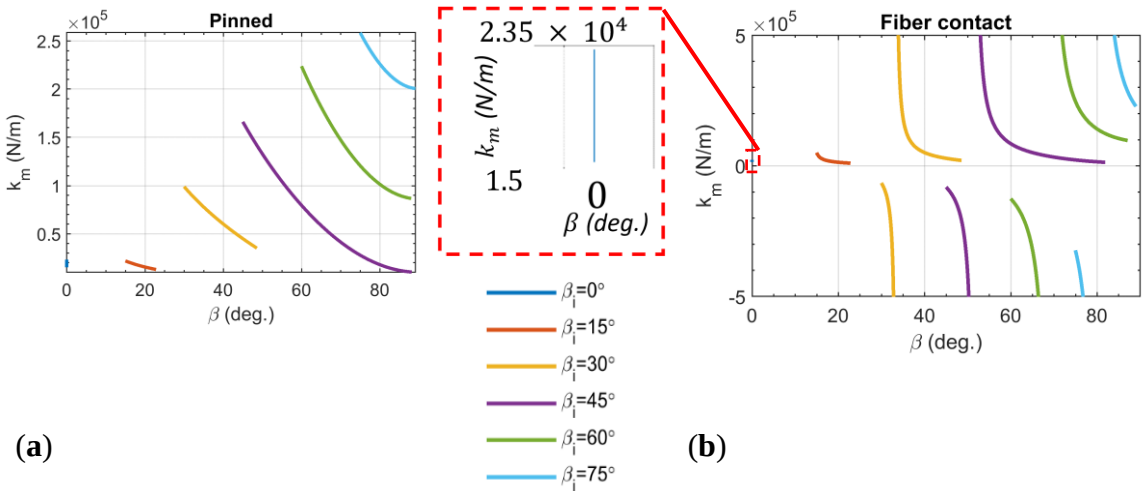

Figure 2.16 Variation muscle stiffness behavior of parallel ($\beta_i = 0°$) and bipennate muscle bundles with pinned boundary condition (a) and fiber contact boundary condition (b). The legend shown on far right indicates the fiber pennation angle of the muscle topology. The inset plot shown in the red dashed box illustrates the muscle stiffness range for a parallel muscle bundle. The muscle stiffness range for the parallel topology is the same for both boundary conditions.

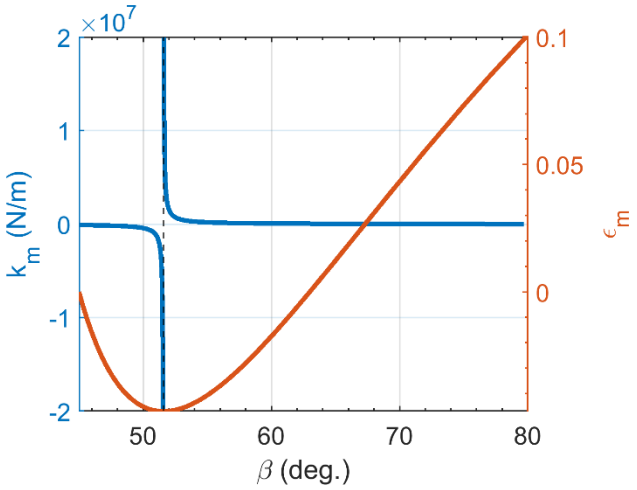

Figure 2.17 Realized negative muscle stiffness behavior for bipennate muscle bundles with fiber contact boundary condition. Blue profile illustrates variation in muscle stiffness during fiber actuation and orange profile corresponds to change in muscle strain during fiber actuation.

2.3.5. Isobaric work output

Although a clear tradeoff is observed between muscle output force and muscle displacement, the isobaric work provides a more complete understanding of the muscle output capacity. Isobaric work output is evaluated by understanding the muscle force behavior during actuation at a constant pressure. Equivalent pressure of $345\ kPa\ (50\ psi)$ is supplied in this analysis to observe an impartial comparison.

$$W_{isobaric} = \int_{l_{m,i}}^{l_{f,free}} F_m dl_m \tag{16}$$

Isobaric work depends on muscle output force so it is expected for the isobaric work to resemble that of the muscle blocked force as seen in Figure 2.15. However, this is not true for bipennate muscle topologies with the fiber contact boundary condition shown in Figure 2.18(b). The negative work corresponds to the muscle topologies that experience the extensile motion. Although the peak muscle displacement analysis in Figure 2.11(b) shows a smaller range of bipennate muscle topologies with the fiber contact boundary condition where the extensile motion exceeds that of the contractile motion while the isobaric work output capacity shows a larger range of bipennate muscle topologies where the extent at which the elongation motion does not contribute to positive isobaric work. The jumps in the profile are associated with change in the number of fibers in the muscle bundle. Since elongation behavior does not exist for muscle topologies with the pinned boundary condition, the isobaric work is always positive as seen in Figure 2.18(a). Furthermore, it shows a bipennate muscle topology with the pinned boundary condition can be designed with an isobaric work output capacity larger than that of the parallel muscle topology of the same size.

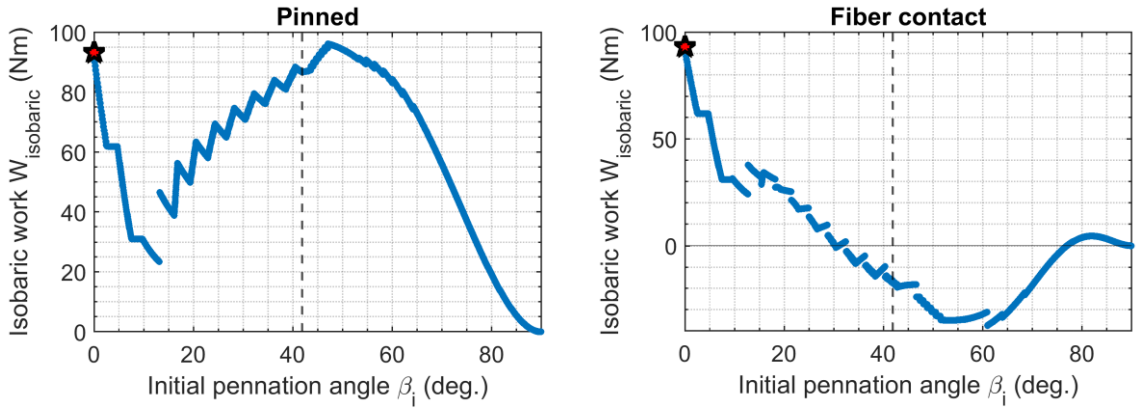

(**a**) (**b**)

Figure 2.18 Variation in isobaric work output capacity with initial pennation angle for (a) pinned boundary condition and (b) fiber contact boundary condition. Red star indicates a parallel ($\beta_i = 0°$) muscle bundle topology and dashed vertical line indicates the boundary between fiber contraction-limited (left of line) and fiber rotation-limited (right of line) topologies.

2.3.6. Isotonic work output

Isotonic work output is evaluated by understanding the muscle behavior during muscle actuation with a constant load F_{load} is applied. The following expression is used to compute isotonic work.

$$W_{isotonic} = F_{load} \int_{l_{m,i}}^{l_{m,free}} dl_m \tag{17}$$

Figure 19 shows that isotonic work scales linearly with the applied load for a given β_i. The isotonic work profile in Figure 2.19 resembles the peak muscle displacement seen in Figure 2.11 since isotonic work depends on the muscle displacement behavior of the muscle. There are bipennate muscle topologies capable of isotonic work that slightly exceeds that of the parallel muscle topology with either boundary condition. Similar to isobaric work of muscle topologies

with the fiber contact boundary condition, the negative isotonic work observed in bipennate muscle topologies with the fiber contact boundary condition is a result of the extension behavior.

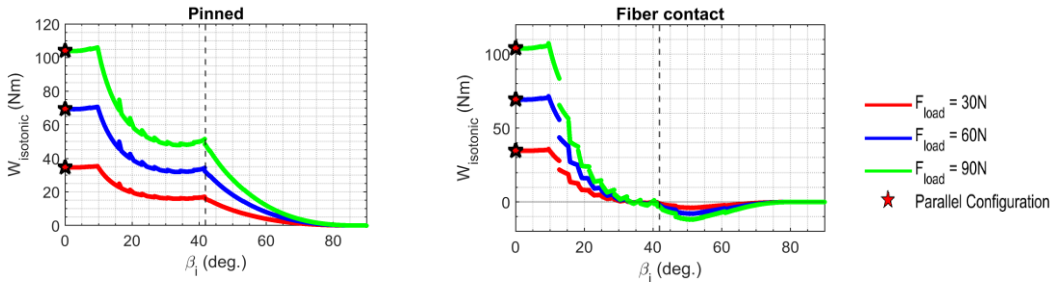

(**a**) (**b**)

Figure 2.19 Variation in isotonic work output capacity of parallel ($\beta_i = 0°$) and bipennate muscle bundles with pinned boundary condition (a) and fiber contact boundary condition (b). The legend on the far right indicates the fiber pennation angle of the muscle topology.

2.4 Conclusion

This paper establishes a method of designing bipennate fluidic artificial muscle bundle topologies under spatial bounding volume constraints. The muscle bundles were parameterized for effectively utilizing the prescribed bounding envelope. Two fiber boundary conditions – fiber contact and pinned – were explored to investigate the implications of incorporating an idealized bioinspired connective tissue functionality as compared to maintaining clearance between fibers via fixed pin joints, respectively. The analysis revealed that, for the given spatial volume constraint, bipennate topologies can be found to produce muscle output force, muscle contraction, muscle stiffness, or work output capacity larger than that of a parallel muscle bundle topology. Thus, depending on the fiber boundary conditions, a bipennate bundle may offer distinct advantages over a more conventional parallel bundle.

The fiber contact boundary condition enables additional fibers to be packed into the fixed bounding envelope through elimination of minimum fiber clearance required in the pinned boundary condition. However, due to decreased contraction, fiber contact configurations produces less work output than pinned configurations over most of the range of initial pennation angles. Contrary to intuition, configuring a bipennate topology to simulataneously maximize fiber contraction and fiber rotation does not yield the largest muscle stroke and results in less contraction than that of a parallel topology with equal bounding envelope. Rather, peak muscle displacement is produced by a bipennate topology with a small (but non-zero) initial pennation angle that exploits both longer fibers and rotation effects. In addition, analysis of muscle behavior found that competing effects of fiber axial contraction and radial expansion in the fiber contact boundary condition determine the overall muscle motion such that a bipennate topology can exhibit extensile motion. The extensile motion found in muscle topologies with the fiber contact bounding condition also enables the bipennate muscle topology to behave as a negative stiffness structure. Furthermore, mechanical singularity was discovered as a byproduct of the fiber contact boundary condition.

Future work will include experiments to investigate these trends in bipennate muscle bundles with the fiber contact boundary condition. To advance our understanding in the design of pennate muscle topologies, future work should explore implications of muscle topology design on efficiency in tracking a dynamic motion and evaluate muscle performance sensitivity to variation in muscle thickness during actuation.

CHAPTER 3: Genetic algorithm-based optimization of spatially constrained pennate fluidic artificial muscle bundle

3.1 Introduction

Human muscle tissues, like other biological systems, have been evolutionarily optimized over generations based on our ancestors' environments and needs to survive. This has enabled the body to pack a sizeable number of actuators into a limited amount of space and perform a variety of kinematic behaviors. Natural skeletal muscles generate tension by shortening sarcomeres in muscle fibers. Tension is created when myosin heads attach to actin to form crossbridges, where the heads pull the actin to shorten the length of the sarcomere. Thus, the generated force is directly related to the sarcomere length. Sarcomeres run the length of the muscle fiber and are recruited as needed to obtain the desired contractile force. Groups of muscle fibers stimulated by a common motor neuron forms a motor unit inside a muscle fascicle. A skeletal muscle comprises of hundreds to thousands of muscle fascicles held together by connective tissue. The actuation elements, or motor units, are distributed in the muscle tissue such that the muscle fascicles can be assembled, positioned, and sized in various formations [29,30,55]. The muscles works in antagonistic paris to perform various tasks, where one muscle contracts while the other muscle relaxes. Researchers have observed notable differences in actuation behavior with varying muscle architecture types, of which the parallel and pennate configurations are studied the most and commonly used to discuss these architectural tradeoffs [28,51,52,54]. The long fascicles in the parallel musculature are aligned parallel to the line of motion and take advantage of the longitudinal arrangement to generate large contractions. Fascicles in convergent muscles are arranged in a fanned configuration and attach to a common point on a tendon. In contrast, the fascicles in the pennate musculature are shorter, where the tendon for pennate muscles span the length of the muscle and fascicles are attached to the tendon at an oblique angle. As the fascicles contract, they pivot about the attached location on the tendon. Consequently, this allows the muscle to have a larger number of fibers and

produces more force. A comparison of these two architectures of similar anatomical size shows the pennate topology capable of generating a greater amount of force but at the cost of less contraction [43]. Furthermore, the shape, and size of these muscle tissues depend on their function and location in the body. We see this in the hamstring and quadricep muscle groups, where the bicep femoris in the hamstrings have a parallel musculature and the rectus femoris in the quadriceps are bipennate. Both of these muscles act on the hip and knee joint but are attached to different bones in the body and collaborate with other existing muscles to perform different flexion and extension motions [56]. A hierarchical activation scheme is used to selectively stimulate motor units synchronously to produce contraction and generate motion. This architecture and control structure can be leveraged in robotics to improve energy efficiency, bandwidth, and variable stiffness control [57–60]. Applying this approach to soft, muscle-inspired actuators allows for topological freedom not possible with traditional robotic actuation systems like motors and pistons.

Of the existing soft actuators in the literature, the McKibben muscle or fluidic artificial muscle (FAM) is one of the most attractive to the robotics research community due to its inherent compliance, ease of fabrication, and high force-to-weight ratio. A study found an antagonistic pair of FAMs achieve a force-to-weight ratio six times greater than that of an equivalent double-acting cylinder. [61] The fluidic artifical muscle was firsst invented by Richard Gaylord in the later 1950s but popularized by Joseph McKibben in the late 1960s, when he developed it as an orthotic appliance for polio patients. A FAM is composed of an elastomeric tube and braided mesh sleeve or sheath. Pneumatic or hydraulic fluid pressure is used to radially expand the inner bladder and the fiber wrap design of the mesh sleeve guides the mechanism to produce tensile force and contract axially [32,62]. FAMs can be sized, oriented, and organized into a bundle to create a variety of topologies, force-displacement behaviors, and differing dynamic responses much like

the fascicles in natural human muscle tissues. FAMs exhibit similar force-contraction behavior to skeletal muscle fascicles, where applied pressure determines the force output and extent of contraction. While motor neurons are used to regulate force and contraction of natural muscles, control valves are used to vary the applied pressure in FAMs. Although FAMs observe similar contractile force behavior, the quasi-static assumption in the FAM model indicates the generated force is not velocity dependent when applied pressure is held constant.

Current literature mostly focuses on the kinematic behavior of FAMs arranged in parallel [63–67]. Although this parallel topology is one embodiment of a hierarchical actuator, there are sparse studies in the present literature that explore other configurations. In 2013, Azizi and Roberts were the first to arrange FAMs in a unipennate array and found the presence of variable gearing similar to that found in natural muscles [42]. This variable gearing is unique as it is made possible solely due to the pennate architectural feature. Jenkins et al. discuss how the mutable configuration of this pennate muscle architectural design can be leveraged to create a soft variable stiffness actuator [39,50]. In a previous study, Jenkins et al. presented a model to describe the coupled relationship between force, speed, and stiffness of individual FAMs to that of the bundle and experimentally validated the model by arranging the FAMs in a bipennate array. To obtain a more complete understanding of this pennate architectural feature, we recently performed a comparative study that quantified the effects of pennation angle on spatially constrained FAM bundle performance. The findings illustrated that careful selection of the pennation angle, can alter the number, sizing, arrangement, and distribution of FAMs in the bundle and augment performance characteristics compared to that of a parallel FAM bundle subject to equivalent spatial bounds [68]. Although models of the parallel and pennate FAM bundles have been developed and demonstrated, it is unclear under what conditions which topology should be selected. A purely biomimetic approach

to FAM bundle design may not be optimal given the requirements and constraints on a human can be drastically different from those on a legged robot or wearable assistive device. Thus, a strategic method of spatially optimizing FAM bundle design is needed. The optimal FAM bundle topology will likely differ based on the optimization cost function(s) or desired objective(s) as well as different geometric constraints. This work presents a genetic algorithm-based optimization framework that enables us to generate different FAM bundle designs and evaluate changes to the optimal design based on spatial constraints as well as objective. The FAM bundle designs presented in this study are inspired by the fascicle arrangements observed in these skeletal muscle architectures, where individual FAMs in the bundle are analogous to muscle fascicles and pinned joints in the boundary condition are similar to the attachement points on the tendon. The parallel FAM bundle design adopts the parallel musculature while the pennate FAM bundle design with the centrally arranged FAMs takes on the pennate muscle architecutre. The fanned configuration in convergent muscles appear in the pennate FAM bundle design with laterally arranged FAMs. MATLAB simulations utilize the parameterized model to evaluate a FAM bundle design's force and stroke, allowing a multi-objective genetic algorithm (MOGA) to create Pareto frontiers of maximum force and maximum stroke subject to different spatial envelopes.

This paper first details the modeling and parameterization of a fluidic artificial muscle (FAM) bundle. Next, the MOGA problem formulation is described and implemented, and the resulting design trends are discussed. A selection of FAM bundle designs were chosed to experimentally validate trends seen in the generated Pareto frontiers. Then, the influence of the spatial envelope constraints on optimal FAM bundle design parameters is discussed. Finally, concluding remarks are made to highlight the contributions and limitations of this work and suggested directions for future study.

3.2 Methods

3.2.1 FAM bundle Modelling and Parameterization

The fluidic artificial muscle (FAM) was first invented by Richard Gaylord in the late 1950s but popularized by Joseph McKibben in the late 1960s, when he developed it as an orthotic appliance for polio patients. Among the many attractive properties of this type of soft actuator, its functional similarity to skeletal muscles in tension is the basis of its moniker as an 'artifical muscle'. The commonly used nonlinear force-strain relationship to describe FAM actuation behavior is derived from a virtual work method that assumes the artificial muscle takes the form of an idealized, thin-walled, pressurized cylinder. Changes to the artificial muscle dimensions are correlated to the planar network of jointed pantographs on the braided mesh sheath, where the braid angle increases during actuation. Given the initial braid angle α_0 and initial FAM radius and length (r_0 and l_0, respectively), the radial expansion and axial contraction can be described in terms of FAM contraction strain ε_f as shown below:

$$r(\varepsilon_f) = \frac{r_0}{\sin(\alpha_0)}\sqrt{1-(1-\varepsilon_f)^2 \cdot \cos^2(\alpha_0)} \tag{1}$$

$$l(\varepsilon_f) = (1-\varepsilon_f) l_0$$

Based on the conservation of energy, the tensile force produced by a FAM $F_{f,MR} = P\frac{dV}{dl} - V_b\frac{dW}{dl}$, where P is the fluid pressure applied to the inner bladder, dV is the interior volume change of the bladder, dl is change in the FAM length, and dW is the change in strain energy density in the volume of the bladder $V_b = \pi l_0(r_0^2 - [r_0 - t_0]^2)$. This model assumes an ideal cylindrical geometry and the braided fibers of the mesh sleeve are considered stiff and remain in contact with the inner bladder. Klute and Hannaford account for the elasticity of the inner bladder in their formulation of the FAM tensile force by introducing terms with respect to the change in strain

energy density stored in the volume of the bladder [34]. Mooney-Rivlin material constants (C_{10}, C_{01}) are used to describe the hyper elastic properties of the inner bladder. Thus, the resulting FAM force expression $F_{f,MR}(\varepsilon_f, P)$ depends on the contraction strain and fluid pressure to the inner bladder, where $a = \frac{3}{tan^2(\alpha_0)}$ and $b = \frac{1}{sin^2(\alpha_0)}$ are constants related to the initial braided mesh sleeve geometry. It should be noted this FAM model is not only dependent on the material properties of the bladder but also the wall thickness t_0 of the bladder.

$$F_{f,MR}(\varepsilon_f, P) = \pi \cdot r_0^2 \cdot P \cdot \left(a\left(1-\varepsilon_f\right)^2 - b\right) + \frac{V_b}{2l_0^3\left(1-\varepsilon_f\right)^3}\Bigg\{4(C_{10}+C_{01})l_0^2\big[-1+\big(1-\varepsilon_f\big)\big]^4 - \frac{4l_0^2\varepsilon_f\left(1-\varepsilon_f\right)^2\left(2-\varepsilon_f\right)\left(C_{10}+C_{01}\left[1-\varepsilon_f\right]^2\right)}{\left[-tan^2(\alpha_0)-1+\left(1-\varepsilon_f\right)^2\right]^2} + \frac{4l_0^2\left(C_{10}+C_{01}\left[1-\varepsilon_f\right]^4\right)}{tan^2(\alpha_0)+\varepsilon} - \frac{4l_0^2\left(1-\varepsilon_f\right)^4\left[C_{10}+C_{01}\left(-1+2\left(1-\varepsilon_f\right)^2\right]\right.}{tan^2(\alpha_0)}\Bigg\} \quad (2)$$

For multiple FAMs arranged in a pennate bundle, the total force of the bundle must consider the component of each individual FAM force acting along the direction of motion. Therefore, the expression for calculating the bundle force F_m includes the number of FAMs in the bundle n and the pennation angle β [42].

$$F_{m,MR}(\varepsilon_f, P) = n \cdot F_{f,MR}(\varepsilon_f, P) \cdot \cos\left(\beta(\varepsilon_f)\right) \quad (3)$$

FAMs in a pennate topology are subject to not only radial expansion and axial contraction but also rotation upon actuation. This rotation behavior depends on the contraction strain of the individual FAMs in the bundle.

$$\beta(\varepsilon_f) = \sin^{-1}(\frac{\sin(\beta_0)}{1-\varepsilon_f}) \quad (4)$$

Assuming the bundle thickness in Figure 1 remains constant during actuation, the extent of FAM contraction and rotation in the bundle varies depending on the intial pennation angle β_0. FAMs with a zero pennation angle are a special case of this pennate configuration and are identified as the parallel topology, where FAMs will only contract axially and expand radially. Maximum FAM contraction strain $\varepsilon_{f,max} = 1 - \frac{1}{\sqrt{3}cos(\alpha_0)}$ can be used to predict whether the FAMs in the bundle are contraction-limited, rotation-limited, or both. Contraction-limited FAMs can reach their full contraction potential at the free (zero force) contraction of the bundle such that $\varepsilon_{f,free} = \varepsilon_{f,max}$ is the FAM contraction strain at the free contraction of the bundle. However, they do not fully rotate; i.e. the pennation angle at the free contraction condition $\beta_{free} = \beta(\varepsilon_{f,max}) < 90°$. Rotation-limited FAMs can fully rotate such that $\beta_{free} = \beta(\varepsilon_{f,max}) = 90°$, but do not fully contract; i.e. $\varepsilon_{f,free} < \varepsilon_{f,max}$. For FAMs that are both contraction limited and rotation limited, $\beta_{free} = 90°$ and $\varepsilon_{f,free} = \varepsilon_{f,max}$.

3.2.2 MOGA problem formulation and FAM bundle optimization

Due to the combinatorial nature of this topology optimization problem, the genetic algorithm is selected as the optimization technique used to illuminate desirable topological properties of the FAM bundle based on the geometric constraints and desired actuation kinematics or objectives of interest. To heuristically determine optimal FAM bundle designs with specified geometric constraints, a MOGA is implemented using the FAM bundle model shown in Equation (1)-(4) from Section 2.1. An architectural tradeoff is expected between force and stroke based on our understanding of parallel and pennate topologies. Thus, the resulting Pareto-optimal frontier can

be used to characterize the tradeoffs between different FAM bundle designs and help inform design decisions.

The FAM bundle optimization problem is formuated below, where the design variable string $\boldsymbol{x} = [n \quad r_0 \quad \beta_0 \quad l_0]$ is subject to bounds and constraints:

$$\min\left(f_1(\boldsymbol{x}), f_2(\boldsymbol{x})\right) \tag{5}$$

$$\begin{aligned} s.t. \quad & 2 \le n \le 2\mathbb{N} \\ & 0 \le \beta_0 \le 90 \quad (^\circ) \\ & 0 < l_{bundle}(\boldsymbol{x}) \le L \quad (\text{in}) \\ & 0 < t_{bundle}(\boldsymbol{x}) \le \frac{W}{2} \quad (\text{in}) \\ & 0 < \max\left(2 \cdot r(\varepsilon_f)\right) \le D \quad (\text{in}) \\ & \min(\boldsymbol{x_v}) \le x_c \le max(\boldsymbol{x_v}) \quad (\text{in}) \\ & \min(\boldsymbol{y_v}) \le y_c \le \max(\boldsymbol{y_v}) \quad (\text{in}) \\ & \min(\boldsymbol{x_v}) \le x_i(\varepsilon) \le max(\boldsymbol{x_v}) \quad i = 1,2,3,4 \quad (\text{in}) \\ & \min(\boldsymbol{y_v}) \le y_i(\varepsilon) \le \max(\boldsymbol{y_v}) \quad i = 1,2,3,4 \quad (\text{in}) \end{aligned} \tag{6}$$

The fitness function $f_1(\boldsymbol{x}) = -F_{m,MR}(0,P) = -F_{b,MR}(P)$ is the FAM bundle blocked force to maximize the bundle output force and $f_2(\boldsymbol{x}) = -\Delta l_m\big(\varepsilon_f(F_{b,MR}(P) = 0)\big)$ is the FAM bundle free contraction to maximize the bundle stroke. FAMs in the bundle are homogeneous and assumed to be arranged in a bipennate array. The bounds on n enforce this assumption and constrain this design variable to positive and even integers. The FAM bundle design in this analysis considers a single-layer, two-dimensional array of FAMs based on the prescribed layout of the bundle within the specified bounds as shown in the three-dimensional illustration. The FAM bundle length

l_{bundle} and thickness t_{bundle} must remain within the specified length L and width W dimension of the spatial envelope, respectively.

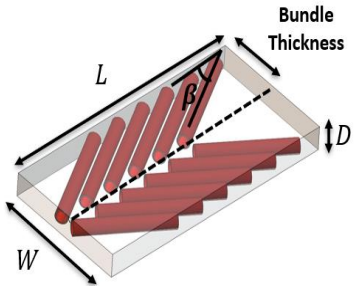

Figure 3.1. Three-dimensional illustration of FAM bundle circumscribed within specified length L, width, W, and depth D spatial bounds.

Thus, the FAM diameter must remain within the specified depth dimension D of the spatial envelope. The spatial envelope is assumed to be symmetrical with a uniform cross-section, and the bundle thickness is held constant during actuation. FAMs in the bundle are placed as close to the centerline as possible. A pinned boundary condition is considered as illustrated in Figure 3.2; one end of each FAM is assumed to be pinned to a rigid outer frame and the other end is attached to a central spine.

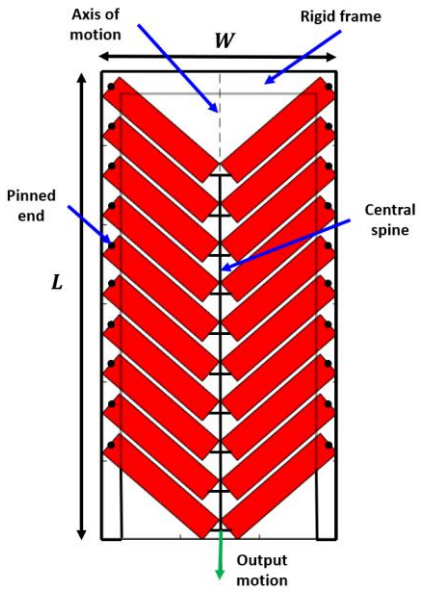

Figure 3.2. Pinned boundary condition of a bipennate muscle bundle in planar view. The rigid frame represents bounding envelope, with the length and width dimensions defined. FAM ends are pinned to the rigid frame and central spine.

In keeping with the assumed cylindrical geometry idealization, the projection of each FAM onto the planar view is a rectangle defined by the coordinates shown in Figure 3.3. Figure 3.3 illustrates the pinned coordinate position (x_c, y_c) of the top-most or inner-most FAM placement for centrally arranged or laterally arranged FAMs, respectively, where $x_c = \frac{W}{2} - \max\left(r(\varepsilon_f) \cdot cos\left(\beta(\varepsilon_f)\right) + l(\varepsilon_f) \cdot sin\left(\beta(\varepsilon_f)\right)\right)$ and $y_c = L - max\left(r(\varepsilon_f) \cdot sin\left(\beta(\varepsilon_f)\right)\right)$.

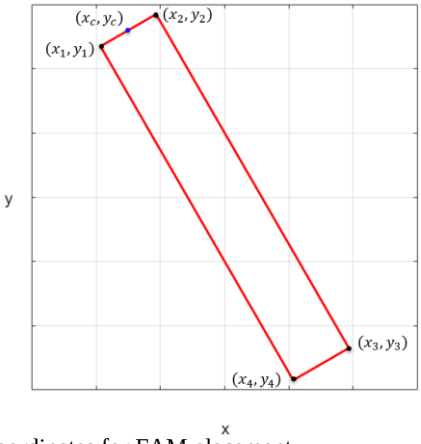

Figure 3.3. Planar visual of labelled coordinates for FAM placement.

$(\boldsymbol{x_v}, \boldsymbol{y_v})$ is the set of coordinate vectors that describe the planar shape of the spatial envelope. The four corner points shown are used to identify coordinate positions subject to the axial contraction, radial expansion, and rotational behavior of an individual FAM in the bundle. The top-most or inner-most FAM placement must be located inside the spatial envelope. These corner points are described for each pair of FAMs in the bundle and are used to ensure all FAMs in the bundle remains inside the spatial bounds for the entirety of its actuation.

Based on the established FAM model and understanding of FAM behavior during actuation, previous studies have shown pennate FAM bundle designs subject to equivalent spatial bounds can lead to two different FAM arrangements [69]. The laterally arrangement take on similar form to the fanned muscle fiber geometries found in our pectoral muscles, while the central arrangement aligns more closely to the bipennate musculature of the rectus femoris in our quadriceps.

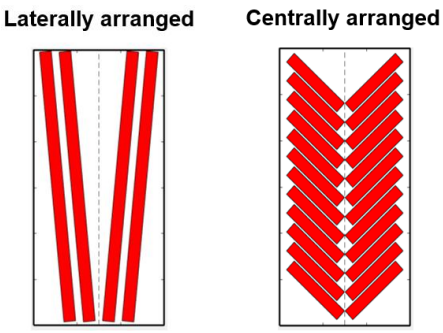

Figure 3.4. Two-dimensional illustration of different FAM arrangement designs for a FAM bundle.

The coupled relationship between the FAM bundle design parameters lead to notably different constraints depending on how the FAMs are arranged in the bundle. A FAM bundle with laterally arranged FAMs must account for the minimum clearance between FAMs along the width dimension Δx of the spatial envelope while the minimum clearance between FAMs is required along the length dimension $\Delta y$of the spatial envelope for centrally arranged FAMs. Consequently, the bundle length l_{bundle} and bundle thickness w_{bundle} are defined differently based on FAM arrangement.

For laterally arranged FAMs,

$$l_{bundle} = 2 \cdot r(\varepsilon_f) \cdot sin\left(\beta(\varepsilon_f)\right) + l(\varepsilon_f) \cdot cos(\beta(\varepsilon_f)) \tag{7}$$

$$t_{bundle} = \left(\frac{n}{2} - 1\right)\Delta x + 2 \cdot r(\varepsilon_f) \cdot cos\left(\beta(\varepsilon_f)\right) + l(\varepsilon_f) \cdot sin\left(\beta(\varepsilon_f)\right)$$

where $\Delta x = \max\left(\frac{2 \cdot r(\varepsilon_f)}{sin(\beta(\varepsilon_f))}\right)$

$$x_1(\varepsilon_f) = x_c - (j-1)\cdot\Delta x - r(\varepsilon_f)\cdot\cos\left(\beta(\varepsilon_f)\right) \quad (8)$$

$$x_2(\varepsilon_f) = x_c - (j-1)\cdot\Delta x + r(\varepsilon_f)\cdot\cos\left(\beta(\varepsilon_f)\right)$$

$$x_3(\varepsilon_f) = x_2(\varepsilon_f) + l(\varepsilon_f)\cdot\sin\left(\beta(\varepsilon_f)\right)$$

$$x_4(\varepsilon_f) = x_1(\varepsilon_f) + l(\varepsilon_f)\cdot\sin\left(\beta(\varepsilon_f)\right)$$

$$y_1(\varepsilon_f) = y_c - r(\varepsilon_f)\cdot sin(\beta(\varepsilon_f))$$

$$y_2(\varepsilon_f) = y_c + r(\varepsilon_f)\cdot sin\left(\beta(\varepsilon_f)\right)$$

$$y_3(\varepsilon_f) = y_2(\varepsilon_f) - l(\varepsilon_f)\cdot cos(\beta(\varepsilon_f))$$

$$y_4(\varepsilon_f) = y_1(\varepsilon_f) - l(\varepsilon_f)\cdot cos(\beta(\varepsilon_f))$$

$j = 1,2,\dots,\frac{n}{2}$

For centrally arranged FAMs,

$$l_{bundle} = \left(\frac{n}{2} - 1\right)\Delta y + 2\cdot r(\varepsilon_f)\cdot sin\left(\beta(\varepsilon_f)\right) + l(\varepsilon_f)\cdot cos(\beta(\varepsilon_f)) \quad (9)$$

$$t_{bundle} = 2\cdot r(\varepsilon_f)\cdot cos\left(\beta(\varepsilon_f)\right) + l(\varepsilon_f)\cdot sin(\beta(\varepsilon_f))$$

where $\Delta y = \max\left(\frac{2\cdot r(\varepsilon_f)}{\sin(\beta(\varepsilon_f))}\right)$

$$x_1(\varepsilon_f) = x_c - r(\varepsilon_f)\cdot\cos\left(\beta(\varepsilon_f)\right) \quad (10)$$

$$x_2(\varepsilon_f) = x_c + r(\varepsilon_f)\cdot\cos\left(\beta(\varepsilon_f)\right)$$

$$x_3(\varepsilon_f) = x_2(\varepsilon_f) + l(\varepsilon_f)\cdot\sin\left(\beta(\varepsilon_f)\right)$$

$$x_4(\varepsilon_f) = x_1(\varepsilon_f) + l(\varepsilon_f)\cdot\sin\left(\beta(\varepsilon_f)\right)$$

$$y_1(\varepsilon_f) = y_c - (j-1)\cdot\Delta y - r(\varepsilon_f)\cdot\sin\left(\beta(\varepsilon_f)\right)$$

$$y_2(\varepsilon_f) = y_c - (j-1)\cdot\Delta y + r(\varepsilon_f)\cdot sin\left(\beta(\varepsilon_f)\right)$$

$$y_3(\varepsilon_f) = y_2(\varepsilon_f) - l(\varepsilon_f)\cdot cos(\beta(\varepsilon_f))$$

$$y_4(\varepsilon_f) = y_1(\varepsilon_f) - l(\varepsilon_f)\cdot cos(\beta(\varepsilon_f))$$

$$j = 1,2,\dots,\frac{n}{2}$$

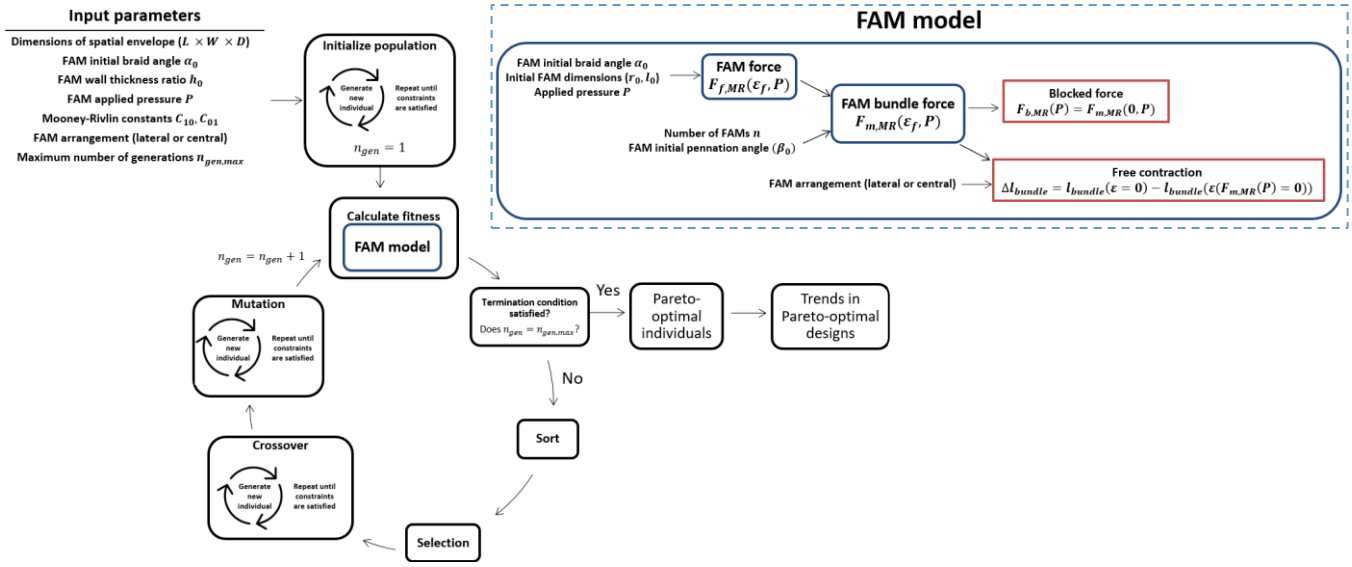

Figure 3.5. Schematic of optimization framework with FAM model.

Given the input parameters of the spatial envelope dimensions, geometric parameters of the braided sleeve, properties of the inner bladder, and choice of FAM arrangement (lateral or central), a set of random FAM bundle designs or individuals are generated to create an initial population. If the individual does not satisfy constraints, a new FAM bundle design is generated until the constraints are satisfied. The FAM model is used to evaluate the objectives or fitness of each individual. If the termination criteria are not met, this MOGA uses a non-dominated sorting genetic algorithm (NSGA) to rank individuals or FAM bundle designs in the population based on the

objectives. The highest-ranking individuals are selected as elite and parents. Offspring are generated by randomly selecting genes from each parent in crossover. The crossover scheme randomly selects the initial pennation angle from one of the parents and selects either the initial radius or the intial length from one of the parents. These two selected design variables from the parent designs are used to solve for the unknown FAM dimension and checked for feasibility with the specified bounding envelope. This process is repeated until constraints are satisfied. Mutation is applied to only a select number of individuals in the population, where only one variable is mutated in the design. The design variable randomly selects initial radius, initial length, or intial pennation angle and checked for feasibility. This step is repeated until mutated individuals satisfy constriants. The dimensions of the FAM as well as its pennation angle are needed to determine an appropriate number of FAMs that will satisfy the boundary conditions. Thus, n is the largest number allowable when generating the FAM bundle design with the new design parameters. Individuals in the new population are evaluated for their fitness. If the termination conditions are met, Pareto-optimal individuals in the population are extracted to identify trends in the optimal designs. At each generation of the optimization algorithm, the top 30% of the population is selected as elite individuals, top 50% of the population are selected to be parents, and top 30% are mutated.

3.3 Results

The Pareto frontier of the optimal FAM bundle designs are generated for a specified spatial envelope. (Pareto frontier axes are FAM bundle blocked force and FAM bundle free contraction.) This study assumes an initial braid angle $\alpha_0 = 30°$, FAM wall thickness ratio $h_0 = \frac{t_0}{r_0} = \frac{1}{6}$, and an applied pressure $P =$ 344.7 Pa (50 psi). A stress-strain test was performed on the selected bladder material and the measured

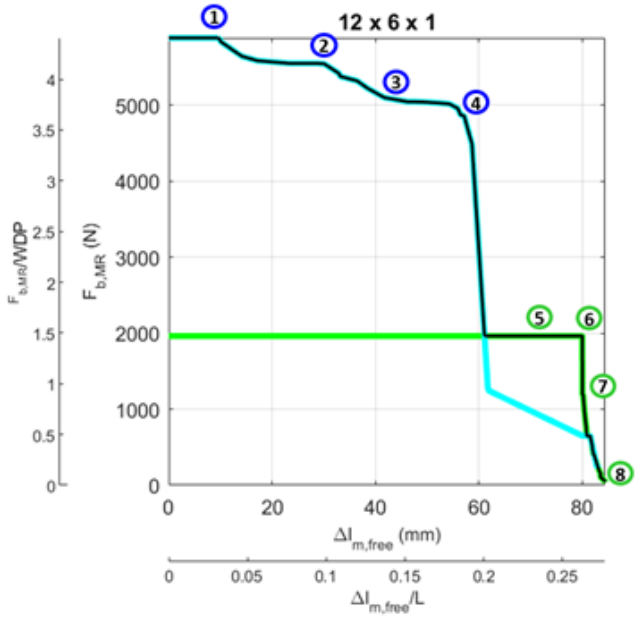

Figure 3.6. Pareto frontier for maximizing FAM bundle blocked force and free contraction within a 12 × 6 × 1 rectangular spatial envelope in black. The results correspond to $P =$ 344.7 kPa.Cyan curve shows region of Pareto frontier where the optimal FAM bundle designs have laterally arranged FAMs while the green portion corresponds to centrally arranged FAMs. Number labels correspond to different FAM bundle designs along the Pareto frontier. The designs are shown in

Mooney-Rivlin constants are $C_{10} = 55.4$ kPa and $C_{01} = 260.5$ kPa.

For a specified rectangular spatial envelope 30.48 cm (12 inches) in length , 15.24 cm (6 inches) in width, and 2.54 cm (1 inch) in depth, Figure 3.6 shows the resulting Pareto frontier for maximizing both force and stroke of the FAM bundle after 5000 generations. The light green curve is associated with the Pareto frontier of FAM bundle designs with FAMs that are laterally arranged, while the cyan curve corresponds to designs with FAMs that are centrally arranged. An inspection of both curves allows us to estimate the overall Pareto frontier of all FAM bundle designs, as shown in the black curve.

This Pareto frontier result maps the force and stroke tradeoff to different FAM bundle designs. Notice the intersection of the two curves indicates a transition in FAM arrangement. To the left of this intersection, FAM bundle

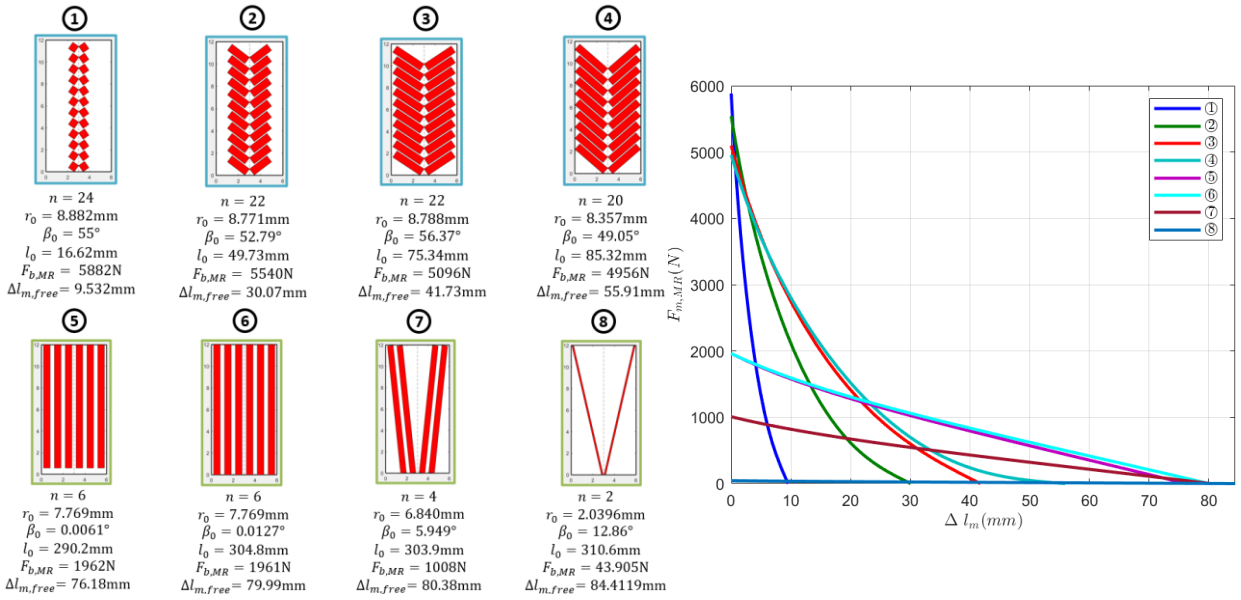

Figure 3.7. Illustrations of each FAM bundle design numbered along the Pareto Frontier in Figure 3.6 with their corresponding FAM bundle parameters as well as model predicted blocked force and free contraction listed below. The plot shows the model predicted bundle force-contraction behaviour for each FAM bundle design illustrated. The results correspond to $P = 344.7$ kPa.

designs with centrally arranged FAMs are more desirable while to the right, the preferred arrangement of the FAMs is lateral. Under this spatial envelope aspect ratio $(\frac{L}{W})$, a centrally arranged FAM bundle design is desireable for large force applications while a laterally arranged FAM bundle design is desireable for large stroke applications.

To observe the trade-offs between force and stroke, several FAM bundle designs numbered along the Pareto frontier are shown in Figure 3.7. Each numbered label represents a different FAM bundle design as illustrated, and their corresponding bundle force-strain relationship is plotted. The progression of FAM bundle designs along the Pareto frontier shows a large number of short FAMs arranged centrally at a large pennation angle produces the most bundle force but least amount of bundle stroke. In order to achieve more bundle stroke, the optimal number of FAMs in the bundle decreases along with a change in FAM diameter to allow for longer length FAMs to be

arranged at smaller pennation angles. However, this design change leads to a drop in bundle force. Thus, as more bundle stroke is desired, the optimal FAM arrangement switches from central to lateral. The force-contraction curves in Figure 7 quantifies and illustrates these changes by directly analyzing the capabilities of these Pareto-optimal FAM bundle designs at the same applied pressure.

Although these results show a pennate topology is optimal for most of this operating space, there are still some force-stroke conditions, there are still some force-stroke conditions where the parallel topology is more desirable. By nondimensionalizing the Pareto frontier, the shape and trends observed can be applied to any rectangular spatial envelope of the same aspect ratio. The FAM bundle blocked force was compared to the force that would be produced by the same pressure applied to equivalent total cross-sectional area ($W \cdot D$) of the full spatial envelope. The FAM bundle free contraction was compared to the length of the spatial envelope, which suggests the extent of contraction strain possible. In the $12 \times 6 \times 1$ aspect ratio case, it shows the majority of the optimal-FAM bundle designs along the Pareto frontier achieve a larger force in comparison to the pressure force applied to equivalent total cross-sectional area of the spatial envelope where $\frac{F_{b,MR}}{WDP}$>1.

3.3.1 Experimental validation

To validate the observations and trends seen from these FAM bundle optimization results, several FAM bundle designs were selected and fabricated for a $12 \times 6 \times 1$ rectangular aspect ratio envelope. For ease of fabrication, the initial FAM radius was kept the same and the overall envelope dimensions were scaled to maintain the $12 \times 6 \times 1$ aspect ratio for each design. The selected bundle designs are described in Table 1. These designs correspond to the cases illustrated in Figure 6.

C_{10} = 55.4 kPa, C_{01}= 260.5 kPa					
Design	Bounding Envelope $L \times W \times D$ [mm]	n	r_0[mm]	β_0[°]	l_0[mm]
③	327.7 × 163.8 × 27.31	20	9.522	53.62	87.42
⑤	373.4 × 186.7 × 31.12	6	9.522	0.0049	330.2
⑥	373.4 × 186.7 × 31.12	6	9.522	0.0049	355.6
⑦	426.7 × 213.4 × 35.56	4	9.522	5.997	425.6

Table 3.1. Mooney-Rivlin constants (C_{10}, C_{01}) and parameters of FAM bundle designs along the Pareto frontier for $12 \times 6 \times 1$ spatial aspect ratio.

In fabricating the FAMs for these experiments, several fittings and connectors are used at the end of the bladder and mesh structure to ensure a fluid tight seal, a way to supply pressurized fluid, and ball-joint for smooth rotation. These additional components have no impact on the measured blocked force of the FAM as they do not assist in generating force and are considered inactive. However, they contribute to the overall length of the FAM. This inactive length $l_{inactive}$ limits the extent of rotation and influences the free contraction as seen in the expression for evaluating the pennation angle at free contraction:

$$\beta_{free,in} = \sin^{-1}\left(\frac{\sin(\beta_0)(l_0 + l_{inactive})}{l_{free} + l_{inactive}}\right) \tag{11}$$

The bundle free contraction with inactive length can be expressed as:

$$\Delta l_{free,in} = (l_0 + l_{inactive})\cos(\beta_0) - \left(l_{free} + l_{inactive}\right)\cos\left(\beta_{free,in}\right) \tag{12}$$

In the case of parallel FAM bundles, the FAMs are aligned with the direction of motion and not expected to rotate so the model predicted free contraction $\Delta l_{free,in}$ is unaffected by the inactive length. Also, as seen in equation 12, the number of FAMs in the bundle has no effect on free contraction. On the other hand, the blocked force scales with the number of FAMs in the bundle

as seen in equation 3. Thus, for testing purposes, only a pair of FAMs were built for each of the pennate FAM bundle designs (Designs 3 and 7, Figure 3.8) and a single FAM was built for each of the parallel bundle designs (Designs 5 and 6). The measured blocked force was then scaled by the number of FAMs in the bundle design.

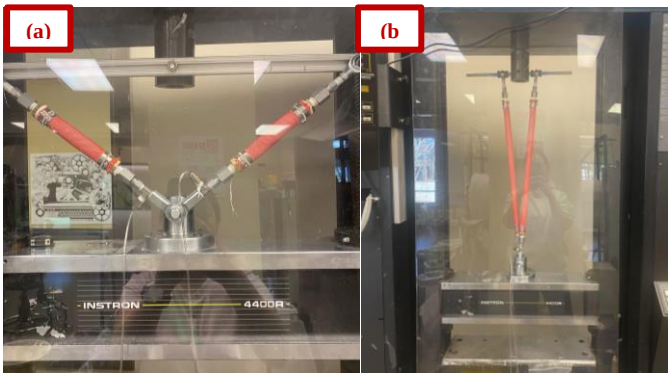

Figure 3.8. Instron Model #4400R mounted with (a) pair of FAMs in Design 3 (b) pair of FAMs in Design 7.

The experimental measurements are tabulated in Table 2 with the blocked force scaled according to the number of FAMs in the bundle design. The measured inactive length for the FAMs used in these experiments was $l_{inactive} = 266.7$ mm (10.5 in). Figure 3.8 shows the nondimensionalized blocked force and free contraction for the selected FAM bundle designs corresponding to the spatial envelope dimensions shown in Table 1. The experimental blocked force and free contraction for each design align relatively well with the expected model predictions for a $12 \times 6 \times 1$ aspect ratio envelope. The results illustrate the aspect ratio for this spatial envelope allows for a large number of FAMs arranged centrally by orienting them at a large pennation angle to achieve greater bundle force. However, this limits the length of FAMs and bundle free contraction as seen in the FAM bundle in design 3. In comparison, this spatial envelope aspect ratio allows for longer length FAMs arranged laterally to produce more bundle free contraction as seen in the parallel FAM bundles in design 5 and 6 as well as the pennate FAM bundle in design

7. This lateral arrangement reduces the number of FAMs in the bundle and consequently produces less bundle force. Although the FAM bundle in design 7 only has two pairs of FAMs, the bundle contraction is greater than that of a parallel bundle designs due to the FAM rotation behavior with a small pennation angle. Section 4 extensively discusses the spatial envelope aspect ratio impact on optimal FAM bundle design.

Experiments		
Design	$F_{b,exp}$[N] ($\frac{F_{b,exp}}{WDP}$)	$\Delta l_{exp,free}[mm]$ ($\frac{\Delta l_{exp,free}}{L}$)
③	4969 (3.2221)	32.56 (0.0994)
⑤	2722 (1.359)	87.19 (0.2335)
⑥	2958.5 (1.4774)	92.96 (0.249)
⑦	1777 (0.6794)	111.9886 (0.2624)

Table 3.2. Experimentally measured blocked force and free contraction for selected FAM bundle designs.

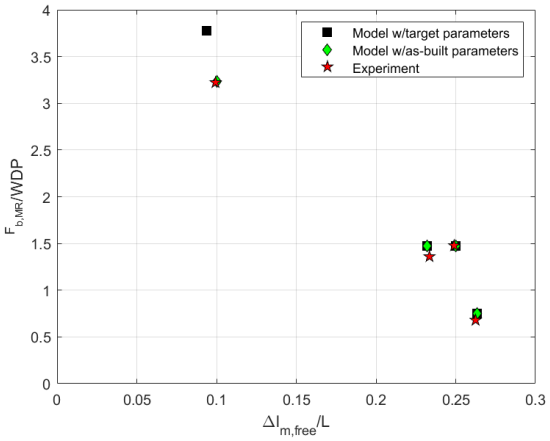

Figure 3.9 Experimental blocked force and free contraction compared to model predictions.

Although care was taken in the fabrication process to target the design parameters listed in Table 3.1, the as-built parameters can deviate slightly and result in some variation observed between the experimental measurements and model predictions with the target parameters. The most noticeable difference is observed in design 3 where the as-built initial braid angle was measured to be 32°

instead of the target $30°$ and the initial pennation angle was $52°$ instead of the target $53.62°$. This slight variation in the α_0 and β_0 results in approximately 80N drop in blocked force and an additional 1mm in bundle free contraction. This illustrates the blocked force and free contraction sensitivity to α_0 and β_0. Applying the model with the as-built parameter values yields good agreement with the experimental force and free contraction measurements, however, demonstrating the model accuracy. It should also be noted that the FAM model presented in this study is more applicable for slender FAMs. It is observed that the tip ends of the FAM can take on a conical shape upon pressurization and change the force-strain behavior. These tip effects become negligible for large slenderness ratio FAMs, where an ideal cylindrical shape can be assumed. However, the conical ends becomes more evident with small slenderness ratio FAMs, where the tip effects will become significant [15]. For comparison, FAMs in the design 3 bundle are 19.05 mm ($\frac{3}{4}$in) in diameter but only 88.9 mm $(3.5$ in$)$ long. While studies attempt to capture the tip behavior, a precise model is difficult to express and relate to FAM dimensions as it depends on the density of the pantograph network and complicates the friction behavior between braid strands in contact. Furthermore, modeling the elastic forces of the inner bladder become a challenge with the shape change at the tip. Nonetheless, the blocked force and free contraction measurements obtained in this study were within 10% of the model-predicted values when the as-built FAM geometry parameters are used.

3.3.2 Implications of spatial envelope on optimal FAM bundle designs

To further investigate the significance of the spatial envelope, we performed this optimization problem for different spatial envelopes. In this study, we altered the geometric constraints by changing the aspect ratio of the rectangular spatial envelope while keeping the volume the same. The estimated Pareto frontier curves for these different aspect ratio spatial envelopes are shown in

Figure 10. Figure 10(a) shows the resulting Pareto frontier for maximizing both force and stroke of the FAM bundle for a rectangular spatial envelope 21.54 cm ($\sqrt{72} \approx 8.48$ in) in length and width, and 2.54cm(1 in) in depth. Figure 3.10(b) shows the resulting Pareto frontier for maximizing both blocked force and stroke of the FAM bundle for a rectangular spatial envelope that is 15.24 cm (6 in) long, 30.48 cm (12 in) wide, and 2.54 cm(1 in) in depth.

The results show the Pareto frontier varies drastically between different spatial envelope aspect ratios. The shapes of these Pareto frontiers indicate the presence of different trade-offs between force and stroke. The magnitude limits of blocked force decreases as the length dimension of the spatial envelope becomes smaller. However, increasing the width dimension of the spatial envelope allows for larger FAM bundle free contractions.

The $\sqrt{72} \times \sqrt{72} \times 1$ aspect ratio shows optimal FAM bundle designs should always have centrally arranged FAMs. While both laterally and centrally arranged FAM bundle designs were considered in this aspect ratio, the Pareto-optimal configurations are all centrally arranged bundles. This is seen in the green curve in Figure 10(a), showing all laterally arranged FAM bundle designs fall below the force and stroke capacity of all centrally arranged FAM bundle designs along the Pareto frontier. While for the $6 \times 12 \times 1$ aspect ratio, laterally arranged FAMs are more desireable for large force applications while a centrally arranged FAM bundle design is desireable for large stroke applications. Furthermore, a number of optimal-FAM bundle designs along the Pareto frontier can achieve a notably large contraction strain $\frac{\Delta l_{m,free}}{L} > 0.5$. This illustrates the functional capacity of FAM bundle designs can be related to the spatial envelope.

3.4 Discussion

In order to evaluate how the FAM bundle designs along the Pareto fontier change with respect to the spatial envelope and

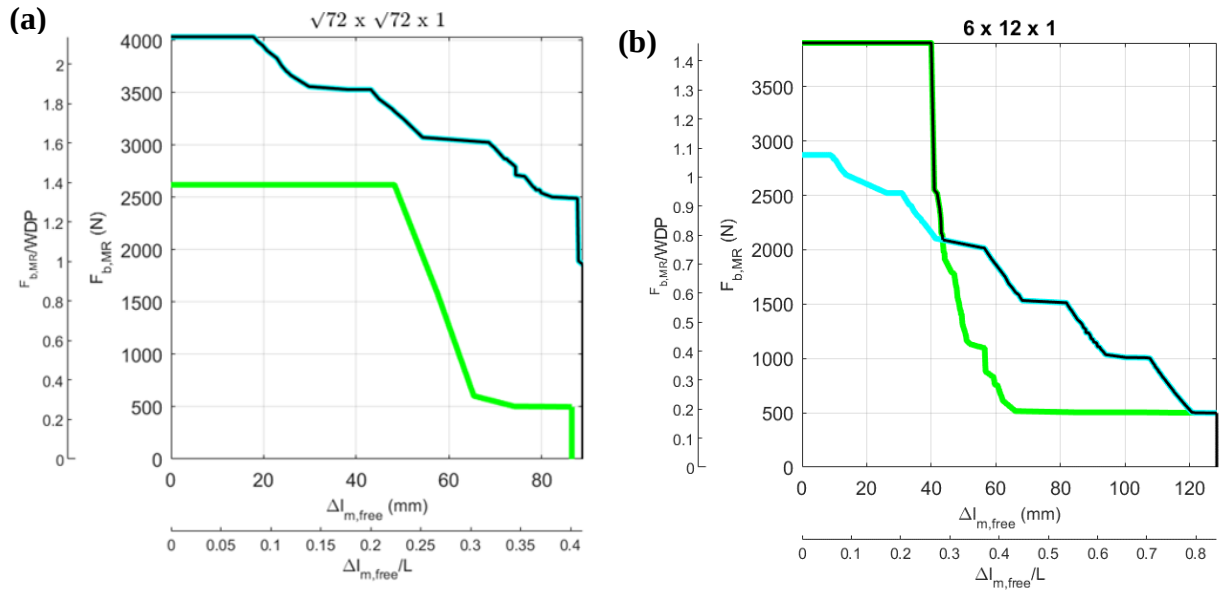

Figure 3.10. Pareto frontier for maximizing FAM bundle blocked force and free contraction within a (a) $\sqrt{72} \times \sqrt{72} \times 1$ rectangular spatial envelope in black (b) $6 \times 12 \times 1$ rectangular spatial envelope in black. The results correspond to $P =$ 344.7 kPa.

see compromises made between force and stroke, a closer inspection of individual design parameters from the optimal FAM bundle designs along the Pareto frontier is needed. In Figures 11-13, each colored y-axis corresponds to a different design parameter for each FAM bundle along the Pareto frontier for the specified aspect ratio. The x-axes shows the corresponding bundle blocked force or free contraction. The blue axes and circle markers correspond to the initial pennation angle, the red axes and square markers are for the initial FAM length, and the green axes and triangle marker is for the number of FAMs in the bundle design. The dotted line identifies a free contraction or blocked force boundary for what type of FAM arrangement is more desireable.

For operating conditions where large force and small contraction are needed, the FAM bundle designs along the Pareto frontier of the $12 \times 6 \times 1$ aspect ratio envelope (Figure 3.11) indicates centrally arranged FAMs with a larger pennation angle are more desireable. The reason is with a large $\frac{L}{W}$ ratio, a large β_0 limits individual FAM length l_0 but allow a greater number of FAMs n in the bundle and results in greater overall bundle force. In this region of the operating space, the β_0 of optimal FAM bundle designs decreases to increase individual FAM length l_0 to achieve more bundle contraction. Although a smaller β_0 contributes to a larger component of axial

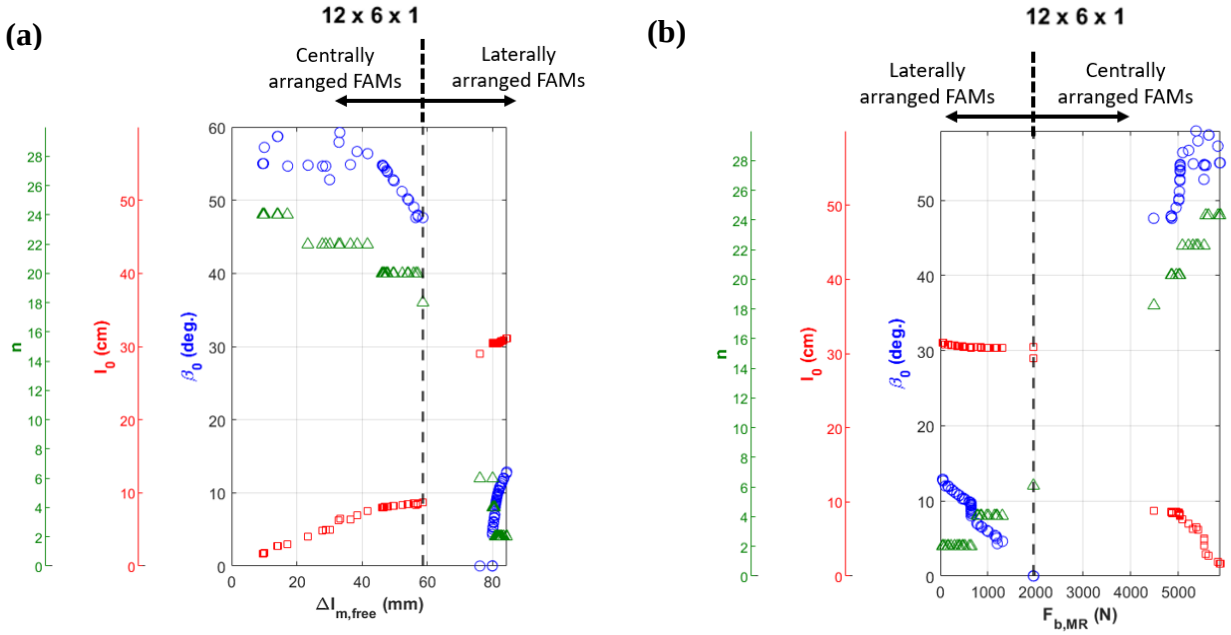

Figure 3.11. Design parameters of FAM bundle designs along Pareto frontier with respect to (a) free contraction and (b) blocked force for $12 \times 6 \times 1$ spatial aspect ratio.

contraction force, n decreases in this central arrangement as a byproduct of the large $\frac{L}{W}$ ratio and results in an overall smaller $F_{b,MR}$. Thus, a distinct change from centrally arranged pennate FAM arrangement to parallel FAM arrangement appears in the operating space.

For operating conditions where small force and large contraction are needed, the FAM bundle designs along the Pareto frontier of the $12 \times 6 \times 1$ aspect ratio envelope indicates laterally arranged FAMs with a small but non-zero pennation angle are more desireable. The lateral arrangement is the reason why we can take advantage of this large $\frac{L}{W}$ ratio to have large individual FAM lengths l_0 for a great amount of $\Delta l_{m,free}$. However, small β_0 in this large $\frac{L}{W}$ ratio limits the number of FAMs n that can be arranged laterally in the bundle and reduces the amount of $F_{b,MR}$. This is evident in the parallel FAM bundle designs. Although a small but non-zero pennation angle does not have a notable effect on individual FAM lengths l_0 in this operating region, the samll but non- zero pennation angle can take advantage of the FAM rotation behavior to allow greater bundle

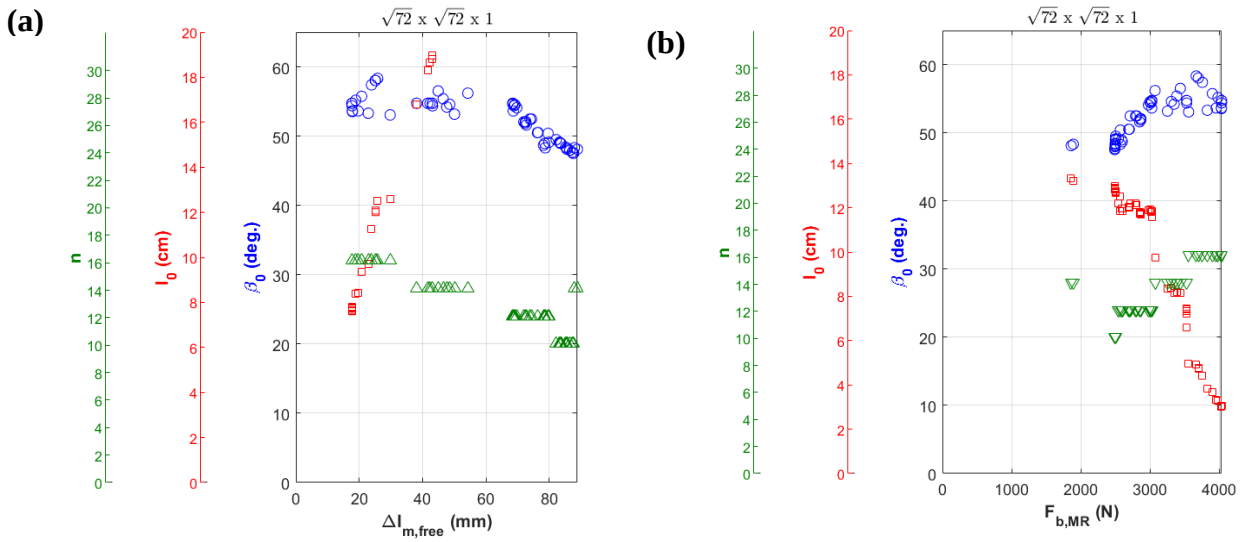

Figure 3.12. Design parameters of FAM bundle designs along Pareto frontier with respect to (a) free contraction and (b) blocked force for $\sqrt{72} \times \sqrt{72} \times 1$ spatial aspect ratio.

contraction compared to bundles with $\beta_0 = 0°$ (parallel) configuration.

In the case of the $\sqrt{72} \times \sqrt{72} \times 1$ aspect ratio, the FAM bundle designs along the Pareto frontier are all centrally arranged FAMs. As seen in Figure 3.12, the FAM bundle designs along the Pareto

frontier indicates a larger pennation angle is more desireable for large force and small contraction operating conditions as described previously. As higher contractions are desired, the β_0 of optimal FAM bundle designs slightly decreases to increase individual FAM length l_0. In the small force and large contraction region, an interesting trend is observed with this square planar enevelope where there is little to no variation in β_0 but an increase in n produces greater bundle contraction. This is a result of having a smaller r_0 enabling slightly longer l_0. One might expect that a larger n should generate a greater amount of force since it is an even integer.

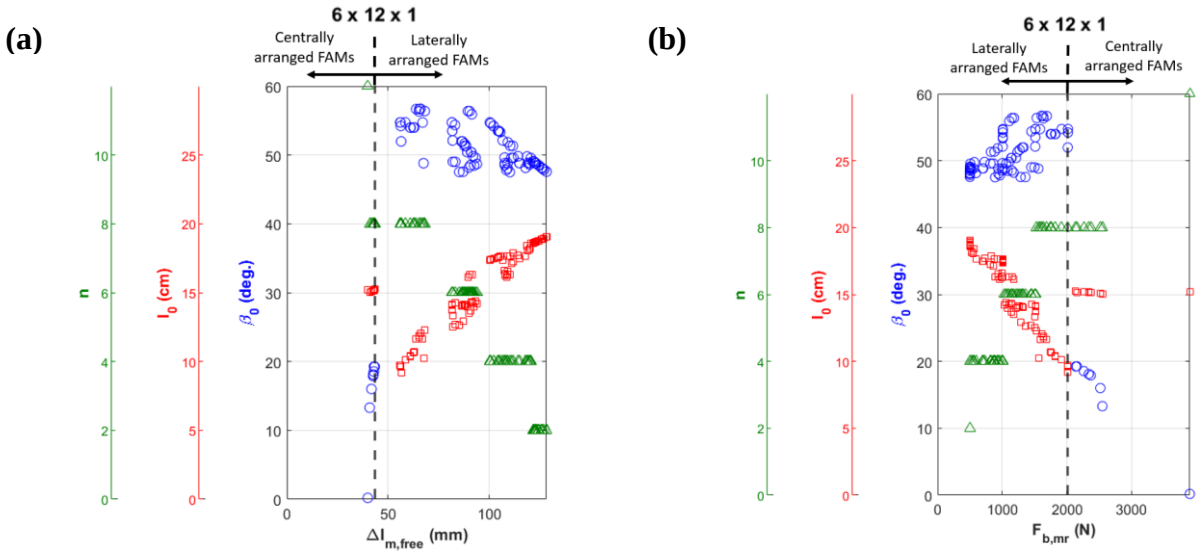

Figure 3.13. Design parameters of FAM bundle designs along Pareto frontier with respect to (a) free contraction and (b) blocked force for $6 \times 12 \times 1$ spatial aspect ratio.

However, based on the FAM model, the r_0 term is squared so despite having a larger n value, the smaller r_0 dominates and produces a smaller bundle force.

In the case of the $6 \times 12 \times 1$ aspect ratio (Figure 3.13), the individual FAM bundle design parameters for the designs along the Pareto frontier drastically differ from trends seen before. For operating conditions where large force and small contraction are needed, the FAM bundle designs

along the Pareto frontier indicates laterally arranged FAMs with a small pennation angle are more attractive. The lateral arrangement can be leveraged with this small $\frac{L}{W}$ ratio to have a large number of FAMs n in the bundle and thus increasing $F_{b,MR}$.

Although not much variation is seen in l_0 within this operating region, increasing the β_0 to a small but non-zero value in this lateral arrangement forces the number of FAMs n in the bundle to decrease. This results in a significant decrease in $F_{b,mr}$, but the FAM can take advantage of both axial contraction and rotation for more $\Delta l_{m,free}$. Notice that as more bundle contraction is needed, the designs along the Pareto frontier indicates centrally arranged FAMs with a large pennation angle are preferable. The small $\frac{L}{W}$ ratio is the reason why the number of FAMs n in the bundle that can be arranged centrally is limited and consequently reduces $F_{b,MR}$ as compared to laterally arranged FAMs. A large β_0 leads to a smaller l_0 but the rotation behavior increases and results in more bundle contraction. As the β_0 in this central arrangement decreases in this operating region, the designs approach a single pair of FAMs. Although this reduces $F_{b,MR}$, greater l_0 is allowed and a combined effort of axial contraction of a longer l_0 and rotation enable more $\Delta l_{m,free}$. Thus, it is evident the spatial bounds play an important role in soft actuator topology design and in response the architectural tradeoffs will likely change.

3.5 Conclusion

This paper presents a design optimization method for spatially constrained fluidic artificial muscle bundles. A custom multi-objective genetic algorithm based framework is used to quantify the architectural tradeoff between force and stroke with respect to the specified spatial envelope. This multi-objective optimization problem assumes homogeneous FAMs in the bundle and uniform spatial bounds. The FAMs in the bundle follow a pinned boundary condition, where the

FAMs in the bundle are spaced to account for minimum clearance for the FAMs to radially expand, axially contract, and rotate without interfering the behavior of neighboring FAMs. The nonlinear FAM force-contraction model used in this study accounts for the elasticity of the bladder by including experimentally measured Mooney-Rivlin hyperelastic materal constants. The generated Pareto frontier not only outlines the bundle force and stroke limit for a given pressure in the design space but maps the force and stroke tradeoff to different optimal FAM bundle designs. A close inspection of individual design parameters from the optimal FAM bundle designs along the Pareto frontier provide explanations for compromises made in the design to achieve greater force or stroke. The analysis also reveals when to consider laterally arranged FAMs and centrally arranged FAMs based on the desired force and stroke of the bundle. This design decision is not one that could have been made before. Several designs along the $12 \times 6 \times 1$ aspect ratio Pareto frontier was fabricated and tested to compare with the model predicted bundle force and contraction. The experimental measurements of blocked force and free contraction aligned well with the model predictions and validated the trends observed. By manipulating the aspect ratio of the spatial envelope while the spatial volume is maintaned, the Pareto frontier generated illustrates how the geometric constraint impacts optimal FAM bundle designs.

The capacity of this optimization method allows for investigation of different spatial envelopes and further exploration of spatial envelope implications on FAM bundle design. In the human arm, the biceps brachii has a fusiform parallel architecture, while the extensor diatorum muscle has a unipennate architecture. Should a FAM actuated robot arm use the same configuration? How does the answer to this question change with the required force, range of motion, or size of the robotic limb? The design optimization framework and analysis presented in this study can be used to answer these questions. If the spatial bounds of the robot arm is defined and its force and

displacement capacity to actuate the elbow and shoulder joint is known, the method presented in this study provides the framework to determine the optimal configuration for the robot arm. This framework is not limited to FAMs, as it can also be applicable for other types of soft actuators subject to geoemtric constraints to properly size, arranged, and orient actuator units based on desired objectives. Future work should explore non-uniform spatial bounds, non-planar bundle arrangements, and consider heterogeneous actuators to improve tracking performance or efficiecny in dynamic applications.

CHAPTER 4: Strain amplified with Helically Braided Fiber Reinforced Sleeve for Energy Harvesting

4.1. Introduction

Soft and stretchable devices such as stretchable electronics, e-skins, and soft robotics have the appeal of being deformable. In many cases, it is desirable to be able to incorporate sensors or energy harvesters into such devices to convert strain into electrical signals (sensors) or electricity (harvesters). Here, we report a concept to increase the amount of strain applied to soft materials (with a cylinder geometry) for a given external strain. While this concept could improve the sensitivity of strain sensors, we focus here on energy harvesting as a demonstrator platform.

Deformable devices capable of converting mechanical motion to electricity are useful for stretchable electronics that capture energy from the human body as well as ocean wave energy harvesters. [70–74] Recently, an energy harvesting method was demonstrated that leverages the electrical double layer (EDL) capacitance found in supercapacitors. The EDL forms at the electrode/electrolyte interface where charges are found to accumulate at the boundary between a conductor and a surrounding ionic solution. By building EDLs using soft materials – namely liquid metals encased in hydrogel – it is possible to form energy harvesters, in which the change in capacitance is varied by deforming, and thus changing the area of the electrode. This is described as shown in equation 1. The capacitance, C, of the EDL is due to charges separated by atomic distances d, where ε_0 is the permittivity of free space and ε_r is the relative permittivity of the dielectric material, ΔA is the change in area of the electrode, and Δq is the change in quantity of charge.

$$\Delta C = \frac{\varepsilon_0 \varepsilon_r \Delta A}{d} = \frac{\Delta q}{V} \quad \textbf{(1)}$$

This approach was initially demonstrated by varying the interfacial area between two rigid electrodes separated by water droplets. [75,76] More recently, this concept was extended to an entirely soft and stretchable energy harvester that utilizes liquid metal as the conductor in the device. [41]The liquid metal is encased in hydrogel, where the interface between the liquid metal and hydrogel forms an EDL capacitor. This soft variable-area energy harvester design can operate under multiple modes of deformation (stretching, twisting, or compression) and exhibits comparable performance in air and in water. While this entirely soft variable-area supercapacitor provides a solution to address many existing implementation problems in practical applications, methods to amplify the generated current response per unit of mechanical deformation have yet been explored.

This study proposes the addition of a helically braided fiber reinforced sleeve that can wrap around the hydrogel to augment its electrical output performance by increasing the deformation for a given strain and the braiding ‘squeezes’ a cylindrical/cable form of the gel. The helically braided fiber reinforced sleeve is a tubular structure composed of multiple fibers crossing over and under each other, similar to a basket weave, but the pattern created visually appears as a twill weave, where a set of fibers in the same direction appear to be oriented at a specified angle while another set of fibers appear to be positioned at the same specified angle but in the opposite direction. This tubular pattern structure allows for even distributed load and commonly found in a variety of applications from hydraulic brake hose lines in cars to everyday garden hoses. [77,78] In most common applications, the fibers are aligned in the direction of the resultant tangential and axial forces experienced by the hose to prevent deformation or rupture such that it can operate under high force, high pressure, and/or temperature-varying conditions.

This paper explores the implications of the helically braided fiber reinforced sleeve design in a cylindrical form of this soft variable-area electrochemical supercapacitor. The kinematic behavior of the electrode under axial stretch is modeled with and without the presence of the braided sleeve to observe the strain amplified EDL area induced capacitance change. Simulations of current responses from the equivalent circuit model of the soft supercapacitor are used to compare the effect of the braided sleeve for different mechanical input axial stretch strain profiles.

This paper first details the electrode shape change behavior under axial stretch and the electrode deformation influenced by the kinematics of the helically braided fiber reinforced sleeve. Next, equivalent circuit model for EDL capacitors and the soft supercapacitor are presented and discussed. Then, the influence of the fiber reinforced braided sleeve is examined through simulated and measured current responses corresponding to different axial stretch inputs. Finally, conclusions are made to highlight the contributions and limitations of this work and suggested directions for future study.

4.2 Results and Discussion

In this study, the soft supercapacitor design comprises of two equally sized liquid metal electrodes (eutectic mixture of gallium and indium, EGaIn [79]) encapsulated inside the same polyacrylamide hydrogel casing as shown in **Figure 4.1**. The polyacrylamide hydrogel contains 1M of sodium chloride as an electrolyte to form an EDL capacitor. The hydrogel takes a cylindrical form while the electrodes assume the shape of a capsule (a cylinder with hemispherical ends) at rest, where electrical equilibrium is established. The soft elastic structure of the hydrogel allows for one encapsulated liquid metal electrode, termed the working electrode, to change shape in response to local axial stretch applied to the hydrogel while the other electrode, termed the reference electrode, remains stationary.

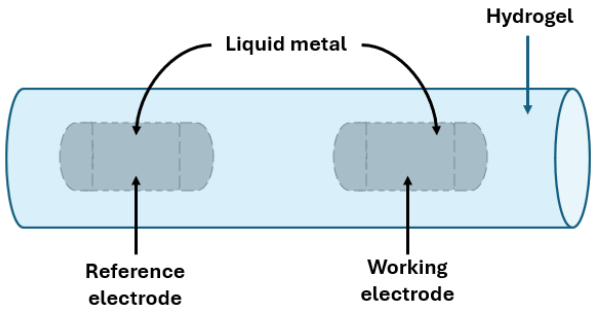

Figure 4.1. Schematic of soft supercapacitor with two liquid metal electrodes encapsulated in hydrogel.

Geometric changes to the hydrogel directly align with the observed deformation of the working electrode, such that the working electrode shape take on prolate hemi-ellipsoid shape ends based on axial stretch $\boldsymbol{\varepsilon} = \frac{\Delta \boldsymbol{l}}{\boldsymbol{l_0}}$ applied to the hydrogel. Details of this geometric model are found section S1 in the Supporting Information. This working electrode shape change increases the interfacial area between the electrode and electrolyte to disrupt the electrical equilibrium at rest and drives charges through the circuit until a new equilibrium state is reached. Returning the stretched working electrode to its initial shape at rest drives charges in the opposing direction through the circuit. Thus, alternating current is produced from mechanical input of cyclic axial stretch.

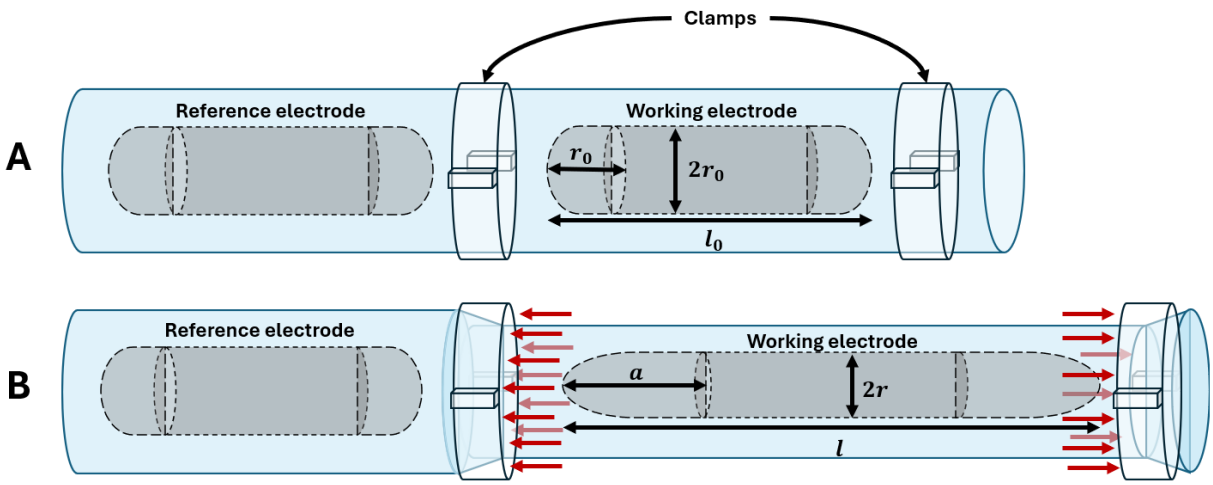

Figure 4.2. Capsule geometry of working electrode transforms to cylinder geometry with hemi-ellipsoid ends due to mechanical stretch. Schematic of soft supercapacitor with two clamps used to isolate the working electrode at rest or unloaded state (A) and stretched state with distributed axial tension applied to the clamps (B).

The fabricated soft supercapacitor used in this study has liquid metal electrode radii of $\boldsymbol{r_0 = 2.5}$ mm and length of $\boldsymbol{l_0 = 1}$ cm at rest. The polyacrylamide hydrogel is approximately 17.5 mm in diameter and 7 cm in length with the electrodes approximately 1.3 cm apart at rest. The unexpanded and fully expanded diameter of the helically braided fiber reinforced sleeve are 12.7 mm and 19.05 mm, respectively.

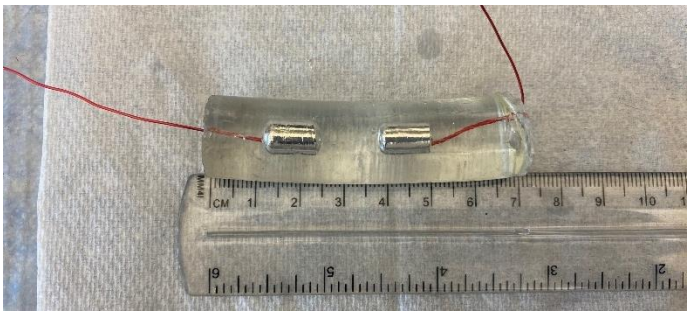

Figure 4.3. Soft supercapacitor with two liquid metal electrodes encapsulated in hydrogel casing.

4.2.1 Effect of Helically Braided Sleeve on EDL Area

The helically braided design of the braided sleeve is illustrated as a network of jointed pantographs where the braid angle $\boldsymbol{\theta}$ denoted in **Figure 4** is the angle of each elementary pantograph. [33]

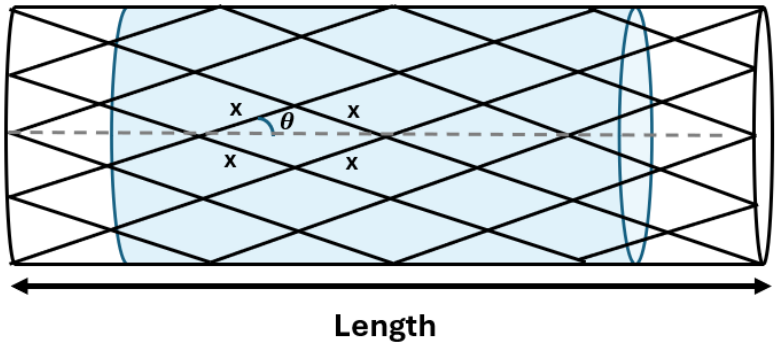

Figure 4.4. Schematic of pantograph network of helically braided sleeve design around cylindrical hydrogel.

This braid angle determines the extent of axial extension or contraction as well as radial expansion or compression. A large starting braid angle corresponds to a greater operating axial strain and radial compression working range as detailed in S2 in the Supporting Information. The radial compression of the liquid-metal-hydrogel composite is linearly related to the axial stretch of the device following Poisson's ratio for incompressible materials based on Equation (S2). The addition of a helically braided fiber reinforced sleeve to the liquid-metal-hydrogel composite alters this radial deformation by driving a change in internal volume. This helically braided design forces the internal volume to decrease and result in greater radial compression. **Figure 4.5**A shows the radial deformation of the soft supercapacitor with the braided sleeve has an exponential relationship to axial strain. Thus, the corresponding change in EDL area illustrated in Figure 4.5B with the presence of the helically braided fiber reinforced sleeve is larger than without the braided sleeve. Table S1 in the Supporting Information and this analysis shows that while a larger starting braid angle design increases the operating axial strain range of the device,

and therefore also increases the maximum radial deformation and change in EDL area, the radial deformation is more sensitive to axial strain with smaller braid angles. This gives designers the opportunity to tune the sensitivity of the device to the expected strain operating range by appropriately choosing the starting braid angle.

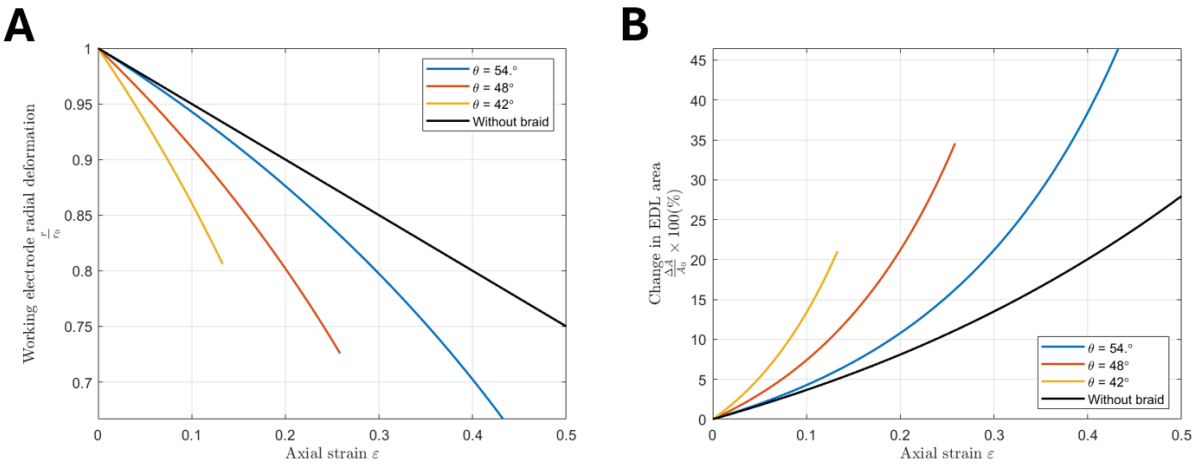

Figure 4.5. Model predicted radial deformation (A) and change in EDL area in percent (B) of the working electrode with respect to axial stretch strain for different starting braid angle θ_0 designs compared to without braid. The maximum operating axial strain range is determined by the starting braid angle as well as manufacturer dimensions of the braided sleeve. Details are found in S2 in the Supporting Information.

4.2.2 Equivalent Electrical Circuit Model for the Soft Supercapacitor

The classical equivalent circuit model commonly used for an EDL capacitor in electrochemical cells consists of the capacitance of the double layer ($\boldsymbol{C_{dl}}$), an equivalent series resistance (ESR) and equivalent parallel resistance (EPR) as shown in **Figure 4.6**. [80–82]

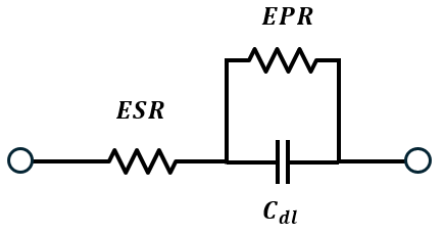

Figure 4.6. Conventional equivalent circuit model for EDL capacitor

The ESR is related to the electrolyte in the cell, and decreasing the distance between the two liquid metal electrodes and increasing the electrolyte concentration in the hydrogel can both decrease this resistance. The EPR is associated with charge-transfer resistance in the faradaic process, where electron transfers across the electrode/electrolyte interface causing an oxidation or reduction reaction to occur. The current resulting from these redox reactions at the working and reference electrode is known as faradaic current. The magnitude of faradaic current is determined by the rate of oxidation or reduction reaction at the electrode surface. However, current not related to any redox reactions may also exist in an electrochemical cell and are referred to as non-faradaic or capacitive current. Non-faradaic process occurs when the electrode potential or electrolyte composition in the cell changes. Non-faradaic current appears when negatively charged particles in the electrolyte solution migrate toward the positively charged electrode while the positively charged particles move away from the positively charged electrode. When the migration behavior is dictated by the electrolyte, the product is the structure of an EDL interface and depends on the surface area of the electrodes and concentration of the electrolyte. Although both faradic and non-faradaic processes can simultaneously occur, the magnitude of non-faradaic current is much smaller.

Cyclic voltammetry is an electrochemical analytical technique used to capture any current response from the electrochemical cell by using a potentiostat to apply a triangular potential waveform. Although this technique is commonly used to characterize reduction and oxidation

processes of molecular species as well as electron transfer-initiated chemical reactions, it is also used to observe capacitive behavior in an electrochemical cell. [83,84]Cyclic voltammograms of electrochemical cells with redox reactions appear duck shaped, where faradaic current from redox reactions appears as peaks. In contrast, the cyclic voltammogram shape for an ideal EDL capacitor is a parallelogram.

The traces in **Figure 4.7** are the voltammograms experimentally measured for the soft supercapacitor presented in this study. The lack of peaks seen in the voltammogram

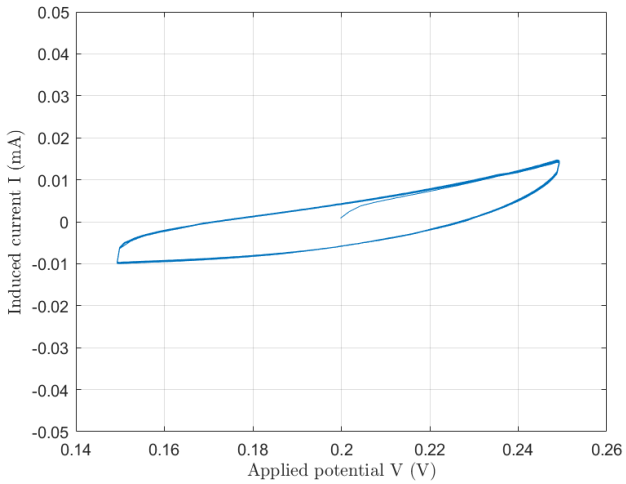

Figure 4.7. Voltammograms of the soft supercapacitor at rest for a 100-mV potential window and a scan rate of 100 $\frac{\mathbf{mV}}{\mathbf{s}}$.

illustrates no charge transfer behavior is present in this potential range and only non-faradaic current is present in this electrochemical cell. Thus, the EPR in the equivalent circuit model for EDL capacitor can be neglected and the behavior of the electrode/electrolyte interface for this system can be represented as a capacitor only. [23,24,28] The classical definition of a capacitor $\boldsymbol{C = \frac{\varepsilon_0 \varepsilon_r A}{d}}$ consists of two parallel conductive plates separated by a dielectric material, where $\boldsymbol{\varepsilon_0}$ is the permittivity of free space and $\boldsymbol{\varepsilon_r}$ is the relative permittivity of the dielectric material, $\boldsymbol{A}$ is the surface

area of the conductive plate, and $\boldsymbol{d}$ is the distance between the parallel plates. In this case, the EDL resembles two charged layers separated by electrolyte molecules from the electrode. Thus, the resulting equivalent electrical circuit model shown in Figure 4.8 represents the electrochemical cell used to evaluate the behavior of the soft supercapacitor with two liquid metal electrodes in this study. Each capacitor element represents the EDL capacitance from the liquid metal electrode and the resistor in series corresponds to the electrolyte resistance $\boldsymbol{R}$. Axial stretch applied to the working electrode (WE) increases the EDL area of that electrode and consequently increases capacitance to move charges on the reference electrode (RE) onto the working electrode. Releasing the stretched WE back to its original unstretched state will decrease the EDL area and capacitance to return charges back to the RE. Alternating current induced by cyclic stretching the WE in the soft supercapacitor can be simulated following Kirchoff's voltage law. (Supporting Information)

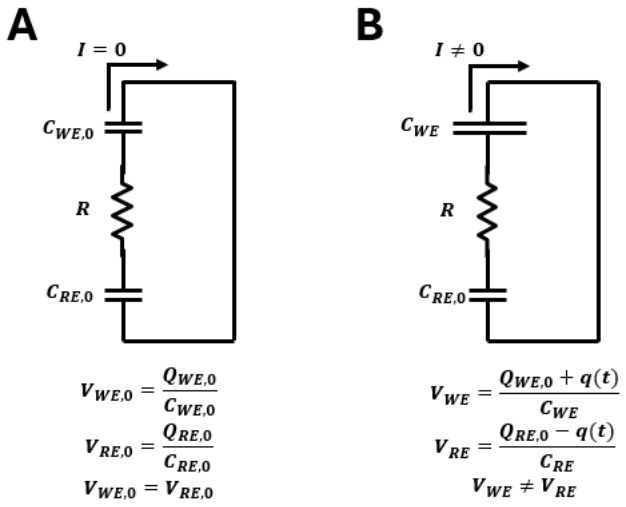

Figure 4.8. Equivalent electrical circuit model for the electrochemical cell in the soft supercapacitor where the capacitor elements represent the EDL capacitance correspond to each liquid metal electrode in the hydrogel and a resistor element representing the

electrolyte resistance in the hydrogel. (A) shows the circuit initially in equilibrium with the device at rest and (B) shows a perturbation due to deformation of the device when the working electrode is stretched.

4.2.3 Simulation Results

The specific capacitance $\mathbf{C_{sp}} = \frac{\int \mathbf{IdV}}{\frac{\mathbf{dV}}{\mathbf{dt}} \times \Delta \mathbf{V} \times \mathbf{A}}$ of the EDL is needed to predict the change in capacitance from the kinematic model of EDL area. The specific capacitance found from the trace in the voltammogram is $\approx \mathbf{34.9}\,\frac{\boldsymbol{\mu F}}{\boldsymbol{cm^2}}$, which is within the range of typical metals in electrolyte ($\mathbf{10}\,\frac{\boldsymbol{\mu F}}{\boldsymbol{cm^2}} \leq \mathbf{C_{sp}} \leq \mathbf{40}\,\frac{\boldsymbol{\mu F}}{\boldsymbol{cm^2}}$). [21]

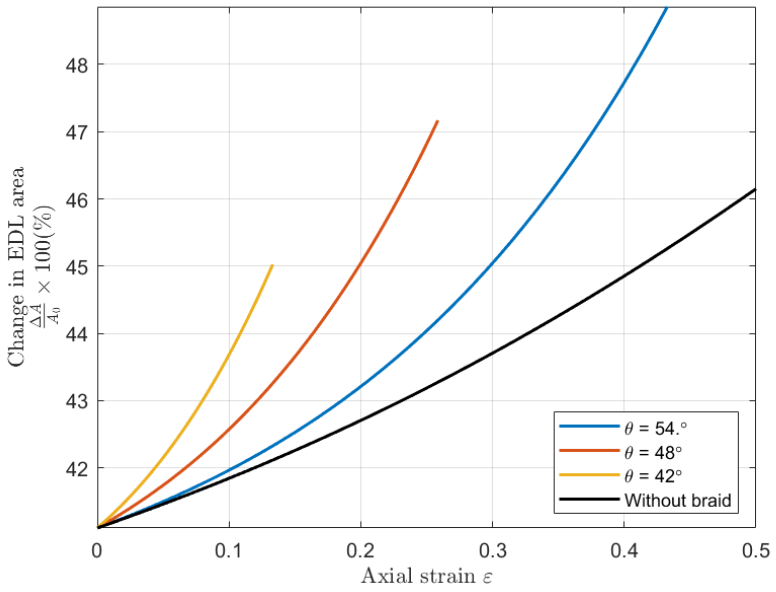

Figure 4.9. Simulated change in total capacitance of soft supercapacitor subject to axial stretch strain

Figure 4.9 shows the model predicted total capacitance $\boldsymbol{C_T} = \frac{\boldsymbol{C_{WE}C_{RE}}}{\boldsymbol{C_{WE}+C_{RE}}}$ is $\approx \mathbf{41.1}\boldsymbol{\mu F}$ at rest aligns with the total capacitance ($\mathbf{41.42}\boldsymbol{\mu F}$, averaged across 15 cycles) calculated from cyclic voltammetry data. The total capacitance measure from cyclic voltammogram using the

change in stored energy approach expressed from the integral of instantaneous power of the soft supercapacitor as discussed in S5 in the Supporting Information. To simulate the induced current response from the equivalent electrical circuit model, an understanding of electrolyte resistance based on Pouillet's law is required. (S4 in the Supporting Information) An existing study found a sufficient method of predicting change in electrical resistivity of a polyacrylamide hydrogel containing sodium chloride. The method illustrates the undeformed resistance of the hydrogel was approximately equivalent to that of water with the same concentration of sodium chloride and the measured molar conductivity matched closely with the reported value for aqueous solutions. This electrolyte resistivity is expressed as $\frac{\boldsymbol{R}}{\boldsymbol{R_0}} = (\mathbf{1} + \boldsymbol{\varepsilon})^{\mathbf{2}}$, where the resistance increases exponentially as the hydrogel is stretched. [73] The 1M sodium chloride concentration (~5% mass percent) used in this study corresponds to electrical resistivity of $\mathbf{14.3\ \Omega cm}$ [85,86] and the electrolyte resistance varies from 7.71 $\mathbf{\Omega}$ at rest to 12.1 $\mathbf{\Omega}$ when stretched to the maximum operating axial strain for $\boldsymbol{\theta_0} = \mathbf{48}°$. We note that although the conductivity of hydrogel materials is notably lower than that of metals due to low water retention from evaporation, this can be improved with high concentrations of electrolyte as shown in previous studies. [76] **Figure 4.10**A shows the prescribed triangle cyclic waveform with a peak 10% axial stretch on the working electrode at 1 Hz. The model prediction of working electrode capacitance (Figure 4.10B) and induced current response (Figure 4.10C) corresponding to the prescribed mechanical input are illustrated, where the soft supercapacitor with the braided sleeve is shown in red and without the braided sleeve is shown in black.

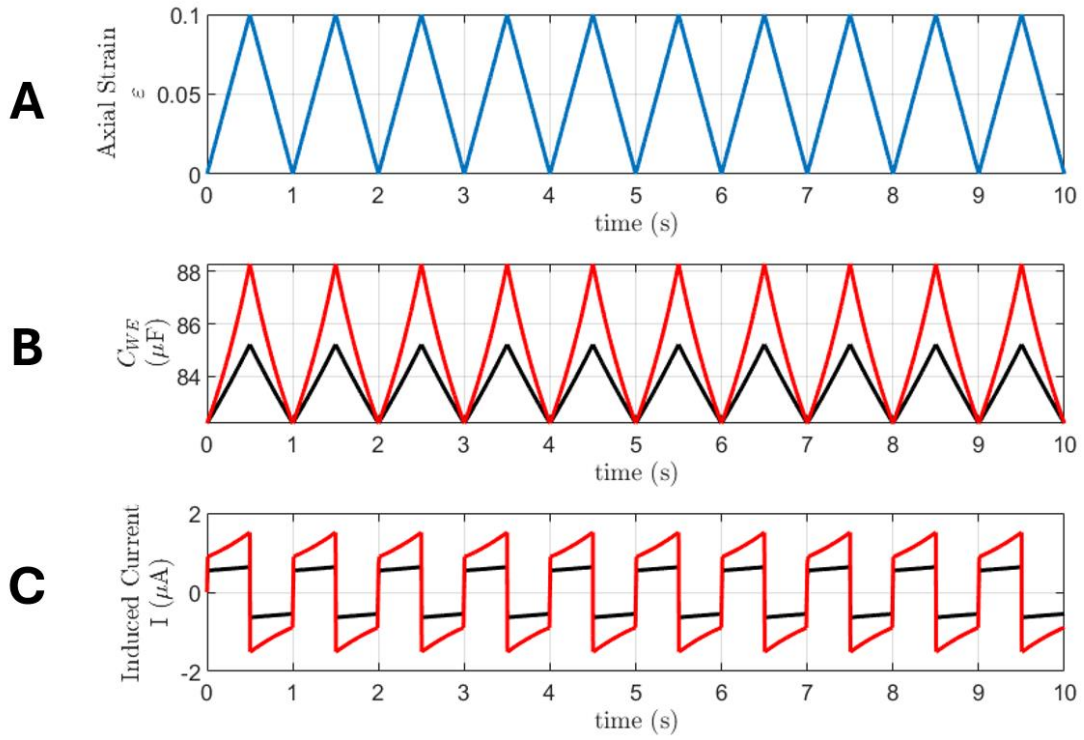

Figure 4.10. The prescribed triangle waveform for mechanical input shown in (A) is for a 10% peak axial stretch at 1 Hz on the working electrode. The model predicted change in working electrode capacitance (B) and simulated induced current (C) with (in red) and without (in black) the helically braided sleeve is shown for the prescribed mechanical input (A).

The open circuit voltage (OCV) of the device at rest measured from the cyclic voltammetry data is approximately 0.2V and is used to estimate the initial quantity of charges on the electrodes in the soft supercapacitor. The current peaks observed indicate movement of charges in response to the imposed axial stretch. The simulation results show larger peaks for the soft supercapacitor with the braided sleeve (in red) as compared without the braided sleeve (in black). This demonstrates that braided sleeve is serving to amplify the radial compression of the working electrode to increase the EDL area, subsequently increasing total capacitance and allowing for greater movement of charges within the device. Simulation results of induced

current responses to imposed peak axial strain amplitudes of 10%, 20%, and 30% at 1 Hz are shown in **Figure 4.11**, where the growth of peak current values with the fiber reinforced braided sleeve is notably greater as expected with a linear expression for radial compression without the braided sleeve.

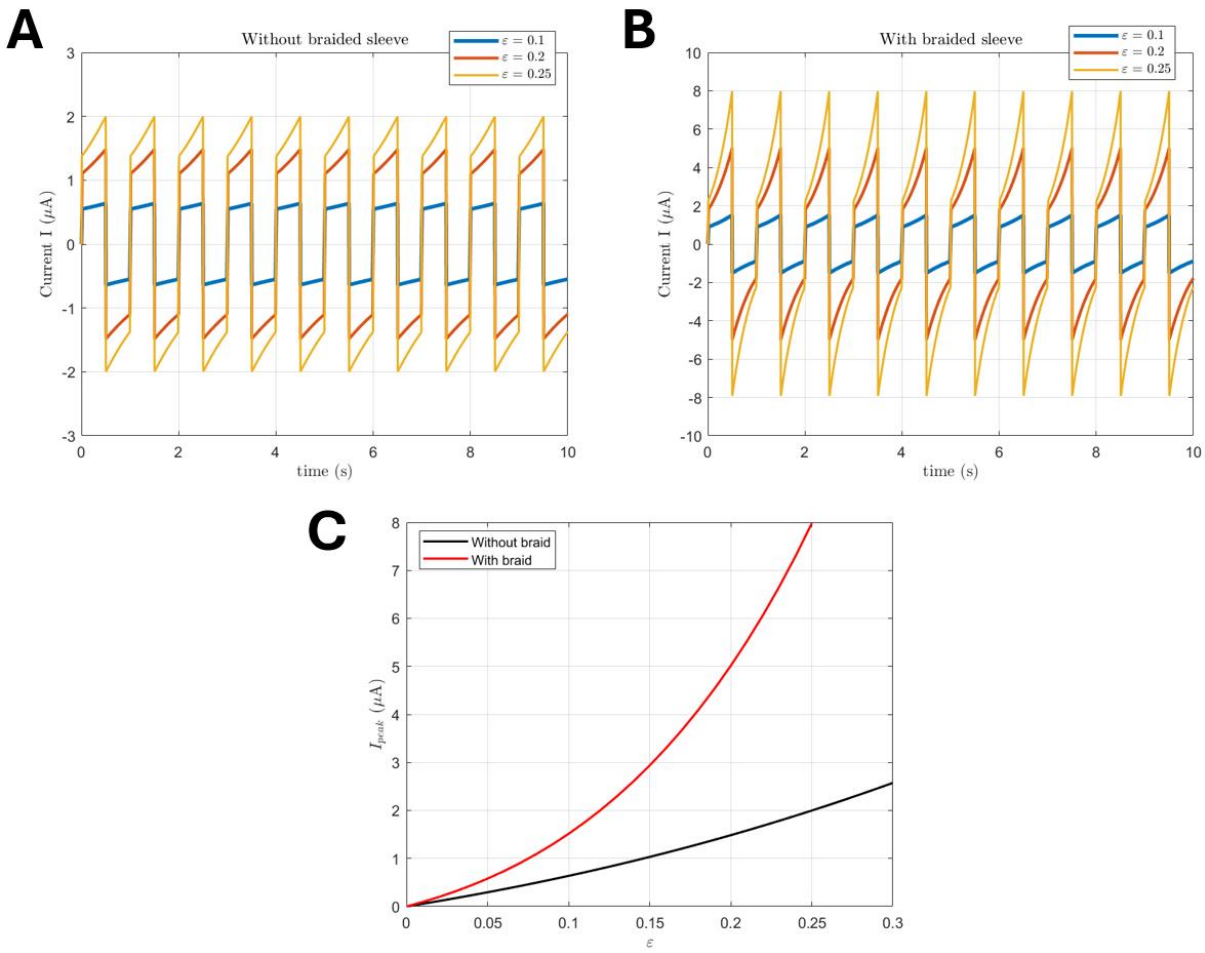

Figure 4.11. Simulated induced current response to 10%, 20%, and 25% axial strain on the working electrode without (A) and with (B) the helically braided sleeve. A comparison of model predicted peak current value with respect to axial strain with (in red) and without (in black) the braided sleeve is shown in (C).

4.2.4 Experimental validation

To validate the trends predicted by simulation, induced current responses were experimentally measured for the fabricated soft supercapacitor with different mechanical inputs. These current responses were compared with and without the presence of the fiber reinforced braided sleeve. Custom clamps were 3D-printed and used to secure the device to the jaws of an Instron (Model #5943) tensile testing apparatus as shown in **Figure 4.12**. Figure 4.12C shows the starting braid angle was measured to be **48°** via image analysis.

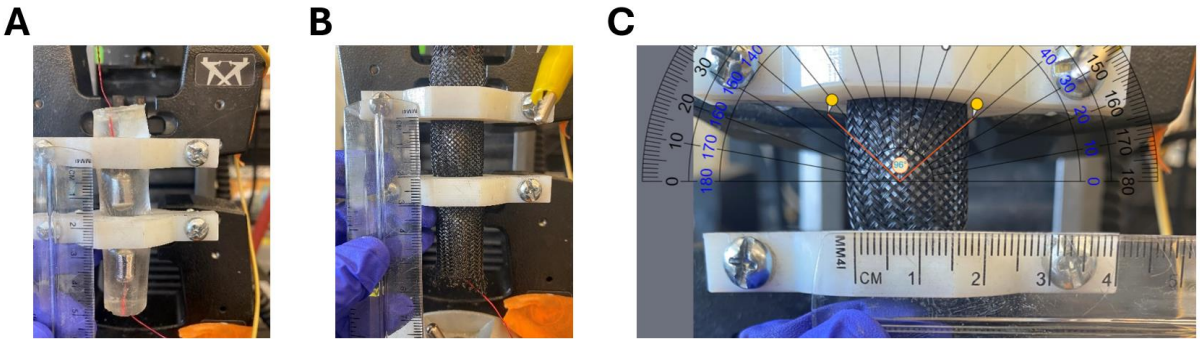

Figure 4.12. Image of soft supercapacitor clamped to Instron without (A) and with (B) the braided sleeve. The measured starting braid angle of the soft supercapacitor at rest is shown in (C), where $\boldsymbol{\theta_0 = \frac{96°}{2} = 48°}$.

One clamp is secured between the two electrodes and held by the stationary jaw of the Instron while the moving jaw of the Instron holds the other clamp located just above the working electrode. This clamping configuration allows for the working electrode to be stretched while the reference electrode remains at rest.

Chronoamperometry measurements were collected for several cyclic stretch profiles with triangle waveforms applied to the working electrode. The axial strain here is determined based on the peak-to-peak amplitude of the prescribed waveform and the initial distance between the clamps. The initial distance measured between the clamps was **17 mm** without the braid and **20mm** with the braid as seen in Figure 4.12A and Figure 4.12B. Triangle stretch waveforms

with peak amplitudes of 1mm to 5mm at 1mm increments were prescribed at 1 Hz and the resulting current measurements are shown in **Figure 4.13**.

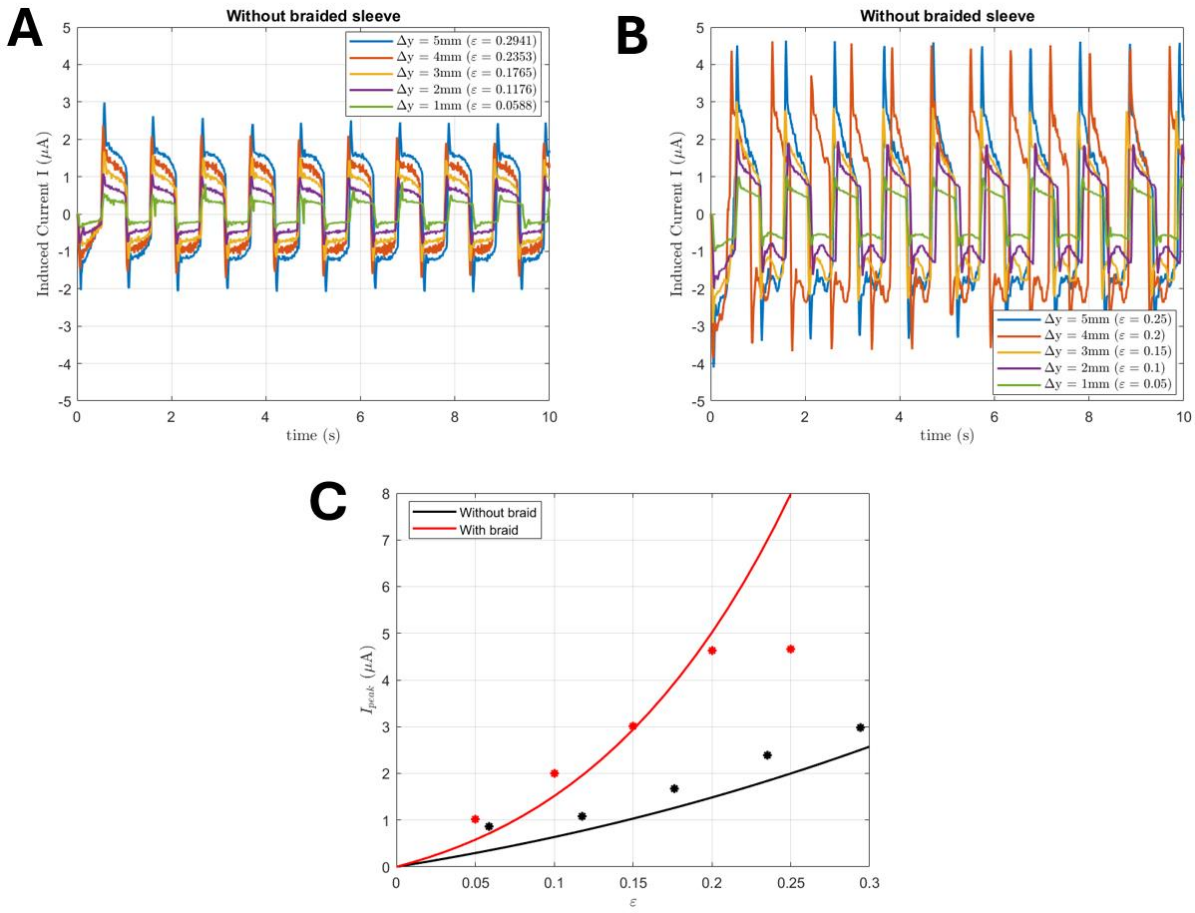

Figure 4.13. Experimental chronoamperometry measurements for prescribed peak amplitude for 1mm to 5mm in 1mm increments at 1 Hz for soft supercapacitor without (A) and with (B) the helically braided fiber reinforced sleeve, where strain values shown in legends correspond to the peak amplitudes. Peak current values measured (filled circle markers) are compared to model predictions (solid line) in (C), where red corresponds to the presence of the braided sleeve and black is associated with the absence of the braided sleeve.

Experimental measurements show a gradual increase in peak current values for the soft supercapacitor without the fiber reinforced braided sleeve and a more rapid growth with the

braided sleeve, which aligns with model simulation predictions. Although the experimental peak current values for the device with the braided sleeve are smaller than the model predictions at large axial strains, the observed values remain larger than those without the braided sleeve. These results validate that the presence of a braided sleeve improves the performance of the soft supercapacitor by increasing the change in EDL area sensitivity to axial deformation.

4.3 Conclusions

This paper explores the design, analysis, and experimental demonstration of a soft electromechanical sensor or energy harvesting device based on a deformable supercapacitor with a helically braided sleeve mechanical reinforcement. The liquid metal electrodes in this entirely soft variable area electrochemical supercapacitor allows the EDL area to change in response to axial stretch strain applied to the device. Analysis of the braided sleeve kinematics reveals an increase in radial compression of the electrode per axial stretch, resulting in greater change in EDL area to improve the electrical output performance of the soft supercapacitor. Simulations of induced current response to prescribed axial deformation of the soft supercapacitor with and without the presence of the fiber reinforced braided sleeve illustrate the effect of this behavior. Results show a significant increase in peak current values with the braided sleeve as compared to a smaller increase without the braided sleeve. We utilize electrochemical analysis techniques and cyclic voltammetry and chronoamperometry to estimate the change in total capacitance of the device and measure induced current response for axial deformations of the electrode, respectively. These induced current responses were measured experimentally for mechanical strains applied to the working electrode. The peak current measurements validated the model-predicted trends and demonstrated that the braided sleeve provides a greater capacitance change and therefore current generated in the circuit.

This work presents a method to improve the axial deformation sensitivity to this type of soft supercapacitor sensor or energy harvester by introducing a helically braided fiber reinforced sleeve. While contributions from this work enable the progression of implementing soft energy harvesting devices in practical applications, challenges remain such as low water retention in the hydrogel that can alter conductivity of the gel, and the oxidation of gallium may decrease the potential over extended periods of time. Future work should explore new gel materials with these concerns in mind to offer a longer shelf life and optimize the performance of this soft electromechanical transducer.

4.4 Experimental Section/Methods

Materials: Eutectic mixture of gallium and indium (EGaIn) was purchased from Indium Corporation, Acrylamide, 2-hydroxy-4'-(2-hydroxethoxy)-2-methylpropiopheneone (Irgacure 2959), N-N'-methylenebis(acrylamide) (MBA) was purchased from Sigma Aldrich. Sodium chloride (NaCl) was purchased from Fisher Scientific. A 5mm glass rod was purchased from McMaster Carr. Non-UV resistant acrylic tubing and sheets were purchased from Amazon. Custom molds were used to fabricate devices from acrylic tubing and sheets. Laser writer (Universal Laser Systems VLS 3.5) was used to cut the sheets to desired shapes and sizes.

Fabrication of soft supercapacitor: Acrylamide pre-gel solution (30% W/V acrylamide (monomer), 0.04% W/V MBA (crosslinker), 0.13% W/V Irgacure 2959 (initiator)) was used to make the hydrogel. This pre-gel solution is cured under a $55\,\frac{mW}{cm^2}$ intensity UV lamp in the mold at an upright position for 4 minutes first, then flipped on its side to cure for another 3 minutes to make the hydrogel casing. The cavity is first filled as desired with liquid metal and additional pre-gel solution is added on top of the liquid metal and cured under the UV lamp for 90 seconds. This step is repeated to make the second liquid metal electrode in the device.

Characterization: The Biologic SP 200 potentiostat was used to carry out electrochemical analysis techniques. 24-gauge (0.02 in) copper wires were inserted into the hydrogel to create electrical connections, and no metal leakage was observed. Instron Model #5943 was used to apply prescribed mechanical inputs to the device.

CHAPTER 5: Key research contributions and suggested future investigations

5.1 Implications of spatially constrained bipennate topology on FAM bundle actuation

5.1.1 Contributions

- …A method of designing bipennate fluidic artificial muscle bundle topologies under spatial bounding volume constraints was presented.
- …Two fiber boundary conditions – fiber contact and pinned – were explored to investigate the implications of incorporating an idealized bioinspired connective tissue functionality as compared to maintaining clearance between fibers via fixed pin joints, respectively.
- Analysis revealed that, for the given spatial volume constraint, bipennate topologies can be found to produce muscle output force, muscle contraction, muscle stiffness, or work output capacity larger than that of a parallel muscle bundle topology. Thus, depending on the fiber boundary conditions, a bipennate bundle may offer distinct advantages over a more conventional parallel bundle.
- The fiber contact boundary condition enables additional fibers to be packed into the fixed bounding envelope through elimination of minimum fiber clearance required in the pinned boundary condition.
- The extensile motion found in muscle topologies with the fiber contact bounding condition also enables the bipennate muscle topology to behave as a negative stiffness structure. Furthermore, mechanical singularity was discovered as a byproduct of the fiber contact boundary condition.
- …Configuring a bipennate topology to simulataneously maximize fiber contraction and fiber rotation does not yield the largest muscle stroke and results in less contraction than that of a parallel topology with equal bounding envelope. Rather, peak muscle displacement is produced by a bipennate topology with a small (but non-zero) initial pennation angle that exploits both longer fibers and rotation effects.

5.1.2 Future Investigations

Future work will include experiments to investigate these trends in bipennate muscle bundles with the fiber contact boundary condition. To advance our understanding in the design of pennate muscle topologies, future work should explore implications of muscle topology design on efficiency in tracking a dynamic motion and evaluate muscle performance sensitivity to variation in muscle thickness during actuation.

5.2. Genetic algorithm-based optimization tool for spatially constrained FAM bundle

5.2.1 Contributions

- …A custom multi-objective genetic algorithm framework was used to quantify the architectural tradeoff between force and stroke with respect to the specified spatial envelope.
- …The generated Pareto frontier not only outlines the bundle force and stroke limit for a given pressure in the design space but maps the force and stroke tradeoff to different optimal FAM bundle designs.
- …The analysis reveals when to consider laterally arranged FAMs and centrally arranged FAMs based on the desired force and stroke of the bundle. This design decision is not one that could have been made before.
- …A select number of designs along the 12 × 6 × 1 aspect ratio Pareto frontier were fabricated and tested to compare with the model predicted bundle force and contraction.
- …Two other aspect ratios (6 × 12 × 1 and √72 × √72 × 1) were explored in this study while spatial volume was maintained to observe geometric constraint impacts optimal FAM bundle designs.

- …The capacity of this optimization method allows for investigation of different spatial envelopes and further exploration of spatial envelope implications on FAM bundle design.
- …This framework was not limited to FAMs, as it can also be applicable for other types of soft actuators subject to geometric constraints to properly size, arranged, and orient actuator units based on desired objectives.
- …This work lays the foundation for studying emergent behavior of biological muscle architecture, e.g. answering physiological and evolutionary questions like: Why does the biceps brachii muscle have a fusiform parallel architecture while the extensor diatorum muscle have a unipennate architecture? Why are the hip and knee joints in the body actuated by multiple muscles with parallel, unipennate, bipennate, and circumpennate fiber architectures that depend on the muscle location in the anterior or lateral compartment of the leg, and how are the muscles coordinated for different tasks?

5.2.2 Future Investigations

Future work should explore non-uniform spatial bounds, non-planar bundle arrangements, and consider heterogeneous actuators to improve tracking performance or efficiency in dynamic applications.

5.3 Strain amplified soft supercapacitor with helically braided fiber reinforced sleeve

5.3.1 Contributions

- …Analysis of the braided sleeve kinematics revealed an increase in radial compression of the electrode per axial stretch, resulting in greater change in EDL area to improve the electrical output performance of the soft supercapacitor.

- …Simulations of induced current response to prescribed axial deformation of the soft supercapacitor with and without the presence of the fiber reinforced braided sleeve illustrate the effect of this increased change in EDL area.
- …Generated results show a significant increase in peak current values with the braided sleeve as compared to a smaller increase without the braided sleeve.
- …Electrochemical analysis techniques (cyclic voltammetry and chronoamperometry) were used to estimate the change in total capacitance of the device and measure induced current response for axial deformations of the electrode, respectively.
- …The peak current measurements from chronoamperometry validated the model-predicted trends and demonstrated that the braided sleeve provides a greater capacitance change and therefore current generated in the circuit.

5.3.2 Future Investigations

While contributions from this work enable the progression of implementing soft energy harvesting devices in practical applications, challenges remain such as low water retention in the hydrogel that can alter conductivity of the gel, and the oxidation of gallium may decrease the potential over extended periods of time. Future work should explore new gel materials with these concerns in mind to offer a longer shelf life and optimize the performance of this soft electromechanical transducer.

5.4 Final Conclusions

The potential for soft actuators and sensors adds value to many fields beyond robotics and energy harvesters. This work of hierarchical actuation allows for better energy efficiency and versatility. The focus on architectural design enables spatial optimal packaging while a soft construction provides compatibility that is safe to human interaction. This work will hopefully be insightful for future research to continue investigating the possibilities of soft devices.

REFERENCES

[1] S. Bauer, S. Bauer-Gogonea, I. Graz, M. Kaltenbrunner, C. Keplinger, R. Schwödiauer, 25th anniversary article: A soft future: From robots and sensor skin to energy harvesters, Advanced Materials 26 (2014) 149–162. https://doi.org/10.1002/adma.201303349.

[2] D. Chen, Q. Pei, Electronic Muscles and Skins: A Review of Soft Sensors and Actuators, Chem Rev 117 (2017) 11239–11268. https://doi.org/10.1021/acs.chemrev.7b00019.

[3] Z. Xue, H. Song, J.A. Rogers, Y. Zhang, Y. Huang, Mechanically-Guided Structural Designs in Stretchable Inorganic Electronics, Advanced Materials 32 (2020). https://doi.org/10.1002/adma.201902254.

[4] M.D. Dickey, Stretchable and Soft Electronics using Liquid Metals, Advanced Materials 29 (2017). https://doi.org/10.1002/adma.201606425.

[5] T.Q. Trung, N.E. Lee, Recent Progress on Stretchable Electronic Devices with Intrinsically Stretchable Components, Advanced Materials 29 (2017). https://doi.org/10.1002/adma.201603167.

[6] W. Zeng, L. Shu, Q. Li, S. Chen, F. Wang, X.M. Tao, Fiber-based wearable electronics: A review of materials, fabrication, devices, and applications, Advanced Materials 26 (2014) 5310–5336. https://doi.org/10.1002/adma.201400633.

[7] M. Stoppa, A. Chiolerio, Wearable electronics and smart textiles: A critical review, Sensors (Switzerland) 14 (2014) 11957–11992. https://doi.org/10.3390/s140711957.

[8] Y. Liu, M. Pharr, G.A. Salvatore, Lab-on-Skin: A Review of Flexible and Stretchable Electronics for Wearable Health Monitoring, ACS Nano 11 (2017) 9614–9635. https://doi.org/10.1021/acsnano.7b04898.

[9] M. Ha, S. Lim, H. Ko, Wearable and flexible sensors for user-interactive health-monitoring devices, J Mater Chem B 6 (2018) 4043–4064. https://doi.org/10.1039/c8tb01063c.

[10] T.R. Ray, J. Choi, A.J. Bandodkar, S. Krishnan, P. Gutruf, L. Tian, R. Ghaffari, J.A. Rogers, Bio-integrated wearable systems: A comprehensive review, Chem Rev 119 (2019) 5461–5533. https://doi.org/10.1021/acs.chemrev.8b00573.

[11] Y.M. Wang, T. Voisin, J.T. McKeown, J. Ye, N.P. Calta, Z. Li, Z. Zeng, Y. Zhang, W. Chen, T.T. Roehling, R.T. Ott, M.K. Santala, P.J. Depond, M.J. Matthews, A. V. Hamza, T. Zhu, Additively manufactured hierarchical stainless steels with high strength and ductility, Nat Mater 17 (2018) 63–70. https://doi.org/10.1038/NMAT5021.

[12] C. Majidi, Soft Robotics: A Perspective - Current Trends and Prospects for the Future, Soft Robot 1 (2014) 5–11. https://doi.org/10.1089/soro.2013.0001.

[13] P. Polygerinos, N. Correll, S.A. Morin, B. Mosadegh, C.D. Onal, K. Petersen, M. Cianchetti, M.T. Tolley, R.F. Shepherd, Soft Robotics: Review of Fluid-Driven Intrinsically Soft Devices; Manufacturing, Sensing, Control, and Applications in Human-Robot Interaction, Adv Eng Mater 19 (2017). https://doi.org/10.1002/adem.201700016.

[14] N. Lu, D.H. Kim, Flexible and Stretchable Electronics Paving the Way for Soft Robotics, Soft Robot 1 (2014) 53–62. https://doi.org/10.1089/soro.2013.0005.

[15] S. Coyle, C. Majidi, P. LeDuc, K.J. Hsia, Bio-inspired soft robotics: Material selection, actuation, and design, Extreme Mech Lett 22 (2018) 51–59. https://doi.org/10.1016/j.eml.2018.05.003.

[16] N. El-Atab, R.B. Mishra, F. Al-Modaf, L. Joharji, A.A. Alsharif, H. Alamoudi, M. Diaz, N. Qaiser, M.M. Hussain, Soft Actuators for Soft Robotic Applications: A Review, Advanced Intelligent Systems 2 (2020). https://doi.org/10.1002/aisy.202000128.

[17] J.H. So, J. Thelen, A. Qusba, G.J. Hayes, G. Lazzi, M.D. Dickey, Reversibly deformable and mechanically tunable fluidic antennas, Adv Funct Mater 19 (2009) 3632–3637. https://doi.org/10.1002/adfm.200900604.
[18] A. Adamatzky, A brief history of liquid computers, Philosophical Transactions of the Royal Society B: Biological Sciences 374 (2019). https://doi.org/10.1098/rstb.2018.0372.
[19] Y. Jin, Y. Lin, A. Kiani, I.D. Joshipura, M. Ge, M.D. Dickey, Materials tactile logic via innervated soft thermochromic elastomers, Nat Commun 10 (2019). https://doi.org/10.1038/s41467-019-12161-1.
[20] M.D. Bartlett, N. Kazem, M.J. Powell-Palm, X. Huang, W. Sun, J.A. Malen, C. Majidi, High thermal conductivity in soft elastomers with elongated liquid metal inclusions, Proc Natl Acad Sci U S A 114 (2017) 2143–2148. https://doi.org/10.1073/pnas.1616377114.
[21] G. Yun, S.Y. Tang, S. Sun, D. Yuan, Q. Zhao, L. Deng, S. Yan, H. Du, M.D. Dickey, W. Li, Liquid metal-filled magnetorheological elastomer with positive piezoconductivity, Nat Commun 10 (2019). https://doi.org/10.1038/s41467-019-09325-4.
[22] S.C.B. Mannsfeld, B.C.K. Tee, R.M. Stoltenberg, C.V.H.H. Chen, S. Barman, B.V.O. Muir, A.N. Sokolov, C. Reese, Z. Bao, Highly sensitive flexible pressure sensors with microstructured rubber dielectric layers, Nat Mater 9 (2010) 859–864. https://doi.org/10.1038/nmat2834.
[23] J. Yang, D. Tang, J. Ao, T. Ghosh, T. V. Neumann, D. Zhang, E. Piskarev, T. Yu, V.K. Truong, K. Xie, Y.C. Lai, Y. Li, M.D. Dickey, Ultrasoft Liquid Metal Elastomer Foams with Positive and Negative Piezopermittivity for Tactile Sensing, Adv Funct Mater 30 (2020). https://doi.org/10.1002/adfm.202002611.
[24] M.D. Bartlett, A. Fassler, N. Kazem, E.J. Markvicka, P. Mandal, C. Majidi, Stretchable, High-k Dielectric Elastomers through Liquid-Metal Inclusions, Advanced Materials 28 (2016) 3726–3731. https://doi.org/10.1002/adma.201506243.
[25] K. Sim, Z. Rao, F. Ershad, C. Yu, Rubbery Electronics Fully Made of Stretchable Elastomeric Electronic Materials, Advanced Materials 32 (2020). https://doi.org/10.1002/adma.201902417.
[26] S. Coyle, C. Majidi, P. LeDuc, K.J. Hsia, Bio-inspired soft robotics: Material selection, actuation, and design, Extreme Mech Lett 22 (2018) 51–59. https://doi.org/10.1016/j.eml.2018.05.003.
[27] R. Vepa, Biomimetic Robotics, in: Engineered Biomimicry, Elsevier Inc., 2013: pp. 81–105. https://doi.org/10.1016/B978-0-12-415995-2.00004-0.
[28] J.G. Betts, P. Desaix, E. Johnson, J.E. Johnson, O. Korol, D. Kruse, B. Poe, J.A. Wise, M. Womble, K.A. Young, Anatomy and Physiology, OpenStax, 2022.
[29] D. Huston, B. Esser, G. Spencer, D. Burns, E. Kahn, Hierarchical actuator systems, in: Smart Structures and Materials 2005: Industrial and Commercial Applications of Smart Structures Technologies, SPIE, 2005: p. 311. https://doi.org/10.1117/12.607220.
[30] J. Ueda, J.A. Schultz, H.H. Asada, Cellular Actuators, 2017.
[31] C.A. Oatis, Biomechanics of Skeletal Muscle, in: Kinesiology: The Mechanics and Pathomechanics of Human Movement, 2nd ed., LippincottWilliams&Wilkins, 2008.
[32] Z. Zhang, M. Philen, Pressurized artificial muscles, J Intell Mater Syst Struct 23 (2012) 255–268. https://doi.org/10.1177/1045389X11420592.
[33] B. Tondu, Modelling of the McKibben artificial muscle: A review, J Intell Mater Syst Struct 23 (2012) 225–253. https://doi.org/10.1177/1045389X11435435.

[34] G.K. Klute, B. Hannaford, Accounting for Elastic Energy Storage in McKibben Artificial Muscle Actuators, JournalofDynamicSystems,Measurement,AndControl 122 (2000) 386–388. http://asmedigitalcollection.asme.org/dynamicsystems/article-pdf/122/2/386/5495750/354_1.pdf.
[35] C.S. Kothera, M. Jangid, J. Sirohi, N.M. Wereley, Experimental characterization and static modeling of McKibben actuators, Journal of Mechanical Design 131 (2009) 0910101–09101010. https://doi.org/10.1115/1.3158982.
[36] M.A. Meller, M. Bryant, E. Garcia, Reconsidering the McKibben muscle: Energetics, operating fluid, and bladder material, J Intell Mater Syst Struct 25 (2014) 2276–2293. https://doi.org/10.1177/1045389X14549872.
[37] W. Wojnicz, B. Zagrodny, M. Ludwicki, J. Awrejcewicz, E. Wittbrodt, A two dimensional approach for modelling of pennate muscle behaviour, Biocybern Biomed Eng 37 (2017) 302–315. https://doi.org/10.1016/j.bbe.2016.12.004.
[38] E. Azizi, E.L. Brainerd, T.J. Roberts, Variable gearing in pennate muscles, 2008. www.pnas.orgcgidoi10.1073pnas.0709212105.
[39] T. Jenkins, M. Bryant, Pennate actuators: Force, contraction and stiffness, Bioinspir Biomim 15 (2020). https://doi.org/10.1088/1748-3190/ab860f.
[40] F.U. Khan, M.U. Qadir, State-of-the-art in vibration-based electrostatic energy harvesting, Journal of Micromechanics and Microengineering 26 (2016). https://doi.org/10.1088/0960-1317/26/10/103001.
[41] V. Vallem, E. Roosa, T. Ledinh, W. Jung, T. il Kim, S. Rashid-Nadimi, A. Kiani, M.D. Dickey, A Soft Variable-Area Electrical-Double-Layer Energy Harvester, Advanced Materials 33 (2021). https://doi.org/10.1002/adma.202103142.
[42] E. Azizi, T.J. Roberts, Variable gearing in a biologically inspired pneumatic actuator array, Bioinspir Biomim 8 (2013). https://doi.org/10.1088/1748-3182/8/2/026002.
[43] C.M. Eng, E. Azizi, T.J. Roberts, Structural determinants of muscle gearing during dynamic contractions, Integr Comp Biol 58 (2018) 207–218. https://doi.org/10.1093/icb/icy054.
[44] G. Mathijssen, D. Lefeber, B. Vanderborght, Variable recruitment of parallel elastic elements: Series-parallel elastic actuators (SPEA) with dephased mutilated gears, IEEE/ASME Transactions on Mechatronics 20 (2015) 594–602. https://doi.org/10.1109/TMECH.2014.2307122.
[45] M. Bryant, M.A. Meller, E. Garcia, Variable recruitment fluidic artificial muscles: Modeling and experiments, Smart Mater Struct 23 (2014). https://doi.org/10.1088/0964-1726/23/7/074009.
[46] M. Meller, J. Chipka, A. Volkov, M. Bryant, E. Garcia, Improving actuation efficiency through variable recruitment hydraulic McKibben muscles: Modeling, orderly recruitment control, and experiments, Bioinspir Biomim 11 (2016). https://doi.org/10.1088/1748-3190/11/6/065004.
[47] R.M. Robinson, C.S. Kothera, N.M. Wereley, Variable Recruitment Testing of Pneumatic Artificial Muscles for Robotic Manipulators, IEEE/ASME Transactions on Mechatronics 20 (2015) 1642–1652. https://doi.org/10.1109/TMECH.2014.2341660.
[48] E. Azizi, T.J. Roberts, Variable gearing in a biologically inspired pneumatic actuator array, Bioinspir Biomim 8 (2013). https://doi.org/10.1088/1748-3182/8/2/026002.
[49] S. Kianzad, M. Pandit, J.D. Lewis, A.R. Berlingeri, K.J. Haebler, J.D.W. Madden, Variable stiffness structure using nylon actuators arranged in a pennate muscle

configuration, in: Electroactive Polymer Actuators and Devices (EAPAD) 2015, SPIE, 2015: p. 94301Z. https://doi.org/10.1117/12.2086799.
[50] T.E. Jenkins, M. Bryant, Variable stiffness soft robotics using pennate muscle architecture, in: SPIE-Intl Soc Optical Eng, 2019: p. 4. https://doi.org/10.1117/12.2514265.
[51] W. Wojnicz, B. Zagrodny, M. Ludwicki, J. Awrejcewicz, E. Wittbrodt, A two dimensional approach for modelling of pennate muscle behaviour, Biocybern Biomed Eng 37 (2017) 302–315. https://doi.org/10.1016/j.bbe.2016.12.004.
[52] C. Stecco, W. Hammer, A. Vleeming, R. De Caro, Functional Atlas of the Human Fascial System, Elsevier Ltd., 2015.
[53] B. Tondu, P. Lopez, Modeling and Control of McKibben Artificial Muscle Robot Actuators, IEEE Control Syst 20 (2000) 15–38. https://doi.org/10.1109/37.833638.
[54] R.McN. Alexander, The orientation of muscle fibres in the myomeres of fishes, JournaloftheMarineBiologicalAssociationoftheUnitedKingdom 40 (1969) 263–290.
[55] M.S. Miller, B.M. Palmer, M.J. Toth, D.M. Warshaw, CHAPTER 5, n.d.
[56] T.J. Roberts, C.M. Eng, D.A. Sleboda, N.C. Holt, E.L. Brainerd, K.K. Stover, R.L. Marsh, E. Azizi, The multi-scale, three-dimensional nature of skeletal muscle contraction, Physiology 34 (2019) 402–408. https://doi.org/10.1152/physiol.00023.2019.
[57] M. Bryant, M.A. Meller, E. Garcia, Variable recruitment fluidic artificial muscles: Modeling and experiments, Smart Mater Struct 23 (2014). https://doi.org/10.1088/0964-1726/23/7/074009.
[58] M. Meller, J. Chipka, A. Volkov, M. Bryant, E. Garcia, Improving actuation efficiency through variable recruitment hydraulic McKibben muscles: Modeling, orderly recruitment control, and experiments, Bioinspir Biomim 11 (2016). https://doi.org/10.1088/1748-3190/11/6/065004.
[59] R.M. Robinson, C.S. Kothera, N.M. Wereley, Variable Recruitment Testing of Pneumatic Artificial Muscles for Robotic Manipulators, IEEE/ASME Transactions on Mechatronics 20 (2015) 1642–1652. https://doi.org/10.1109/TMECH.2014.2341660.
[60] G. Mathijssen, D. Lefeber, B. Vanderborght, Variable recruitment of parallel elastic elements: Series-parallel elastic actuators (SPEA) with dephased mutilated gears, IEEE/ASME Transactions on Mechatronics 20 (2015) 594–602. https://doi.org/10.1109/TMECH.2014.2307122.
[61] R. Tiwari, M.A. Meller, K.B. Wajcs, C. Moses, I. Reveles, E. Garcia, Hydraulic artificial muscles, J Intell Mater Syst Struct 23 (2012) 301–312. https://doi.org/10.1177/1045389X12438627.
[62] B. Tondu, P. Lopez, Modeling and Control of McKibben Artificial Muscle Robot Actuators, IEEE Control Syst 20 (2000) 15–38. https://doi.org/10.1109/37.833638.
[63] J.Y. Kim, N. Mazzoleni, M. Bryant, Modeling of resistive forces and buckling behavior in variable recruitment fluidic artificial muscle bundles, Actuators 10 (2021) 1–24. https://doi.org/10.3390/act10030042.
[64] J.Y. Kim, M. Bryant, Electrohydraulic System Analysis of Variable Recruitment Fluidic Artificial Muscle Bundles With Interaction Effects, Journal of Dynamic Systems, Measurement and Control, Transactions of the ASME 146 (2024). https://doi.org/10.1115/1.4064092.

[65] N. Mazzoleni, J.Y. Kim, M. Bryant, Motor unit buckling in variable recruitment fluidic artificial muscle bundles: implications and mitigations, Smart Mater Struct 31 (2022). https://doi.org/10.1088/1361-665X/ac49d9.
[66] M.U.A. Khan, A. Ali, R. Muneer, M. Faisal, Pneumatic artificial muscle-based stroke rehabilitation device for upper and lower limbs, Intell Serv Robot 17 (2024) 33–42. https://doi.org/10.1007/s11370-023-00509-y.
[67] A. Nikkhah, C. Bradley, A. Sharif Ahmadian, Design, dynamic modeling, control and implementation of hydraulic artificial muscles in antagonistic pair configuration, Mech Mach Theory 153 (2020). https://doi.org/10.1016/j.mechmachtheory.2020.104007.
[68] E. Duan, M. Bryant, Implications of Spatially Constrained Bipennate Topology on Fluidic Artificial Muscle Bundle Actuation, Actuators 11 (2022). https://doi.org/10.3390/act11030082.
[69] T.E. Jenkins, M. Bryant, Variable stiffness soft robotics using pennate muscle architecture, in: SPIE-Intl Soc Optical Eng, 2019: p. 4. https://doi.org/10.1117/12.2514265.
[70] H. Nesser, G. Lubineau, Strain Sensing by Electrical Capacitive Variation: From Stretchable Materials to Electronic Interfaces, Adv Electron Mater 7 (2021). https://doi.org/10.1002/aelm.202100190.
[71] V. Vallem, Y. Sargolzaeiaval, M. Ozturk, Y.C. Lai, M.D. Dickey, Energy Harvesting and Storage with Soft and Stretchable Materials, Advanced Materials 33 (2021). https://doi.org/10.1002/adma.202004832.
[72] S. Park, K. Parida, P.S. Lee, Deformable and Transparent Ionic and Electronic Conductors for Soft Energy Devices, Adv Energy Mater 7 (2017). https://doi.org/10.1002/aenm.201701369.
[73] C. Keplinger, J.Y. Sun, C.C. Foo, P. Rothemund, G.M. Whitesides, Z. Suo, Stretchable, transparent, ionic conductors, Science (1979) 341 (2013) 984–987. https://doi.org/10.1126/science.1240228.
[74] H. Wu, Y.A. Huang, F. Xu, Y. Duan, Z. Yin, Energy Harvesters for Wearable and Stretchable Electronics: From Flexibility to Stretchability, Advanced Materials 28 (2016) 9881–9919. https://doi.org/10.1002/adma.201602251.
[75] B. Pal, S. Yang, S. Ramesh, V. Thangadurai, R. Jose, Electrolyte selection for supercapacitive devices: A critical review, Nanoscale Adv 1 (2019) 3807–3835. https://doi.org/10.1039/c9na00374f.
[76] J.K. Moon, J. Jeong, D. Lee, H.K. Pak, Electrical power generation by mechanically modulating electrical double layers, Nat Commun 4 (2013). https://doi.org/10.1038/ncomms2485.
[77] C.W. Evans, Hose Technology, AppliedSciencePublishers, London, 1974.
[78] P.J. Stroempl, Hose Reinforcement Analysis, Management Science and Engineering 12 (2018) 16–20. https://doi.org/10.3968/10589.
[79] M.D. Dickey, R.C. Chiechi, R.J. Larsen, E.A. Weiss, D.A. Weitz, G.M. Whitesides, Eutectic gallium-indium (EGaIn): A liquid metal alloy for the formation of stable structures in microchannels at room temperature, Adv Funct Mater 18 (2008) 1097–1104. https://doi.org/10.1002/adfm.200701216.
[80] A.J.. Bard, L.R.. Faulkner, Electrochemical methods : fundamentals and applications, John Wiley & Sons, Inc., 2001.

[81] B.E. Conway, Electrochemical Supercapacitors Scientific Fundamentals and Technological Applications, KluwerAcademic/PlenumPublishers, NewYork, 1999.
[82] R.L. Spyker, I.R. M Nelms, S. Member, Classical Equivalent Circuit Parameters for a Double-Layer Capacitor, n.d.
[83] H. Yamada, K. Yoshii, M. Asahi, M. Chiku, Y. Kitazumi, Cyclic Voltammetry Part 1: Fundamentals†, Electrochemistry 90 (2022). https://doi.org/10.5796/ELECTROCHEMISTRY.22-66082.
[84] N. Elgrishi, K.J. Rountree, B.D. McCarthy, E.S. Rountree, T.T. Eisenhart, J.L. Dempsey, A Practical Beginner's Guide to Cyclic Voltammetry, J Chem Educ 95 (2018) 197–206. https://doi.org/10.1021/acs.jchemed.7b00361.
[85] D.R. Lide, G. Baysinger, L.I. Berger, R.N. Goldberg, H. V Kehiaian, K. Kuchitsu, D.L. Roth, D. Zwillinger, CRC Handbook of Chemistry and Physics Editor-in-Chief, n.d.
[86] A.V. Wolf, Aqueous Solutions and Body Fluids, 1st ed., Harper&Row, NewYork, 1966.

APPENDICES

Appendix A.

Supplementary videos are provided as representative illustrations of muscle bundles during actuation. Video S1 corresponds to a muscle bundle with fiber contact boundary condition while video S2 corresponds to a muscle bundle with pinned boundary condition. The following supporting information can be downloaded at: https: //www.mdpi.com/article/10.3390/act11030082/s1, Video S1: fibercontact_beta_i_60, Video S2: pinned_beta_i_60. Supplementary videos are provided as representative illustrations of muscle bundles during actuation. Video S1 corresponds to a muscle bundle with fiber contact boundary condition while Video S2 corresponds to a muscle bundle with pinned boundary condition.

Appendix B.

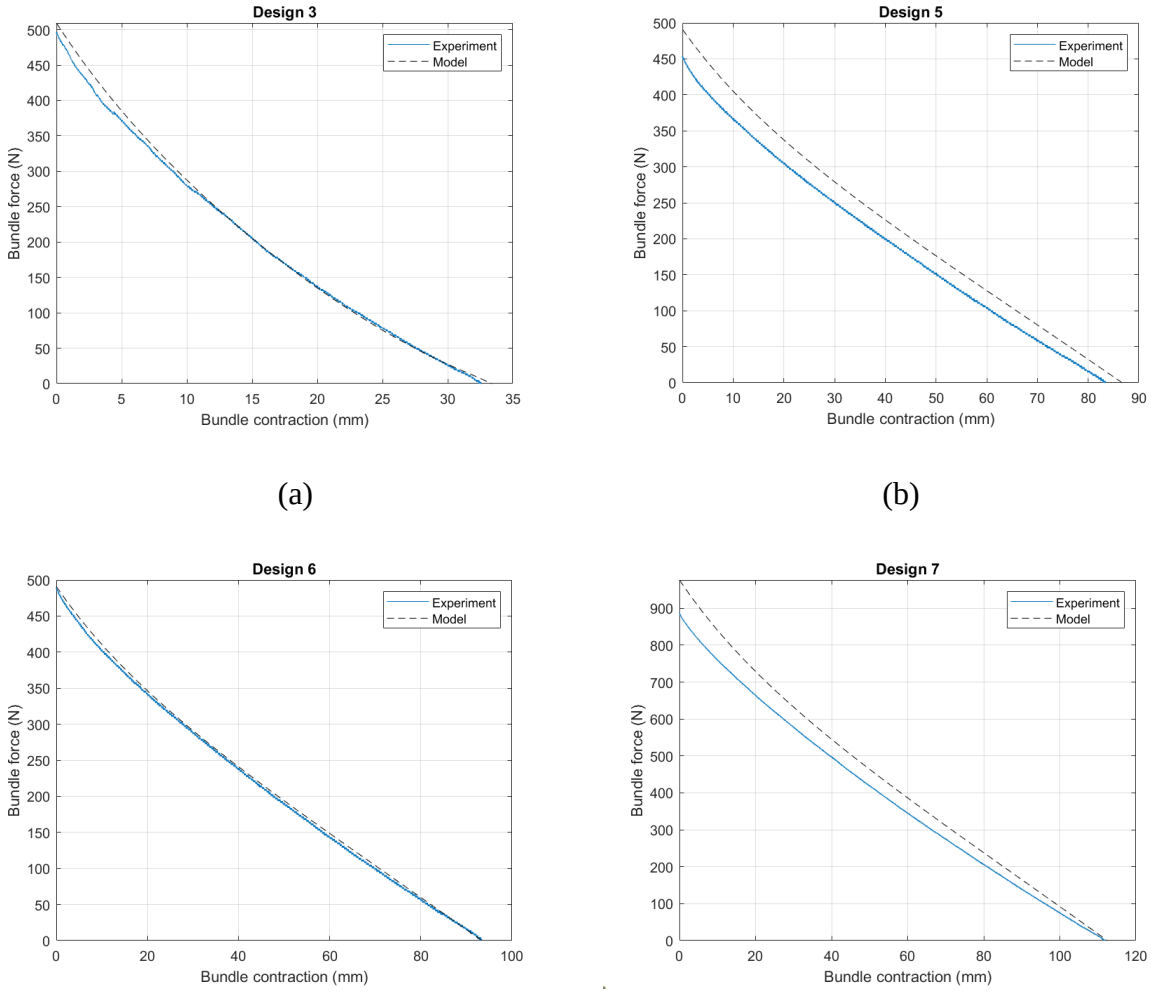

Figure A1. FAM bundle force and contraction model prediction considering as-built parameters (including inactive length) compared to experimental results.

Appendix C.

Supplementary Information

S1. Geometric model

Working electrode length l is expressed in terms of axial strain or stretch ε, where l_0 is the length at rest.

$$l(\varepsilon) = (1 + \varepsilon)l_0 \quad \text{(S1)}$$

The hydrogel and liquid metal electrode are both incompressible materials, which correspond to a Poisson's ratio of $\nu = 0.5$. For a cylindrical geometry, $\nu = \frac{\Delta l}{l_0}\frac{r_0}{\Delta r}$ and can be rearranged to express the radius r_ν as a function of axial strain, where r_0 is the radius at rest.

$$r_\nu = r_0(1 - \nu\varepsilon) = r_0(1 - 0.5\varepsilon) \quad \text{(S2)}$$

The addition of a helically braided fiber reinforced sleeve to this liquid metal hydrogel composite alters this radial deformation. The hydrogel at rest is not sized to fully fill the internal volume of the braided sleeve. When axial stretch is applied, the internal volume of the braided sleeve decreases to compress the hydrogel, which forces the length of the hydrogel to extend and fill the unoccupied internal volume inside the braided sleeve as seen in **Figure S1**.

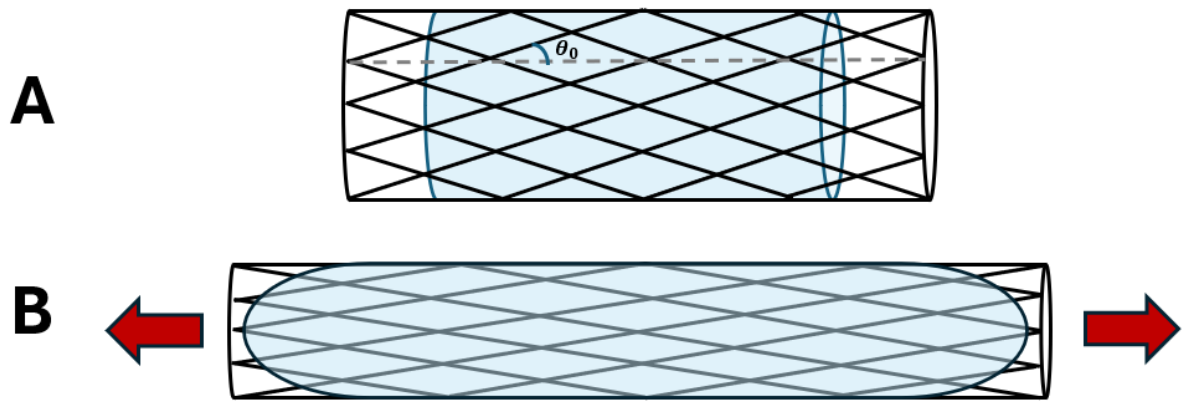

Figure S1. Deformation of hydrogel inside braided sleeve. Excess braided sleeve is present with the hydrogel sized to not fill the internal volume of the braided sleeve at the unloaded state (A). When braided sleeve is stretched, hydrogel is compressed to fill the unoccupied space in the braided sleeve (B).

The starting braid angle θ_0 observed in the network of jointed pantographs on the braided sleeve determines the extent of axial extension or contraction as well as radial expansion or compression. The following expressions describe the kinematic relationship between the parameters of the braided sleeve.

$$\frac{r_\theta}{r_0} = \frac{\sin(\theta)}{\sin(\theta_0)} \qquad \frac{l_\theta}{l_0} = \frac{\cos(\theta)}{\cos(\theta_0)} \tag{S3}$$

The radius including the braided sleeve design r_θ can also be expressed in terms of axial strain as shown below.

$$r_\theta = \frac{r_0}{\sin(\theta_0)}\sqrt{1-(1+\varepsilon)^2 cos^2(\theta_0)} \tag{S4}$$

Since volume is maintained for incompressible materials, these geometric relationships can be used to capture the electrode shape change. The electrode volume V_0 and EDL area A_0 at rest can

be directly computed given the simplicity of the capsule geometry, where $V_0 = \pi {r_0}^2 l_0 + \frac{4}{3}\pi r_0^3$ and $A_0 = 2\pi r_0 l_0 + 2\pi r_0^2$. In the stretched state, the expression for electrode volume becomes $V = \pi r^2 l + \frac{4}{3}\pi a r^2$ since the geometry becomes a cylinder with prolate hemi-ellipsoid ends, where a is a geometric dimension of the hemi-ellipsoid end and related to axial stretch. Because volume remains constant, this geometric dimension can be solved for and used to evaluate for the EDL area as a function of axial stretch, where $e^2 = 1 - \frac{r(\varepsilon)^2}{a(\varepsilon)^2}$.

$$A(\varepsilon) = 2\pi r(\varepsilon) l(\varepsilon) + 2\pi r(\varepsilon)^2 \left(1 + \frac{a(\varepsilon)}{r(\varepsilon) e} \sin^{-1} e\right) \tag{S5}$$

A2. Maximum axial strain with the braided sleeve

The minimum braid angle θ for the dimensions used in this study can be calculated using equation (3) with the rated unexpanded (12.7 mm) diameter of the braided sleeve from the manufacturer. The hydrogel diameter (17.5 mm) and starting braid angle $\theta_0 = 48°$ were measured with the soft supercapacitor at rest.

$$\frac{\left(\frac{12.7\ mm}{2}\right)}{\left(\frac{17.5\ mm}{2}\right)} = \frac{\sin(\theta)}{\sin(48°)} \rightarrow \theta = 32.64° \tag{S6}$$

Equation (1) can be rearranged as follows to express axial strain in terms of starting braid angle.

$$\varepsilon = \frac{l(\varepsilon)}{l_0} - 1 = \frac{\cos(\theta)}{\cos(\theta_0)} - 1 \tag{S7}$$

Based on this expression, a large θ_0 indicates a greater axial strain with the braided sleeve design in this study as shown in Table S1.

Table S1. Maximum axial strain for different starting braid angles

Starting braid angle [degrees]	Maximum axial strain
54	0.4327
48	0.259
42	0.1332

S3. Equivalent circuit model of electrochemical cell for soft supercapacitor

Initially ($t = 0$), the system is at equilibrium, where the voltage across each capacitor is equivalent ($V_{WE} = V_{RE}$) and there is no voltage across the resistor ($I = 0$).

$$\frac{Q_{WE,0}}{C_{WE}(t=0)} = \frac{Q_{RE,0}}{C_{RE}} \tag{S8}$$

, where $Q_{RE,0}$ and $Q_{WE,0}$ are the initial charges on the reference electrode and working electrode EDL capacitor, C_{RE} and C_{WE} are the reference electrode and working electrode EDL capacitance. When the working electrode is axially stretched at time t, the EDL area changes the working electrode EDL capacitance in the system and charges move through the circuit. Thus, the voltage across each capacitor is no longer equal and current is calculated based on Kirchoff's voltage law, where R is the electrolyte resistance and $q(t)$ is the quantity of movement at time t.

$$i(t)R = V_{RE} - V_{WE} = \frac{Q_{RE,0} - q(t)}{C_{RE}} - \frac{Q_{WE,0} + q(t)}{C_{WE}(t)}$$

$$i(t) = \frac{dq(t)}{dt} = \frac{1}{R}\left(\frac{Q_{RE,0} - q(t)}{C_{RE}} - \frac{Q_{WE,0} + q(t)}{C_{WE}(t)}\right) \quad \text{(S9)}$$

At $t = 0$, no charge movement occurs and $q(t = 0) = 0$.

S4. Electrolyte resistance model adapted from [4]

The change in electrolyte resistance is expressed in terms of axial strain, where R_0 is the electrolyte resistance at rest.

$$\frac{R}{R_0} = (1 + \varepsilon)^2 \quad \text{(S10)}$$

The electrolyte resistance at rest R_0 can be evaluated by Pouillet's law $R_0 = \frac{\rho L}{A_{cs}}$, where $\rho = 14.3\ \Omega\text{cm}$ is the electrical resistivity of the hydrogel [29,30], $L = 1.3$ cm is the length of hydrogel material separating the two electrodes in the supercapacitor, and $\mathrm{A_{cs}} = \pi(\frac{d_{hyd}}{2})^2 = \pi(\frac{17.5\ \text{mm}}{2})^2 = 2.42\ \text{cm}^2$ is the cross-sectional area of the hydrogel.

S5. Method for calculating total capacitance from cyclic voltammetry data

The conventional method of calculating capacitance from cyclic voltammetry data is used to calculate total capacitance of the soft supercapacitor at rest.

$$C_T = \frac{2\int_{t_1}^{t_2} V(t) \times I(t)\ dt}{(V_1 - V_2)^2} \quad \text{(S11)}$$

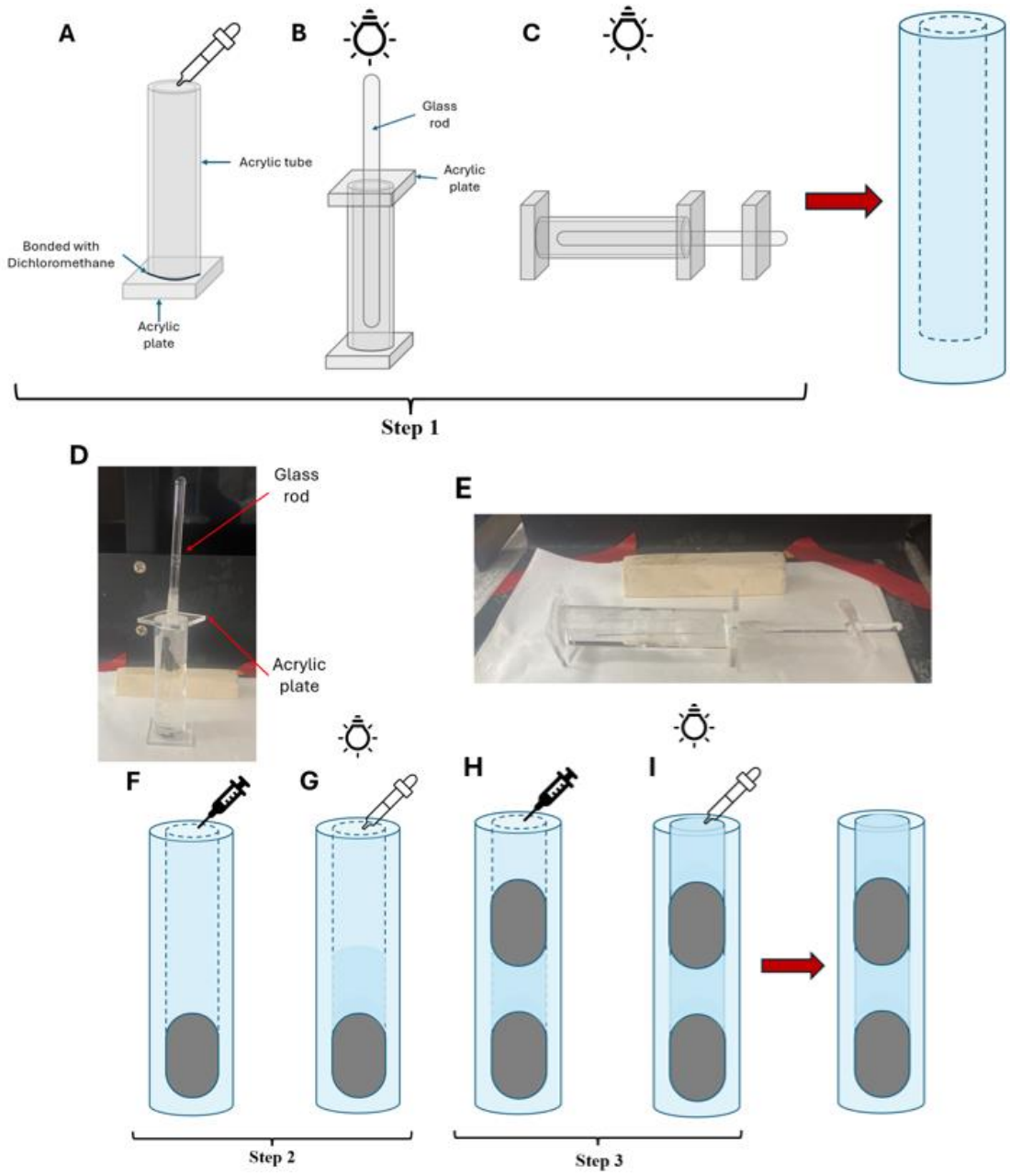

Figure S2. Soft supercapacitor fabrication. Step 1 – (A) Pre-gel solution of polyacrylamide hydrogel is filled in the acrylic mold. An acrylic plate with glass rod is placed inside the acrylic tube (B) to create the cavity for the liquid metal electrodes and curing under the UV lamp in this upright position for 4 minutes. The mold is then flipped on its side (C) to cure for another 3 minutes to make the hydrogel casing. Image of the mold in the upright position (D) and on its side (E). Step 2 – Once the hydrogel casing is removed from the mold, liquid metal is first

partially filled in the cavity (F) and pre-gel solution is added on top of the liquid metal (G). The device is cured in the upright position under the lamp for 90 seconds to create the reference electrode. Step 3 – To make the working electrode, liquid metal is added on top of the cured pre-gel solution in the cavity (H) and additional pre-gel solution is used to fill the rest of the cavity (I). The device is finally cured under the lamp in the upright position for 90 seconds to create the soft supercapacitor.